THE DEVELOPMENT OF HIGH STRENGTH HOT ROLLED STEEL

THE DEVELOPMENT OF HIGH STRENGTH HOT ROLLED STEEL FOR AUTOMOTIVE APPLICATIONS

By ESTHER HUTTEN, B.Eng.

A Thesis Submitted to the School of Graduate Studies in Partial Fulfilment of the Requirements for the Degree Master of Applied Science

McMaster University MASTER OF APPLIED SCIENCE (2019) Hamilton, Ontario (Engineering)

TITLE: The Development of High Strength Hot Rolled Steel for Automotive Applications

AUTHOR: Esther Hutten, B.Eng. (McMaster University)

SUPERVISOR: Dr. Hatem Zurob

NUMBER OF PAGES: xviii, 158

ABSTRACT

The development of high strength hot rolled steels is an important area for improving vehicle fuel efficiency. In collaboration with ArcelorMittal, this project focussed on developing a hot rolled steel with 980 MPa ultimate tensile strength, 800 MPa yield strength and 50% hole expansion ratio. To achieve the target mechanical properties, four different chemistries were trialled which varied the carbon, niobium and vanadium contents. Six combinations of finishing, coiling and intermediate temperatures were trialled for each chemistry.

The effects of thermomechanical processing parameters and alloying contents on the mechanical properties were determined through tensile and hole expansion testing. Microstructural analysis was completed to correlate the mechanical properties to the microstructural characteristics. Microscopy techniques performed included optical microscopy, scanning electron microscopy, transmission electron microscopy and atom probe tomography. The phase transformations which occur during thermomechanical processing were investigated using dilatometry testing.

Microstructural characterization was used to determine the breakdown of strengthening contributions from intrinsic, solid solution, grain boundary, precipitation and dislocation strengthening. Trials varying the processing parameters and steel chemistry led to an understanding of how thermomechanical processing and alloying influence the microstructural features and corresponding mechanical properties in hot rolled microalloyed steels.

PREFACE

The development of advanced high strength steel for automotive purposes is important for improving vehicle fuel efficiency. High strength steel applied to the design of a component can reduce the amount of material required for the component, thereby reducing vehicle weight. The objective of this project is to produce a hot rolled steel with an ultimate tensile strength of 980 MPa, yield strength of 800 MPa and 50% hole expansion ratio. The combination of strength and stretch flangeability is necessary for automotive structural components which require high strength with the ability to be formed into complex parts without cracking. Structural components use thick gauge material which is produced after hot rolling. This project is a new product development effort conducted in collaboration with ArcelorMittal Global R&D and is motivated by market need and by competition with other producers who have developed similar grades.

This thesis is organized based on how the experimental steel was developed. The thesis begins with a literature review in chapter 1, describing the strengthening mechanisms in hot rolled microalloyed steel. Chapter 2 outlines how the thermomechanical processing parameters and experimental chemistries were selected to produce ferritic and bainitic structures. Based on this work, steel was cast and hot rolled at the ArcelorMittal Global R&D Department in Maizières, France. Mechanical testing and microstructural analysis were completed on this material as outlined in chapter 3 and the results are presented in chapter 4. The connection between the thermomechanical

processing parameters, microstructural characteristics and mechanical properties are discussed in chapter 5. The thesis concludes with a summary of the results and recommendations to achieve the target mechanical properties.

This project was conducted under the supervision of Dr. Hatem Zurob and in collaboration with researchers from ArcelorMittal Global R&D, Dr. Sujay Sarkar, Dr. Erika Bellhouse and Dr. Yaping Lu. Regular discussions were had with these researchers who offered much guidance concerning alloy and process design as well as analysis of strengthening mechanisms in the experimental steels.

The experimental contributions of several others also contributed to the completion of this project. The TMP model and CCT diagram model were developed at McMaster University by researchers within the Steel Research Centre including Shenglong Liang. The TEM analyses presented in the following report were conducted by Dr. Xiang Wang. Dilatometry testing was performed by Marta Aniolek from CANMET and APT experiments were carried out by Dr. Brian Langelier.

ACKNOWLEDGEMENTS

First, I would like to thank my supervisor, Dr. Hatem Zurob for taking me on as a master's student, guiding me through this project and always taking time to answer my questions. Thank you for sending me to conferences, for the opportunity to work in France, and encouraging me to spend a semester in Italy. I am grateful for the opportunity to work as a master's student under your supervision and appreciate all your support.

There are many people whose help was invaluable to the completion of this project. I would like to thank all of the MSE staff especially Doug Culley and Dr. Xiaogang Li for their help in the labs. Thanks to Dr. Xiang Wang for performing TEM analyses especially near the end of my project. I am grateful to Dr. Brian Langelier for APT analysis and always being available to explain complex analysis methods in an understandable way and to Chris Butcher, Jhoynner Martinez and Andy Duft for their support in the CCEM. I would also like to acknowledge the work of Marta Aniolek from CANMET on dilatometry testing. Special thanks to many friends and colleagues. Long hours spent writing were more enjoyable with friends.

I would like to acknowledge Dr. Erika Bellhouse, Dr. Sujay Sarkar and Dr. Yaping Lu from the ArcelorMittal Global R&D Department for their guidance. I am grateful for Sujay's support during my stay in France and for the opportunity to travel to the research department in Maizières.

This project was made possible through the financial support of the Natural Science and Engineering Research Council (NSERC), ArcelorMittal Global R&D and McMaster University.

Finally, I would like to thank my friends and family and especially Mom and Dad for their support, interest and encouragement throughout this project.

TABLE OF CONTENTS

LIST OF FIGURES

LIST OF TABLES

SYMBOLS AND ABBREVIATIONS

APT	Atom probe tomography
B-N OR	Baker-Nutting orientation relationship
CT	Coiling temperature
CR	Cooling rate
FT	Finishing temperature
HER	Hole expansion ratio
IT	Intermediate temperature
M/A	Martensite/austenite
SEM	Scanning electron microscope
TE	Total elongation
TEM	Transmission electron microscope
TMP	Thermomechanical processing
T_{nr}	No-recrystallization temperature
UE	Uniform elongation
UTS	Ultimate tensile strength
YS	Yield strength

C_{eq}	Carbon equivalence
K_y	Constant for determination of lath width strengthening
$\dot{T}$	Cooling rate
T_S	Transformation start temperature
V_i	Volume fraction of component i
c_i	Weight fraction of element i

d_{α_0}	Ferrite grain size under strain free conditions
d_{α}	Ferrite grain size
d_{γ}	Austenite grain size
k_i	Solid solution strengthening coefficient of element i
k_s	Solubility product
k_y	Grain boundary strengthening coefficient
l_0	Bainite lath width
r_{ppt}	Radius of precipitate
β_{0-3}	Curve fitting constant for ferrite grain size determination
ε_r	Retained strain
σ_0	Intrinsic strength
σ_{disl}	Dislocation strengthening
σ_{gb}	Grain boundary strengthening
σ_i	Strength of component i
σ_{lath}	Lath width strengthening
σ_{ppt}	Precipitation strengthening
σ_{ss}	Solid solution strengthening
τ_f	Frictional stress of lattice
A	Constant used in determination of solubility constant
$A-C$	Constants for ferrite grain size determination
B	Constant used in determination of solubility constant
E	Elastic modulus
F	Ferrite fraction
G	Shear modulus
L	Particle spacing

M	Taylor factor
T	Temperature
X	True particle diameter
a	Unit cell edge length
b	Burgers vector
d	Grain diameter
f	Volume fraction of precipitates
k	Constant for determination of lath width strengthening
l'	Bainite lath width measured using EBSD linear intercept method
r	Radius of bowing of dislocation
v	Poisson's ratio
w	Width of dislocation
x	Average particle diameter in the plane of intersection
α	Constant for dislocation strengthening determination
β	Variable describing austenite microstructure
γ	Surface energy
ρ	Dislocation density
τ	Shear strength

Chapter 1

Literature Review

Plastic deformation takes place when the resolved shear stress exceeds the critical value needed to initiate dislocation motion. A material is strengthened by the interaction of strain fields within the matrix, increasing the critical resolved shear stress. Dislocations introduce compressive, tensile and shear strains which interact with strain fields around solute atoms, grain boundaries, precipitates and other dislocations. When the strain fields of these factors interact, dislocation motion is impeded, and the strength of the material increases [1], [2].

Microalloyed steels contain small additions of microalloying elements like titanium, niobium and vanadium to contribute to the strength of the steel by grain refinement and precipitation strengthening. Careful selection of the thermomechanical processing (TMP) parameters to produce these steels ensures effective use of the microalloying additions for strengthening.

The following literature review discusses the five mechanisms that work together to strengthen steel: intrinsic strength (σ_0), solid solution strengthening (σ_{ss}), grain boundary strengthening (σ_{gb}), precipitation strengthening (σ_{ppt}) and dislocation strengthening (σ_{disl}) [3]. These mechanisms will be discussed in the context of hot rolled microalloyed steels. Each section covers how the magnitude of the strengthening contribution is calculated and the factors that influence the strengthening contribution during TMP.

1.1 Intrinsic Strength

The iron lattice has an inherent resistance to dislocation motion called the Peierls stress. The Peierls stress is related to the friction within the iron lattice and depends on the distance between slip planes and the slip distance. The magnitude of the Peierls stress decreases with increasing dislocation width, which is the extent of lattice distortion around a dislocation. This is represented by equation (1.1) where τ_f is the frictional stress of the lattice, G is the shear modulus, w is the dislocation width and b is the burgers vector.

$$\tau_f = Gexp\left(-\frac{2\pi w}{b}\right) \quad (1.1)$$

As temperature decreases, the dislocation width decreases resulting in a high frictional stress at low temperatures [4].

At room temperature, the Peierls stress of the BCC iron lattice is small. Gladman presents values determined by several researchers ranging from 15 to 70 MPa. At room

temperature, the intrinsic strength has a small contribution to the overall strength of the material [3].

1.2 Solid Solution Strengthening

The solid solution strengthening of microalloying elements can be quantified by equation (1.2) where c_i is the weight fraction of element i and k_i is its strengthening coefficient.

$$\sigma_{ss} = k_i c_i \quad (1.2)$$

The linear relationship between the strengthening contribution of solute alloying elements and their weight fraction is shown in Figure 1.1. In general, the value of the strengthening coefficient is related to the lattice distortion caused by the size of the solute atoms. Distortion in the lattice creates local strain fields which interact with the strain fields of moving dislocations, strengthening the material. The individual strengthening coefficients and lattice dilation effects are given in Table 1.1. Carbon and nitrogen are interstitial atoms with the largest lattice dilation and strengthening coefficient. Silicon and manganese are commonly used alloying elements in steels for their contribution to solid solution strengthening. Molybdenum contributes minimally to solid solution strengthening. Although chromium has the same lattice dilation affect as Mn, it has a negative effect on solid solution strengthening for other reasons [3].

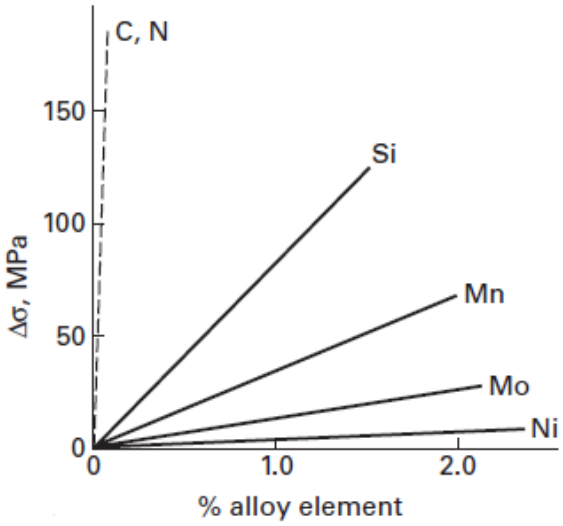

Figure 1.1. Linear dependence of yield strength on weight fraction of alloying elements in BCC iron [1]

Table 1.1 Solid solution strengthening coefficients for commonly used microalloying elements [3]

Element	**Solid Solution Strengthening Coefficient: Δc_i per 1 wt% (MPa)**	**% Lattice Dilation: Δa/a per 1 wt%**
C and N	4620-5544	4.000
Si	83	-0.042
Mn	31-32	0.020
Mo	11	0.041
Cr	-31	0.020

1.3 Grain Boundary Strengthening

Grain boundaries act as barriers to dislocation motion. Due to the discontinuity between the slip planes from one grain to the next, the dislocations pile up when they approach a grain boundary. The well-established Hall-Petch equation (1.3) quantifies the

stress required for slip to cross the grain boundary. In this equation, k_y is the grain boundary strengthening coefficient and d is the grain diameter.

$$\sigma_{gb} = k_y d^{-1/2} \quad (1.3)$$

A stress field is associated with the dislocations that pile up next to a grain boundary under an applied stress. This creates stress in the neighbouring grain until a critical stress is reached at which point new dislocations are created in the neighbouring grain in response to the stress field. The stress accumulating from the dislocations is proportional to the number of dislocations which increases with increasing grain size [1].

The grain size strengthening coefficient is dependent on material composition and can be determined experimentally for a specific material [1]. Kamikawa et al [5] use a k_y value of 0.21 MPa $m^{1/2}$ for an ultralow carbon IF steel considering a grain boundary misorientation angle of 2°. Mao et al [6] and Funakawa et al [7] use a value of 0.55 MPa $m^{1/2}$ for ferritic steels.

1.3.1 Grain Size During TMP

Ferrite nucleates preferentially on austenite grain boundaries and on deformed substructures produced during hot rolling within the austenite grains [8]. Consequently, the final grain size after processing is affected by austenite grain growth during reheating, grain growth between deformation passes, recrystallization during hot rolling and the austenite to ferrite transformation during cooling [9]. The following section will discuss the microstructural changes that occur during reheating, rolling and cooling and how the

changes are affected by the TMP parameters and steel chemistry in hot rolled microalloyed steel.

1.3.1.1 Reheating (Austenite Grain Growth)

The evolution of austenite grain size during reheating is affected by solute drag and precipitation. Solute drag reduces the mobility of the austenite grain boundaries and precipitates limit austenite grain growth by producing a pinning force on the moving boundary. Saito et al. found that the effect of the initial austenite grain size following reheating disappeared after three rolling passes in a Ti-V microalloyed steel [8]. Hodgson and Gibbs also state that the change in grain size during reheating is not important for most products but instead, the amount of microalloying elements remaining in solution after reheating is important as they affect the recrystallization, grain growth and precipitation during hot rolling [10].

1.3.1.2 Hot rolling (Recrystallization and Grain Growth)

Austenite recrystallization and grain growth determine the final austenite grain size after hot rolling. An important parameter during hot rolling is the no-recrystallization temperature (T_{nr}) which is the temperature below which recrystallization no longer occurs. Deformation below this temperature leads to a pancaked microstructure.

Above T_{nr} static recrystallization occurs between rolling passes refining the austenite grain size [11]. The recrystallized grain size is affected by initial austenite grain size, deformation temperature and applied strain [8], [9]. The austenite grain boundaries are nucleation sites for recrystallized grains, so the number of nucleation sites increases

with smaller initial austenite grain size and the recrystallized grain size decreases. Militzer et al. states that the minimum recrystallized grain size is limited to the initial austenite grain size [9].

As temperature decreases, recovery is reduced, and the dislocation density increases. When less recovery occurs, there is increased opportunity for recrystallization and nucleation of recrystallized grains. Lower temperature also reduces the grain boundary mobility, retarding austenite grain growth as seen by Hodgson and Gibbs [9], [10].

Larger strain increases the dislocation density and introduces subgrains which are nucleation sites for new recrystallized grains, thereby also reducing the recrystallized austenite grain size. Dutta and Sellars showed that the T_{nr} should decrease with increasing strain levels. However, during strip rolling which has high strain levels, recrystallization may stop before T_{nr} due to the short interpass times which do not allow enough time for recrystallization to occur [12].

Below T_{nr} strain induced precipitation occurs before recrystallization is complete, effectively stopping recrystallization by the pinning force of the precipitates on the grain boundaries [10]. Several researchers have investigated the effects of microalloying additions on the evolution of the austenite grain size during hot rolling. Militzer et al. investigated the effects of Nb and V on recrystallization and grain growth in microalloyed steel. Militzer et al. found that Nb slows recrystallization and increases T_{nr}. Nb has a solute drag effect which retards recrystallization, thus aiding strain

accumulation. In contrast, strain accumulation was not seen in V steel without Nb [9]. In 2013, Rehman and Zurob also discuss the effect of solute Nb on recrystallization kinetics, showing that solute Nb delays nucleation of recrystallized grains by pinning dislocations and limiting sub-grain growth which act as nucleation sites for recrystallized grains [13].

In 1987, Dutta and Sellars discussed the effects of Nb on recrystallization. They observed that Nb in solid solution slows recrystallization but strain induced precipitation of Nb(C,N) has a more significant effect and stops recrystallization at T_{nr} [12]. Zhang et al. investigated the effect of (Ti,Mo)C on recrystallization in 2016. Below T_{nr}, strain induced precipitation of (Ti,Mo)C occurs, restricting static recrystallization and allowing strain accumulation to occur. This increases the austenite grain boundary area per unit volume and provides numerous ferrite nucleation sites, refining the ferrite grain size upon transformation [11].

In considering grain growth, the solute drag effect of Nb also limits the grain growth of austenite even at temperatures well above T_{nr}. Rehman and Zurob showed that Nb in solid solution slows the growth of recrystallized austenite grains by lowering grain boundary mobility [13]. Vanadium has a weaker solute drag effect and is not very effective at limiting grain growth at hot-rolling temperatures. In addition, V does not form precipitates during hot rolling and as such does not pin the austenite grain boundaries. Titanium can have a small effect on grain growth if the titanium nitrides which form at high temperatures are small enough to pin the grain boundaries [9].

1.3.1.3 Cooling (Austenite to Ferrite Transformation)

The austenite to ferrite transformation occurs during cooling after hot rolling. It is important to consider the factors affecting the transformation to determine what affects the final ferrite grain size and its contribution to the overall strength. In 1979 Sellars and Whiteman wrote about the effect of austenite grain size and retained strain on the ferrite grain size since austenite grain boundaries and dislocations are preferential ferrite nucleation sites. When comparing C-Mn steels to C-Mn-Nb steels, a smaller ferrite grain size was produced in the Nb containing steels. This effect is seen repeatedly in other works and can be attributed to the solute drag and particle pinning effects of Nb [14].

Sellars and Beynon quantified the ferrite grain size in C-Mn, Nb and Ti-V steels as a function of cooling rate ($\dot{T}$), austenite grain size (d_γ) and composition where A, B and C are composition dependent constants.

$$d_\alpha = A + B\dot{T}^{-1/2} + C\left(1 - \exp\left(0.015 d_\gamma\right)\right) \quad (1.4)$$

The effect of retained strain (ε_r) when the austenite is not fully recrystallized can also be incorporated as shown in equation (1.5), where d_{α_0} is the grain size calculated from equation (1.4) under strain free conditions.

$$d_\alpha = d_{\alpha_0}\left(1 - 0.45{\varepsilon_r}^{1/2}\right) \quad (1.5)$$

As retained strain increases in the sample, alloying and cooling rate were found to have less of an impact on ferrite grain size compared to the retained strain [15].

An extension of Sellars and Beynon's relationship was presented by Hodgson and Gibbs in 1992 which incorporates the material composition through the carbon equivalency (C_{eq}) according to equation (1.6) where β_0, β_1, β_2 and β_3 are curve fitting constants [10].

$$d_{\alpha_0} = \left(\beta_0 + \beta_1 C_{eq}\right) + \left(\beta_2 + \beta_3 C_{eq}\right)\dot{T}^{-1/2} + 22\left(1 - \exp\left(0.015 d_\gamma\right)\right) \quad (1.6)$$

Other notable studies on this topic include the work of Umemoto et al. who focussed on the relationship between cooling rate and ferrite grain size. The temperature range in which the austenite to ferrite transformation occurs decreases when the cooling rate is increased. The lower transformation temperature leads to an increased nucleation rate and decreased growth rate. Consequently, the ferrite grain size is refined when the cooling rate is increased. Equation (1.7) relates ferrite grain size, d_α, to the austenite grain size, d_γ, and cooling rate, $\dot{T}$. The constants A, B and C are material dependent and obtained through curve-fitting [16].

$$d_\alpha = A\dot{T}^B d_\gamma^C \quad (1.7)$$

Suehiro et al. developed an expression for ferrite grain size based on the transformation start temperature, the final ferrite fraction and the initial austenite grain size. The transformation start temperature decreases with increased cooling rate and increased austenite grain size [17]. Militzer et al. expanded on Suehiro's relationship, incorporating the effect of retained strain. Militzer et al.'s formula for ferrite grain size is dependent on the final ferrite fraction (F), the initial austenite microstructure (β) which is

a function of the austenite grain size, the elastic modulus (*E*) and the transformation start temperature (T_S):

$$d_\alpha = \left(Fexp(\beta - E/T_S)\right)^{1/3} \quad (1.8)$$

In Nb containing steels, high levels of retained strain were reached and had a more important effect on ferrite grain size than austenite grain size. In this case, the variable β in equation (1.8) is defined in terms of retained strain (ε_r) instead of austenite grain size [9]:

$$\beta = 19.5 + 1.7\exp(-6\varepsilon_r) \quad (1.9)$$

A collection of formulas for calculating the ferrite grain size in hot rolled steels based on microstructure, TMP parameters and composition have been developed over the years. It is evident from the above formulas that prior austenite grain size, cooling rate and composition are important variables in determining the ferrite grain size. High enough levels of retained strain may overshadow the effects of austenite grain size, cooling rate and composition on the final ferrite grain size.

1.4 Precipitation Strengthening

The strengthening from precipitation is a function of precipitate size, strength, spacing and volume fraction. There are two modes by which dislocations can move around precipitates. First, dislocations can shear small soft particles. When a stress is applied and dislocation motion shears a particle, the surface area between the particle and matrix increases. Consequently, the total interfacial energy will increase. To shear a

particle, the work done must be greater than or equal to the energy of the new interface formed between particle and matrix. The shear strength (τ) is given in equation (1.10) where r_{ppt} is the particle radius, γ is the surface energy, b is the burgers vector and L is the particle spacing [1].

$$\tau = \frac{\pi r_{ppt} \gamma}{2bL} \quad (1.10)$$

The second mechanism of dislocation interaction with particles is dislocation bowing. In this case, the particles are too strong to be sheared. When the dislocation approaches the precipitates, it bows between the precipitates until the two ends of the dislocation meet and form loops around the precipitate. The applied stress for dislocation bowing to occur is determined using equation (1.11) where G is the shear modulus of the material and r is the radius of bowing of the dislocation [1].

$$\tau = \frac{Gb}{2r} = \frac{Gb}{L} \quad (1.11)$$

Equation (1.11) is known as the Orowan equation for particle strengthening. Assuming that particles are evenly distributed in a square grid through the matrix, the increased yield strength (YS) due to precipitation strength using the Orowan model can be calculated with equation (1.12) and (1.13) where f is the volume fraction of precipitates and X is the true particle diameter which depends on x, the average diameter of particles in the plane of intersection [1].

$$\sigma_{ppt} = \frac{6Gb\left(\frac{3f}{2\pi}\right)^{1/2}}{X} \quad (1.12)$$

$$X = (3/2)^{1/2}x \quad (1.13)$$

The Orowan model overestimates the precipitation strengthening because it assumes the dislocation is parallel to the edge of the square grid of particles. If the dislocation is parallel to the diagonal of the square, the effective particle spacing increases reducing the force required to bypass the particles. In addition, precipitates are not always evenly distributed in a grid-like array. A random distribution of particles will affect the precipitate spacing and corresponding strengthening as compared to a regular array of particles [3].

Ashby modified the Orowan model by considering the effective particle spacing and produced equation (1.14) for strengthening from a random array of precipitates.

$$\tau = 0.84\left(\frac{1.2Gb}{2\pi L}\right)\ln\left(\frac{x}{2b}\right) \quad (1.14)$$

This can be translated into the increase in YS from precipitation [3].

$$\sigma_{ppt} = \left(\frac{10.8f^{1/2}}{X}\right) * \left(\ln\left(\frac{X}{6.125 * 10^{-4}}\right)\right) \quad (1.15)$$

The model proposed by Ashby shows the dependence of precipitate strengthening on the volume fraction of particles and particle diameter. Figure 1.2 shows the increase in precipitate strengthening with increasing volume fraction of precipitates and decreasing

particle diameter as determined using the Ashby-Orowan model. For comparison, the precipitation strengthening as determined using the Orowan model for a 5 nm particle size is also shown.

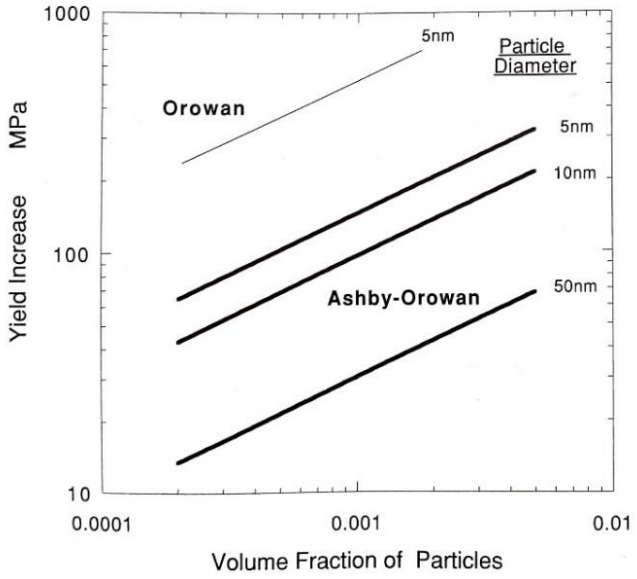

Figure 1.2. Comparison of Orowan and Ashby-Orowan models for YS based on volume fraction and size of particles

1.4.1 Precipitation During TMP

Precipitation can occur at several stages during TMP: i) in austenite before, during or after deformation, ii) during the austenite to ferrite transformation and iii) in ferrite following the transformation [18]. There are two main effects of the precipitates that form during TMP. Precipitates that form in stage i) are often large and do not contribute significantly to the strength of microalloyed steel, however they have an important effect on the austenite and resulting ferrite grain size. Precipitates that form in

stage ii) and iii) can be much smaller and contribute to dispersion strengthening in microalloyed steel [19].

1.4.1.1 Precipitation in Austenite

Precipitation in austenite before deformation is related to the solubility of the carbides and nitrides at high temperature. Solubility products depend on temperature and are written in the form shown in equation (1.16) where A and B are constants depending on the type of nitride or carbide and the matrix composition.

$$logk_s = A - \frac{B}{T} \quad (1.16)$$

Gladman provides an overview of the solubilities of the carbides and nitrides in austenite of the common microalloying elements, Ti, Nb and V. A comparison of the solubility products of Ti, Nb and V carbides and nitrides in austenite and ferrite are shown in Figure 1.3.

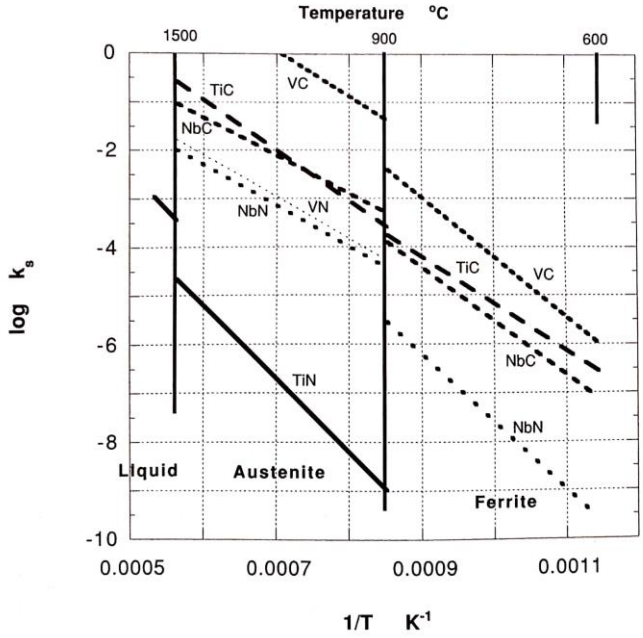

Figure 1.3. Comparison of the solubility products of Ti, Nb and V carbides and nitrides in austenite and ferrite

Three summarizing points can be taken from Gladman which are of importance to precipitation in austenite. First, the nitrides of Ti, Nb and V are always more stable than their carbides. Secondly, out of all the carbides and nitrides, TiN is the most stable in both austenite and ferrite. Finally, VC is the most soluble (or least stable) of the microalloying precipitates in austenite [3].

In relation to precipitation, the purpose of reheating is to dissolve the carbides and nitrides into the austenite. For precipitates to significantly contribute to the final strength of microalloyed steel, they need to be of the order of 3 to 5 nm. This is only possible if the precipitates form at lower temperatures. This will be described in the following sections. Ensuring that the microalloying elements are dissolved into the austenite during reheating is important to increase the driving force for precipitation during the subsequent

TMP steps. Some of the more stable nitrides such as TiN may remain undissolved in the austenite during reheating [9] and could act as nucleation sites for further precipitation during subsequent TMP steps [20].

After deformation the rate of precipitation increases because of the creation of nucleation sites in austenite. The dislocations and subgrains formed during deformation are nucleation sites for strain induced precipitation in deformed austenite [19]. The effects of strain induced precipitation on the austenite and subsequent ferrite grain size were addressed in Section 1.3.

Precipitation in austenite influences the processes of recovery and recrystallization and will consequently affect the product's final microstructure. Rehman and Zurob consider the interactions between precipitation, recovery and recrystallization in austenite in their modelling of recrystallization in austenite. First, carbides and nitrides in austenite retard recovery by pinning dislocations. Precipitates also slow recrystallization by Zener pinning, reducing the growth rate of recrystallized grains. The progress of recovery also affects precipitation by reducing the number of nucleation sites for precipitation. In addition, as recovery proceeds, the dislocation density decreases, reducing the driving force for recrystallization [13]. It is evident that precipitation in austenite affects the process of recovery and recrystallization and correspondingly, the final ferrite grain size. In addition, precipitation that occurs in austenite reduces the amount of solute available for precipitation later during TMP which could contribute to dispersion strengthening.

1.4.1.2 Precipitation During Austenite to Ferrite Transformation

Interphase precipitates form at the austenite-ferrite interface during the austenite to ferrite transformation. Precipitates approximately 3 to 5 nm in diameter are produced at this stage and make an important contribution to the strength of microalloyed steel. Interphase precipitates form as bands parallel to the austenite-ferrite boundary. They nucleate on the interface during the austenite to ferrite transformation and continue to grow in the ferrite phase after nucleation [19].

Two models can be used to explain the formation of interphase precipitates. The ledge model (Figure 1.4 a.) was developed by Honeycombe. He argued that the austenite-ferrite interface is composed of mobile incoherent interfaces and low mobility coherent interfaces. The precipitates form on the interfaces with low mobility which have a Kurdjomov-Sachs (K-S) orientation relationship between austenite and ferrite. Solute builds up ahead of the interface and the interface with K-S orientation relationship remains immobile for enough time to allow solute to diffuse and form precipitates before the interface proceeds. This model provides an explanation for the parallel evenly spaced planar sheets of carbides observed in microalloyed steels [19].

Interphase precipitates do not always form neatly arranged planes. Ricks and Howell describe two mechanisms by which irregular or curved sheets of precipitates can form on high energy, mobile interfaces contrary to Honeycombe's model. The quasi-ledge model (Figure 1.4 b.) was developed by Ricks and Howell to explain curved sheets of regularly spaced precipitates. Their model does not require a particular orientation relationship between austenite and ferrite. Instead, as the interface moves it repeatedly bows out and is pinned by copious precipitation which forms on the interface. Alternatively, an irregular dispersion of coarse precipitates can form by a bowing of the interface between precipitates. This explains the random arrangement of interphase precipitates that are also observed in microalloyed steels [21].

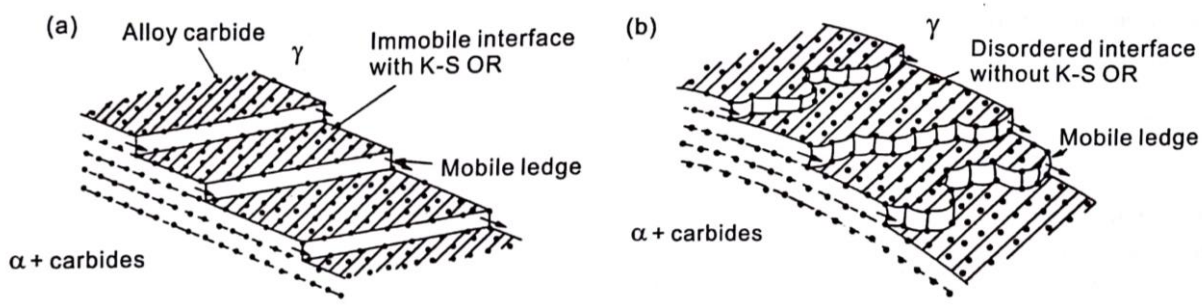

Figure 1.4. a. Ledge model and b. quasi-ledge model used to explain the dispersion of interphase precipitates observed in microalloyed steel

TMP parameters affecting dispersion strengthening in microalloyed steels have been studied by various researchers. Examples of studies determining the effects of transformation temperature, composition, size and arrangement of precipitates on the precipitation strengthening contribution are presented in the following paragraphs.

In 2011 Miyamoto et al. studied the effect of transformation temperature on VC interphase precipitation in medium-carbon steels. From 600°C to 700°C they found that ferrite was strengthened by interphase precipitation. Greater strength was achieved at lower transformation temperatures which produced smaller particles and higher number density of VC interphase precipitate [22]. Similar findings were made by Y. Zhang et al. in low-carbon steels [23]. At temperatures less than 580°C, strength decreased due to the formation of bainite which did not allow interphase precipitation to occur. Therefore, there is an optimal temperature above the temperature of bainite formation but low enough to maximize the driving force for interphase precipitation and its corresponding strengthening contribution [22].

Militzer et al. also investigated precipitation in V and Nb microalloyed steels. In V steels it was found that the maximum strength from precipitation would occur at approximately 675°C while in Nb steels that maximum strength occurs at 625°C. In general, it was found that the strengthening contribution increased with microalloying content [9].

In 2013 Chun et al. simulated coiling temperatures of 650 °C, 550 °C and 400 °C on Ti-Nb-V microalloyed steels. At 650 °C they achieved a 998 MPa ultimate tensile strength (UTS) steel with 65% hole expansion ratio (HER). The steel contained ferrite along with some regions of granular bainite and martensite. The interphase precipitation found in ferrite increased the strength of the ferritic regions and reduced the hardness deviation between the microstructural constituents, producing a favourable combination

of strength and stretch flangeability. At lower temperatures the volume fraction of microalloyed carbides progressively declined with the formation of bainite and martensite which was also found by Miyamoto et al. [22]. A bainitic and martensitic microstructure was formed at 500°C which produced a high strength of 1021 MPa UTS but due to the hardness deviation between bainite and martensite and with a reduced volume fraction of nanoprecipitates, the HER only reached 20% [24].

In 2014 Jang et al. wrote about the effects of adding Mo to Ti-Nb microalloyed steel. Mo was found to refine the dispersion of interphase precipitates by reducing the row spacing and size of the precipitates. Mo decreases the misfit strain between the carbide and ferrite during nucleation of the carbide, making it more kinetically favourable for nucleation to occur and reducing the row spacing and precipitate size. Growth of the precipitate then continues without Mo [25]. Kamikawa et al. studied Ti and Ti,Mo-added steels and found that the addition of Mo resulted in a finer dispersion of interphase precipitates, increased strength and similar ductility in comparison to the Mo-free steels [18].

In 2016 Zhang et al investigated both strain induced and interphase precipitation in Ti-Mo microalloyed steels, making valuable observations both about the effects of coiling temperature (CT) and Mo. Considering coiling temperatures from 500 °C to 650 °C, a CT of 600 °C produced the highest mass fraction of precipitates less than 10 nm in diameter. Two groups of precipitates were identified: those less than 10 nm and those from 10 to 20 nm in diameter. The latter were determined to have formed in

austenite as strain induced precipitates for three reasons: i) their relatively large size, ii) they did not hold a Baker-Nutting orientation relationship (B-N OR) with the ferrite matrix characteristic of interphase precipitation and iii) the larger precipitates contained a higher fraction of Ti than Mo compared to smaller precipitates showing that they formed at higher temperatures where the Ti solubility is low relative to Mo solubility. The precipitates less than 10 nm in diameter held a B-N OR with ferrite and had a smaller Ti to Mo ratio than larger precipitates [11].

Zhang et al. found that the strain induced precipitation had two important effects on the main strengthening contributions, grain size and precipitation. First, strain induced precipitates limit austenite grain growth thereby refining the ferrite grain size to 2.3 μm, but their formation in turn reduces the amount of solute available for interphase precipitation. Therefore, a balance between strain induced and interphase precipitation should be found which ensures that a fine ferrite grain size and high mass fraction of interphase precipitates are formed [11].

In 2013 Chen et al. found that the strengthening contribution from interphase precipitation is mainly dependent on sheet spacing, particle spacing and carbide size. Two microstructures with the same volume fraction of precipitates could have different strengths because of different carbide arrangements. They found that as time progresses during the austenite to ferrite transformation the sheet spacing decreases and the particle spacing increases. The sheet spacing depends on interface velocity. As the transformation progresses, the driving force for transformation falls, reducing the interface velocity and

consequently the sheet spacing. At the same time, less solute is available for precipitation so the particle spacing increases [26].

1.4.1.3 Precipitation in Ferrite

The final stage of precipitation can occur in ferrite after hot rolling by raising the temperature of the material. As discussed by Kestenbach, aging treatments can produce a fine dispersion of precipitates which form on dislocations in ferrite and contribute to strengthening [27]. This method will not be considered here because aging heat treatments are outside the scope of this project.

1.5 Dislocation Strengthening

The primary strengthening contributions in ferritic steels come from grain size and precipitation, whereas an important source of strength in bainitic steels is from dislocation strengthening. This section will discuss dislocation strengthening with a focus on bainitic microstructures. Saito et al. found that when the driving force for austenite decomposition is greater than 400 J/mol, bainite formation can occur instead of a ferritic or pearlitic transformation. Cooling rate and composition are important factors affecting the driving force for bainite transformation [8].

The lath size and dislocation density are the primary sources of strength in bainite [28], [29]. The strengthening contribution from dislocation density is given by the Taylor relationship shown in equation (1.17) where α is 0.38 for BCC iron, M is the Taylor factor and equals 2.75, G is the shear modulus of 81.6 GPa and b is the Burgers vector equal to 0.248 nm [5].

$$\sigma_{disl} = \alpha MGb\sqrt{\rho} \quad (1.17)$$

The lath size is analogous to the grain size in ferrite. The lath boundaries act as boundaries to dislocation motion where boundaries with higher misorientation are stronger barriers to dislocation motion. Bainite is composed of packets of laths. Zhu et al. found that lath boundaries, characterized by a low misorientation angle from 2-7°, are the primary boundaries affecting the YS [30]. In the Hall-Petch equation, Siwecki et al. use a Hall-Petch factor of 0.19 MPa $m^{1/2}$ to calculate the strengthening contribution from lath width for fine bainitic steels with high dislocation density [29].

Zhu et al. investigated the factors affecting bainite strength in ultra-low carbon steels to eliminate the effects of carbide precipitation. The strengthening contribution from lath size was found using equation (1.18) based on a relationship from Kuhlmann-Wilsdorf [31], substituting the dislocation cell size with lath width (l_0).

$$\sigma_{lath} = \frac{kMGb}{l_0} \quad (1.18)$$

Values for $K_y = kMGb$ ranged from 387 to 646 MPa μm corresponding to misorientation angles from 2° to 7°. Fazeli et al. use a K_y value of 115 MPa μm for a vanadium microalloyed bainitic steel. Zhu et al. developed a correction factor to determine the actual bainitic lath width (l_0) from the lath width measured from EBSD maps with the linear intercept method (l'). This was also used by Hell et al. [32]:

$$l_0 = 0.32l' \quad (1.19)$$

The bainitic microstructure is refined with a lower transformation temperature [29]. Mn, Cr and Mo are commonly added alloying elements to increase the hardenability of the material, lowering the transformation temperature. For maximum refinement of bainite, the transformation temperature should be minimized while remaining above the martensite start temperature. An increase in cooling rate will also decrease the transformation temperature, increasing the strength of the bainite with a finer bainitic structure and higher dislocation density [29]. Saito et al. found that the bainite fraction increased with the cooling rate but only when the C and Mn contents were high enough to increase the material's hardenability [8].

Prior deformation affects the kinetics of the bainite transformation. Hu et al. found that with increased deformation at high temperatures, the growth rate of bainite decreases. This is a result of accumulated dislocations in austenite which stabilize the austenite, slowing and delaying bainite growth. A slower growth rate results in a refined bainite structure with higher dislocation density, contributing to higher bainite strength [33].

The effects of vanadium on the bainite transformation kinetics has been studied by various researchers. Typical coiling temperatures result in softening of the bainitic microstructure through recovery. Siwecki et al. hypothesized that the addition of vanadium promotes the formation of vanadium carbonitrides during coiling which restrict dislocation motion, retarding recovery. The effects of vanadium are enhanced at lower coiling temperatures with the reduction of recovery kinetics. The fine precipitates that

formed during coiling had a small strengthening effect, but the contribution was minimal in comparison to their effect on dislocation strengthening through the retardation of recovery [29].

Nafisi et al. studied a V and V-free bainitic steel, comparing the precipitates that formed and the effect of the precipitates on the microstructure. The vanadium containing steel had a higher UTS and YS with smaller microalloyed precipitates and a higher total number density of precipitates. However, the precipitates did not account for the total strength increase seen with the addition of vanadium. Although no microstructural evidence was provided, Nafisi et al. proposed that the remaining strength was a result of the precipitates limiting the recovery of the bainitic microstructure [34].

Fazeli et al. determined that vanadium addition retards the bainite transformation, shifting the transformation to lower temperatures. Consequently, the lath width decreases and the dislocation density increases resulting in a stronger bainite as seen in equations (1.17) and (1.18). In addition, they found that the vanadium added material maintained its strength more effectively than the vanadium free material after isothermal holding at the coiling temperature (CT), pointing to the effect that vanadium has on recovery during coiling [28].

Fazeli et al. and Siwecki et al. both considered the summation of lath and dislocation strengthening mechanisms and determined that a quadratic addition of the strengths is more accurate than a linear addition when the two obstacles have comparable strengths according to equation (1.20) [28], [29].

$$\Delta\sigma = \sqrt{\sigma_{lath}^2 + \sigma_{disl}^2} \quad (1.20)$$

1.6 Examples

This project is being conducted in collaboration with ArcelorMittal Global Research and Development to produce a hot rolled steel for use in automotive applications with a target UTS of 980 MPa, 800 MPa target YS and 50% target HER. Examples of hot rolled microalloyed steels with comparable mechanical properties will be outlined here from patents and other literature.

1.6.1 Patents

An ArcelorMittal patent from 2012 describes a product with a UTS of 780 MPa to 950 MPa (slightly lower than the current target of 980 MPa) and with a HER greater than 50%. The TE of the material is greater than 10%. This was accomplished with a microstructure of granular bainite, ferrite and less than 1.5% cementite along with titanium and niobium carbonitrides. The steel was rolled with a finishing temperature (FT) between 880 °C and 930 °C and coiled between 400 °C and 500 °C. Optionally an intermediate cooling step was incorporated between 640 °C and 700 °C for 2 to 10 seconds [35].

Nippon and Sumitomo produced a patent for a ferritic microstructure in 2005 with a UTS greater than 980 MPa and with a high HER. This steel was processed with a 950 °C FT, held at an intermediate temperature (IT) between 650 °C and 800 °C for 0.5 to 15 seconds and coiled between 300 °C and 600 °C. The material contained both

titanium and niobium with optional additions of molybdenum and vanadium. The patent also states the importance of avoiding cementite and martensite in order to achieve a high HER. The combinations of high strength and HER are shown in Figure 1.5 [36].

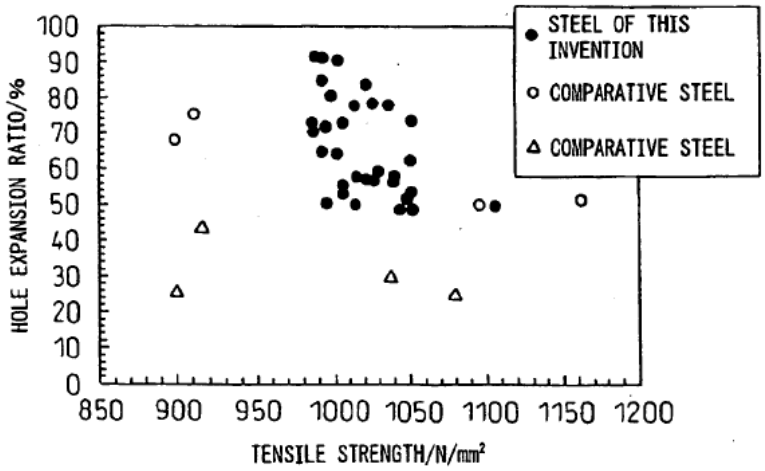

Figure 1.5. Combination of strength and HER from Nippon and Sumitomo patent

JFE produced a patent in 2004 for a steel containing multiple phases of 40 to 95% ferrite with titanium and molybdenum precipitates and secondary phases of bainite and martensite. The average precipitate diameter was less than 20 nm and average precipitate spacing was less than 60 nm. This material has a UTS greater than 780 MPa and HER over 60%. Processing incorporated intermediate cooling between 700 °C and 850 °C and a CT less than 550 °C. A key microstructural feature described here is the presence of precipitates in the ferrite, reducing the strength difference between the ferrite and martensite or bainite, thereby improving the HER by reducing hardness deviations present in the steel [37].

1.6.2 Other Approaches from Literature

Seto et al. present the NANOHITEN steel which achieves a 780 MPa UTS and 100% HER with a single phase microstructure. High strength is achieved with additions of Ti and Mo which form precipitates, on the order of one nanometer in diameter. The single phase uniform microstructure promotes a high HER and the presence of ultra-fine precipitates produces a high strength matrix, resulting in a combination of high strength and HER. The addition of Mo to the steel improves the thermal stability of the precipitates, preventing coarsening so that they remain on the scale of 1 nm. This steel has promising properties but the strength level achieved does not reach the target UTS of 980 MPa for the current project [38].

Zhang et al. present a high strength hot rolled ferritic steel with containing titanium, vanadium and molybdenum with a grain size of approximately 2.5 μm and a fine distribution of precipitates from 1 to 10 nm diameter. This steel had a UTS of 1000 MPa and YS of 955 MPa. The grain size and precipitates account for 361 MPa and 310 MPa of the YS respectively. It was determined that 600 °C was the optimal CT because it produced a large fraction of precipitates less than 10 nm in size. A CT of 550 °C reduced the diffusivity of microalloying elements and a CT of 650 °C resulted in coarsening of precipitates, both of which limited the precipitation strengthening contribution [39]. This work does not include hole expansion values which are of importance when developing steel for structural automotive applications.

Siwecki et al. produced a high strength bainitic microstructure with a base containing 1.4% Mn, 1.0% Cr and 0.25% Mo. An addition of 0.08% V increased the YS by approximately 100 MPa up to 790 MPa due to the precipitation of fine vanadium carbonitrides which prevent recovery and softening of the microstructure. The strength was attributed to a lath width of 1 μm and high dislocation density which contributed 190 MPa and 410 MPa to the total YS respectively. The strength of the matrix, including solid solution strengthening, accounted for the remainder of the strength. The effect of precipitates on the strength was seen in the increase of dislocation strengthening by preventing recovery, rather than in precipitation strengthening [29]. Although high strength was achieved, this paper also does not address the HER of the material.

Nafisi et al. discuss API X100 linepipe steels which contain 0.06% C, 2% Mn, 0.4% Mo and 0.03% Nb and are coiled at 450 °C resulting in a bainitic microstructure. The addition of 0.06% V increased the YS and UTS by 60 to 95 MPa, achieving a UTS up to approximately 900 MPa. The strength increase was attributed in part to the precipitation strengthening contribution due to the decrease in precipitate size and increase in number density of precipitates with the addition of vanadium. However, the precipitates did not account for the total increase in strength and it was hypothesized that vanadium increased dislocation strengthening by restricting dislocation recovery [34].

1.7 Summary

Based on the past work covered here, two microstructures will be presented in the trialled steel to achieve the strength and stretch flangeability requirements. A

precipitation hardened polygonal ferrite microstructure is considered where grain boundary and precipitation strengthening are the primary sources of strength. The second microstructure under consideration is a high strength bainitic structure where dislocation strengthening is an important strengthening mechanism. The optimal combination of processing parameters and chemistry will be determined by trialling six different sets of processing parameters and four different chemistries. The contribution to the total strength from the individual strengthening mechanisms, solid solution strengthening, grain boundary strengthening, precipitation strengthening and dislocation strengthening, are determined using microstructural analysis.

Chapter 2

Alloy and Process Design

TMP processing parameters and alloying additions were selected to produce two microstructures which could achieve the target mechanical properties: a ferritic steel strengthened by a fine grain size and interphase precipitation and a bainitic structure strengthened by a fine lath width and high dislocation density.

2.1 Alloy Design

A base chemistry was developed which includes Mn, Si, Cr, Al, Ti, Mo and N. The Ti is used to tie up residual nitrogen in the matrix through the formation of TiN which is expected to form at high temperatures in the austenite. Ti is added for a 1:1 atomic ratio of Ti and N. The TiN that forms also contributes to grain boundary pinning during reheating and welding. However, too much Ti will result in the formation of coarse carbonitrides which do not contribute to the strength of the steel. Mn is an austenite stabilizer, increasing the steel hardenability and promoting the formation of

bainite. It also has an important solid solution strengthening component but must be added in limited quantities because Mn segregation during casting leads to banding which has a negative affect on the HER properties. Si and Mo both contribute to solid solution strengthening and have a positive affect on the HER by suppressing the formation of pearlite and cementite [40], [41]. Mo also refines the distribution of interphase precipitates and increases hardenability of the material, decreasing the bainite start temperature and promoting a fine bainitic structure [42]. However, Mo in high quantities can have a negative affect on weldability [41]. Si can have a negative impact on surface quality and results in high rolling loads if the content is too high. Cr is added to the steel for its effect on hardenability. Al is added to steel as a deoxidizer but in limited quantities because it can have a negative affect on the HER [40], [41]. The selected base chemistry is displayed in Table 2.1.

The C, Nb and V additions are varied in four different chemistries to study the effect of each element as shown in Table 2.2. C impacts the hardenability and promotes the formation of carbides in the steel. Too little C could limit strengthening from precipitation while too much can promote the formation of phases that reduce the HER (e.g. martensite, cementite). The carbon content is increased from 0.08 wt% in the base chemistry to 0.11 wt% in chemistry B to determine how the microstructure and mechanical properties are affected. V and Nb are added for their influence on precipitation strengthening, recrystallization and grain refinement. Both are important carbide forming elements which were shown to have an important effect on interphase precipitation. The addition of V has also been shown to retard recovery in bainite during

coiling. The addition of Nb and V should be limited to ensure they are used effectively for precipitation strengthening and not lost as coarse precipitates. In addition, too much Nb may result in high rolling loads [40], [41]. The Nb and V levels were selected using simulations to take into account solidification and TMP which control the contribution of Nb and V to strengthening. This is discussed further in Section 2.2. The effect of increasing Nb content is investigated by increasing the Nb content from 0.03 wt% in the base alloy to 0.05 wt% in chemistry C. Chemistry D looks at the affect of a 0.2 wt% V addition to the alloying contents in chemistry C.

Table 2.1. Target base chemistry (wt%)

Mn	Si	Cr	Al	Ti	Mo	N
1.9	0.5	0.3	0.035	0.02	0.2	0.005

Table 2.2.Target C, Nb and V content of the four chemistries trialled (wt%). The bolded values are the variations from the base chemistry.

Chemistry	C	Nb	V
A (Base)	0.08	0.03	0
B (+C)	**0.11**	0.03	0
C (+Nb)	0.08	**0.05**	0
D (+Nb,V)	0.08	**0.05**	**0.2**

2.2 Process Design

Appropriate TMP parameters were selected with the aid of simulations and CCT diagrams. The CCT diagram in Figure 2.1 was produced using a model developed at McMaster University [43] and was used in the selection of coiling temperatures. A TMP model also developed at McMaster University was used to simulate hot rolling and aided

in the selection of finishing temperatures. Six different combinations of processing parameters were selected and are displayed in Table 2.3.

Table 2.3. Target TMP parameters

Number	Finishing Temperature	Intermediate Temperature	Coiling Temperature
1	890	-	610
2			490
3	950	-	610
4			490
5	890	630	490
6	950		

Based on the CCT diagram in Figure 2.1, the base chemistry has a bainite start temperature of 528 °C, a martensite start temperature of 467 °C and an Ac_3 temperature of 837 °C. With increased C content, the Ac_3 and martensite start temperatures shift down slightly and the bainite nose also shifts right to longer times. As a ferrite stabilizer, the addition of V shifts the Ac_3 temperature up to 857 °C.

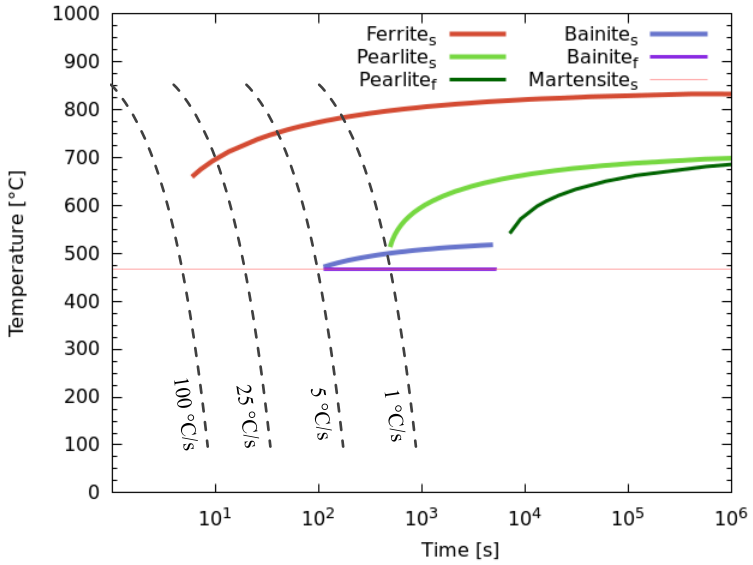

Figure 2.1. CCT diagram for base chemistry

The coiling temperatures were chosen using the CCT diagram. To produce a ferritic microstructure, a CT of 610 °C was selected which is within the ferrite region of the CCT diagram. This was raised to 630 °C for the vanadium containing material from chemistry D. A second CT of 490°C below the bainite start temperature and above the martensite temperature was selected to produce a bainitic structure. The coiling temperatures chosen are within the capability of industrial hot rolling mills. A two-step cooling process was suggested by ArcelorMittal based on success in previous work. This involves an intermediate air cooling step between finishing and coiling to nucleate ferrite and promote precipitation before coiling at a low temperature [35], [37], [36]. An IT of 630 °C with a holding time of 5 seconds was selected for this purpose. This temperature was raised slightly to 640 °C for the V containing sample.

Simulations using ThermoCalc and the TMP model were used to develop an understanding of the precipitation and microstructural evolution which occurs during finishing. The following three calculation steps were used to approximate the amount of precipitation that occurs with different TMP parameters and alloying contents:

1. Scheil solidification module (ThermoCalc) was used to examine precipitation during solidification
2. TMP model was used to quantify precipitation during hot rolling
3. ThermoCalc equilibrium calculations were used to assess precipitation at the CT

The Scheil solidification module is used to determine what precipitate phases form during solidification. The precipitates that form at this stage are large and do not contribute to the strength of the material. Step 2 uses the TMP model developed at McMaster University to determine how much precipitation occurs during hot rolling [43]. The amount of Nb and Ti available for precipitation during hot rolling was taken as the total Ti and Nb content, minus the amount that precipitated out during solidification in step 1. Precipitates that form during hot rolling are not expected to contribute significantly to the strength of the material, but they play an important role in controlling recrystallization and grain size development. The composition of the remaining matrix (excluding precipitates formed in steps 1 and 2) was used as an input in step 3. Step 3 determines how much precipitation occurs at the CT using Thermo-Calc equilibrium calculations. These steps provide a way of comparing the effect of different processing

temperatures and alloying contents on precipitation. Limiting precipitation in steps 1 and 2 is important to ensure that more solute is available for interphase precipitation in step 3.

In step 1, the Scheil solidification model shows that the fraction of the C lost to carbon rich phases increases with a higher initial C content. However, the total C content remaining in the matrix is still higher after solidification for the chemistry containing 0.11 wt% C than 0.08 wt% C. At the same time, C pulls microalloying additions like Nb out of solution which are potential contributors to precipitation strengthening in step 3. Increasing the Nb content has the same effect, causing a higher fraction of Nb to precipitate out during solidification and hot rolling. The C, Nb and V contents must be optimized to ensure that a large fraction does not precipitate out as large carbides which negatively affect the properties but that the additions of these elements are used efficiently to contribute to interphase precipitation strengthening.

Two important observations were made from simulations with the TMP model. First, the T_{nr} increases with increasing Nb content because Nb retards austenite recrystallization. Second, a higher initial Nb content in the matrix results in a higher fraction of Nb being lost as precipitates in the austenite. Keeping all other factors constant, increasing the Nb content from 0.03 wt% to 0.05 wt% results in little difference in the Nb content remaining in solution after hot rolling because of increased precipitation in austenite.

Two finishing temperatures were selected based on their effects on recrystallization and precipitation. A FT of 950 °C was used to ensure a fully

recrystallized austenitic structure was produced after finishing. A lower FT of 890 °C was selected to produce a refined grain structure due to pancaking below T_{nr}. A lower FT is also expected to result in a larger volume fraction of precipitates in the austenite as compared to a higher FT. Both finishing temperatures were selected to be well above the Ar_3 temperature to ensure hot rolling was completed within the austenite phase region. Knowledge of typical finishing temperatures used industrially also informed the selection of finishing temperatures.

Using ThermoCalc equilibrium calculations, the precipitate phase fraction present at the 610 °C CT was estimated. Precipitation increases with the amount of carbide forming elements present in solution after step 2. The effect of coiling at 490 °C on precipitation as determined with the ThermoCalc equilibrium calculations is insignificant because the calculation neglects kinetics. However, it is expected that precipitation at a CT of 490 °C would be minimal. The volume fraction of precipitates formed at 610 °C as determined in step 3 can be used to estimate the contribution to precipitation strengthening from interphase precipitates using equation (1.15).

It was useful to observe the effect of initial Nb content in the three calculation steps for the selection of Nb content. Many Nb levels were simulated and the choice of an appropriate Nb content was based on making a compromise between minimizing the amount of Nb lost during solidification, producing some precipitation during hot rolling for grain refinement while keeping enough Nb in solution to permit interphase

precipitation to occur. Chemistries A and C contain 0.03 wt% and 0.05 wt% Nb respectively to observe the effects of increased Nb experimentally.

Chapter 3

Experimental Methods

The following chapter covers the details of casting and hot rolling of experimental samples and mechanical testing. Sample preparation techniques used for SEM, TEM and APT are outlined and dilatometry testing procedures are described.

3.1 Casting

Ingots were cast in a vacuum induction furnace at ArcelorMittal Maizières Global R&D. The ingot size was 60 x 125 x 240 mm. Four different chemistries were cast and hot rolled to determine the effect of C, Nb and V on the microstructure and mechanical properties of the steel. The target base chemistry is the same for all four steels and is shown in Table 3.1. Table 3.2 shows the target C, Nb and V content for each chemistry. Chemistry A serves as a base comparison for chemistries B, C and D. Chemistries B and C investigate the effect of increased C and Nb content respectively. Chemistry D contains both increased Nb and V content to investigate their combined effect.

Table 3.1. Target base chemistry (wt%)

Mn	Si	Cr	Al	Ti	Mo	N
1.9±0.05	0.5±0.05	0.3±0.05	0.035±0.01	0.02±0.005	0.2±0.02	0.005±0.0005

Table 3.2. Target C, Nb and V content of the four chemistries trialled (wt%). C content is ±0.01%, Nb±0.005% and V±0.02%

Chemistry	C	Nb	V
A (Base)	0.08	0.03	0
B (+C)	**0.11**	0.03	0
C (+Nb)	0.08	**0.05**	0
D (+V)	0.08	**0.05**	**0.2**

Tables 3.3 and 3.4 show the as cast chemistries in comparison to the target chemistry. Two casts were made for each chemistry. Any deviations outside of the tolerances were not significant to be a concern.

Table 3.3. Actual base chemistry in comparison to the target values (wt%)

Chemistry		Mn	S	P	Si	Cr	Al	Ti	Mo	N
Target		1.90	0.002	0.010	0.500	0.300	0.030	0.020	0.200	0.005
Tolerance (±)		0.05	0.001	0.003	0.05	0.05	0.01	0.005	0.02	0.0005
A	1	1.89	0.002	0.012	0.485	0.301	0.027	0.016	0.205	0.003
	2	1.90	0.001	0.012	0.488	0.301	0.027	0.016	0.207	0.003
B	1	1.88	0.002	0.012	0.481	0.299	0.018	0.016	0.206	0.003
	2	1.90	0.002	0.012	0.482	0.300	0.016	0.015	0.209	0.003
C	1	1.90	0.002	0.014	0.489	0.301	0.031	0.014	0.208	0.004
	2	1.89	0.002	0.014	0.489	0.302	0.030	0.014	0.208	0.004
D	1	1.90	0.002	0.015	0.486	0.301	0.026	0.014	0.207	0.005
	2	1.89	0.002	0.014	0.486	0.301	0.024	0.014	0.205	0.006

Table 3.4. Actual C, Nb and V content in comparison to the target values (wt%)

Chemistry		Target			Actual		
		C (±0.01)	**Nb (±0.005)**	**V (±0.02)**	**C**	**Nb**	**V**
Base	A	0.08	0.03	0	0.079	0.028	-
	B				0.081	0.028	-
+C	C	**0.11**	0.03	0	0.107	0.027	-
	D				0.108	0.028	-
+Nb	A	0.08	**0.05**	0	0.087	0.047	-
	B				0.086	0.046	-
+V	C	0.08	**0.05**	**0.2**	0.087	0.047	0.197
	D				0.084	0.047	0.195

3.2 Hot Rolling

After casting, the billets were cut into 30 x 90 x 80 mm sections. The samples were reheated at 1250 °C and four roughing rolling passes were performed with a FT of 1150 °C. After roughing, finishing rolling was performed on the pilot hot rolling mill.

The pilot hot rolling mill consists of a reheating furnace, followed by one rolling stand and a cooling section. The cooling table has both air and water cooling. A bank of air cooling nozzles is located at either end and in the middle of the table. The table contains a total of fourteen banks of water nozzles, seven banks between each bank of air cooling nozzles. Pyrometers are situated at each stage in the rolling process to read the sample temperature: before and after the rolling stand and two pyrometers, a low and high temperature pyrometer, are located on either end of the cooling table. Three furnaces are available to simulate cooling in coil form after rolling.

After roughing rolling, samples were square and about 25 mm thick with a hole in one side where a thermocouple was inserted to take temperature readings during rolling. The samples were reheated in the reheating furnace to 1250 °C for 45 minutes. The sample was removed from the furnace and a thermocouple inserted. The thermocouple temperature readings were used to signal to the operators when each rolling pass was to be conducted. Two operators on either side of the rolling stand pushed the sample manually back and forth through the stand. Seven rolling passes were performed until a thickness of about 2.6 mm was reached. Upon failure of the thermocouple, the pyrometer readings were used. When the FT was reached after the final rolling pass, the sample was sent through the cooling section to achieve the CT. For trials involving intermediate cooling, the sample was held in air for four to five seconds at the IT after the first cooling pass and then sent back through the cooling table a second time to reach its final CT. After cooling, the sample was picked up and held under the exit pyrometers to get a final temperature reading. The sample was then quickly transferred to the cooling furnace. Prior to entering the furnace, the gauge was measured to verify the gap settings used during rolling.

The samples were cooled to room temperature at 30 °C/hour to simulate cooling in coil form. After cooling, they were removed from the furnaces and the head and tail end of each sample was cut off to produce a rectangular sample for mechanical testing and microstructure analysis. Each sample was used to produce three 100 mm by 100 mm hole expansion tests and three tensile tests in the rolling direction. Samples for SEM, EBSD and TEM analysis were also cut from these sheets. Hole expansion testing was

performed at ArcelorMittal Dofasco and tensile testing was performed at McMaster University using ASTM sub-sized samples.

3.2.1 Hot Rolling Parameters

In the hot rolling process, the finishing and coiling temperatures were selected to target the desired microstructure and mechanical properties. The FT is the temperature of the steel following the last hot rolling pass. The FT was varied between 890 °C and 950 °C as discussed in Chapter 2. After finishing, the steel is cooled to its CT. A CT of 610 °C was selected to produce a ferritic structure with microalloyed precipitates. A second CT of 490°C was selected to produce a bainitic structure. Finally, the effect of intermediate cooling on precipitation was tested by holding the steel at an IT of 630°C for approximately 5 seconds between finishing and coiling. The TMP processing parameters are provided in Table 3.5.

Table 3.5. Target TMP parameters

Number	Finishing Temperature	Intermediate Temperature	Coiling Temperature
1	890	-	610
2			490
3	950	-	610
4			490
5	890	630	490
6	950		

Table 3.6 contains the actual TMP temperatures from the hot rolling trials. The FT in Table 3.6 is an average between the thermo-couple and pyrometer readings. The

intermediate and coiling temperatures are the pyrometer readings because no thermo-couple readings are available for these values. The furnace number shows which samples were the first, second and third to be inserted into the coiling furnace. The coiling furnace can hold three samples at a time, so the furnace temperature was maintained at the CT until three samples were inserted. Once the furnace was filled, the samples were cooled at 30 °C/hour to room temperature. The furnace number is significant because samples 1 and 2 were held at the CT for up to 2 hours before cooling. The extended holding time at the CT could affect the final microstructure.

Table 3.6. Actual TMP parameters compared to target parameters including FT, cooling rate (CR), IT and CT. Red shaded cells show when temperatures fell outside of the target range. Temperatures with asterisk (*) apply to V containing samples.

Chemistry	Target/ Actual	FT (°C)	CR 1 (°C/s)	IT (°C)	Time (s)	CR 2 (°C/s)	CT (°C)	Furnace Number
	Target	890 ±15	>100	-	-	-	610/630* ±20	-
Base	**Actual**	896	96				624	1
+ C		898	94				609	1
+ Nb		889	96				629	1
+ V		902	83				*642	1
	Target	890 ±15	>100	-	-	-	490 ±20	-
Base	**Actual**	894	93				500	3
+ C		876	85				503	3
+ Nb		885	115				484	3
+ V		878	112				497	3
	Target	950 ±15	>100	-	-	-	610/630* ±20	-
Base	**Actual**	928	109				622	1
+ C		912	113				621	1
+ Nb		922	110				616	1
+ V		927	107				*623	1
	Target	950 ±15	>100	-	-	-	490 ±20	-
Base	**Actual**	938	107				477	3
+ C		927	106				471	3
+ Nb		916	116				499	2
+ V		920	115				500	2
	Target	890 ±15	>60	630 ±15	4	>40	490 ±20	-
Base	**Actual**	886	57	637	5	42	492	2
+ C		870	62	630	4	49	502	2
+ Nb		891	67	641	4	41	509	2
+ V		860	68	644	4	45	504	2
	Target	950 ±15	>60	630/640* ±15	4	>40	490 ±20	-
Base	**Actual**	915	74	630	5	47	484	3
+ C		933	74	626	5	43	483	3
+ Nb		928	77	627	4	44	506	3
+ V		918	78	*624	4	45	484	3

3.3 Mechanical Properties Testing

Mechanical properties were measured using hole expansion testing and tensile testing. The hot rolled sheets were sheared as shown in Figure 3.1. Three hole expansion coupons were taken from the sheets next to each other. The tensile specimens were machined from the centre of the remaining material in the rolling direction.

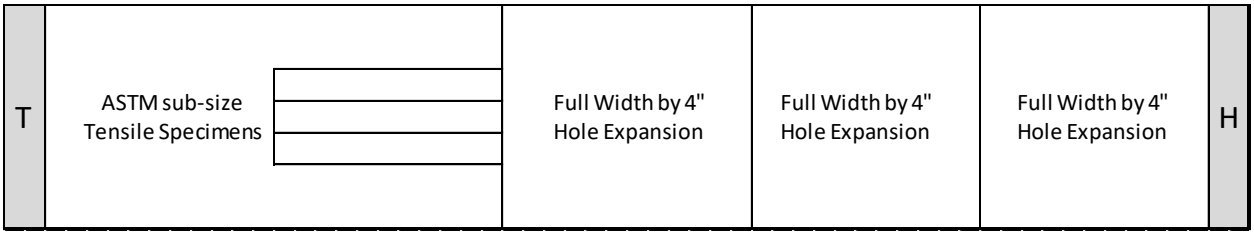

Figure 3.1. Sample shearing for hole expansion testing and tensile testing

3.3.1 Hole Expansion Testing

The hole expansion testing coupons were approximately 4 by 4 inches. The holes were punched in the centre of the coupons using an 85 ton Die Master punch to produce a 10 mm diameter hole. The holes were expanded using a 12 ton Hille Formability press. A high-resolution JAI Camera was used to observe the hole as it expanded during the test. This was coupled to a Matrox imaging computer which recorded the images of the test. The recorded images were reviewed to select the image where the first through thickness crack was visible. This is selected as the point of failure of the sample. The final diameter of the hole after forming was measured using Matrox software which uses the inside surface of the hole to measure the final diameter at failure. The HER is then determined with equation (3.1).

$$\% \, HER = \frac{(Final \; diameter - Original \; diameter)}{Original \; diameter} * 100 \quad (3.1)$$

The standard operating procedures for hole expansion were used as outlined in ArcelorMittal Dofasco's manual and follow the ISO/TS 16630 specifications. First the sample thickness was measured. The thickness of the material was used to select the hole punch which would produce a hole with 12% circumferential clearance according to equation (3.2), where t is the thickness of the material.

$$\% \, Clearance = \frac{(Die \; diameter - Punch \; diameter)}{2t} * 100 \quad (3.2)$$

The hole was punched in the centre of the square test coupon. The edges of the punched hole were inspected for good quality as shown in Figure 3.2.

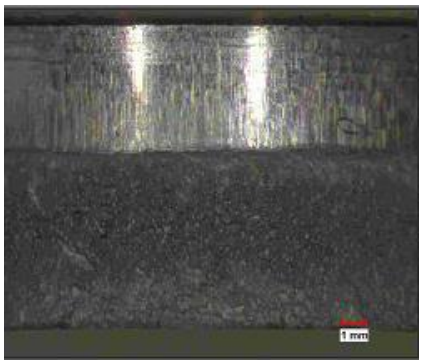

Figure 3.2. Example of punched hole with good quality

The hole expansion test was performed with a Hille Formability Press. To perform the test, the punched hole was placed on top of the forming die with the burr facing up. The coupon was centred over the die and clamped into position under pressure. The die moves at a speed of 1.0 mm/sec and the applied force can reach a maximum of

100 kN. All holes were tested within 1 hour of punching. The sample failure occurs when a crack of approximately 0.1 mm is visible through the thickness of the sheet. The final diameter of the hole was measured from the image where the first crack demonstrating sample failure was seen.

3.3.2 Tensile Testing

The tensile samples were machined by EDM wire machining. ASTM sub-size samples were machined according to the parameters shown in Figure 3.3 and Table 3.7. The grip dimensions varied between the two heats. The samples cut from chemistries A and B had 30 mm grips (i. in Table 3.7). The grip length was increased by 0.5" (12.7 mm) for the second round of tensile samples cut from chemistries C and D to eliminate slip which was observed in some of the samples from chemistries A and B.

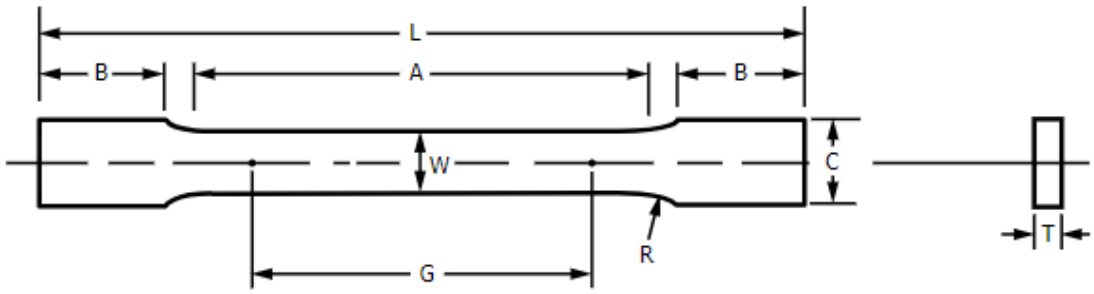

Figure 3.3. Drawing of tensile samples

Table 3.7. Dimensions of sub-size tensile specimens

G	W	T	R (min)	L (min)	A (min)	B (min)	C (approx.)
25.0 ±0.1	6.0 ±0.1	Thickness of material	6	i. 100 ii. 125.4	32	i. 30 ii. 42.7	10

Additionally, the surface of the tensile specimens from chemistries C and D were milled while those from chemistries A and B were not. Surface milling was performed in order to remove the scale which formed during hot rolling.

3.4 Microscopy

Samples for optical and electron microscopy were prepared using regular metallographic mounting, grinding, polishing and etching techniques.

3.4.1 Optical

Samples for optical microscopy were prepared using standard procedures. First the samples were hot mounted in bakelite or cold mounted in epoxy resin, then ground using SiC paper from 500 to 4000 grit. They were then polished using diamond suspension down to 1 or 0.5 μm. The samples were etched using 2% nital to reveal the microstructure. Optical images were taken on a Nikon or Keyence light microscope.

3.4.2 SEM

Samples for SEM imaging were prepared in the same way as for optical imaging. The SEM images were used to determine the morphology, phase fractions and grain size

in the steel. Images were taken using a JEOL 6610 or JEOL 7000 scanning electron microscope. A working distance of 9 to 10 mm at 5 kV were used for imaging.

3.4.3 EBSD

EBSD maps were produced on selected samples as part of the microstructural analysis. A JEOL 7000 SEM was used for the EBSD scans. A step size of 0.05 µm or 50 nm was selected to produce high quality scans and to ensure the detail of the fine microstructure was captured.

3.4.4 TEM

TEM extraction replicas and thin foils were used to characterize precipitates and the morphology of the phases present. Extraction replicas were prepared by mounting grinding and polishing the samples down to 1 µm surface finish. The sample was very lightly etched using 2% nital and a carbon layer was deposited on the surface of the etched sample. To produce the carbon replica, the sample was immersed in 4% nital to strip the carbon film from the surface along with the second phase particles. The carbon replicas were moved from the nital solution on to a copper grid. The precipitates were then analyzed using the PHILIPS CM 12.

Thin foils were used for a more detailed analysis of the microstructure. Thin foils were prepared first by reducing the thickness of a 10 mm by 10 mm sample down to 80 µm by cutting and mechanical polishing. Discs 3 mm in diameter were punched from the thin sheet and jet electropolished in a solution of 10% perchloric acid and methanol at - 40 °C and 16 V. The foils were imaged using the PHILIPS CM12 electron

microscope at 120 kV. Six foils from each sample were analyzed for the morphology of different phases, bainite lath width and precipitate size and distribution.

3.4.5 Atom Probe Tomography

Needles for atom probe tomography analysis were prepared by grinding the sheet down from full thickness to approximately 0.5 mm, targeting the quarter thickness. After producing a sample approximately 15 by 15 mm and 0.5 mm thick, a precision cutter was used to section the sheet into 0.5 mm wide sections, producing square needles approximately 0.5 by 0.5 mm and 15 mm long. The needles were electropolished to produce a fine tip for atom probe tomography analysis.

APT was completed on a LEAP 4000X HR microscope. The scans were performed at approximately 55 K with a specimen temperature of 59.6 K, a 1% detection rate, 250 kHz pulse rate and 60 pJ pulse energy.

3.4.5.1 Electropolishing

Coarse and fine stages of electropolishing were used to produce a fine tip for APT analysis. The coarse stage polishing used a 75% acetic acid and 25% perchloric acid solution. A platinum ring was situated just below the surface of the solution. For coarse electropolishing, 15 to 20 V was used. The platinum ring and sample were connected to the power source and the sample was dipped in and out of the solution in the centre of the platinum ring to thin the sample and produce a sharp tip.

To perform fine stage electropolishing, the needles were mounted in copper tubes. The purpose of this step was to further thin the sample down to a very fine point suitable

for APT analysis. A small platinum ring, approximately 5 mm in diameter was placed under a light microscope. A drop of butoxy ethanol with 2% perchloric acid was placed in the ring. With the power source connected to the platinum ring and to the sample, the sample was moved in and out of the droplet using approximately 20 V. The microscope was focussed on the tip of the sample and was used to monitor the polishing of the tip. After producing the tip, the samples were moved into the APT microscope and stored there under vacuum until analysis.

3.5 Dilatometry

Dilatometry was performed to investigate the phase transformations occurring during hot rolling and the effect of various processing conditions and vanadium additions. The material used for dilatometry analysis was cast and passed through roughing rolling. Cylindrical samples 10 mm long and 5 mm in diameter (Figure 3.4) were machined from the billets using EDM wire machining. Seven different heat treatments and two different chemistries were tested and are outlined in detail in section 4.3. Two samples were tested for each condition for a total of 28 tests. More detail on the tests are available in section 4.3.

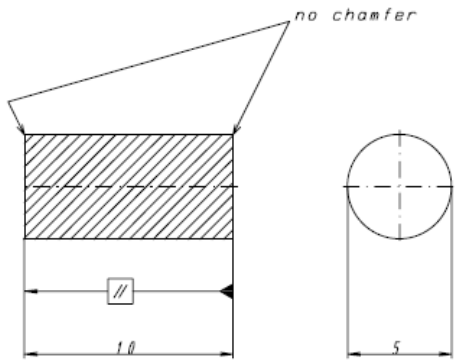

Figure 3.4. Drawing of dilatometry samples

The BÄHR Dilatometer DIL 805A/D at CANMET was used for testing. The specimen was heated by a Cu induction coil and the length change was measured by a linear voltage displacement transducer. The specimens were heated under vacuum and quenched using high purity helium. The DIL805 Win TA 9.0 software package was used to evaluate the data.

Chapter 4

Results

The experimental results are presented in the following chapter. The mechanical properties of the samples are given in section 4.1, microstructural analysis is provided in section 4.2 and dilatometry testing is covered in section 4.3. When discussing combinations of finishing, intermediate and coiling temperatures, the following format will frequently be used: FT-IT-CT or FT-CT (e.g.: 950-630-490 or 890-610).

4.1 Mechanical Properties

Tensile testing was used to measure the UTS, YS and elongation values. The HER was measured from the hole expansion test to assess stretch flangeability of the material. The average mechanical properties are summarized in Table 4.1 and in the following charts. The YS values were determined using a 0.5% offset rather than the 0.2% offset method. A 0.5% offset was used to show clearer trends especially in cases where the tensile curves were rounded and did not display a clear yield point. The

complete tensile curves are available in Appendix A along with the standard deviations of the average mechanical properties.

Table 4.1. Summary of mechanical properties and microstructural characteristics of all samples

FT IT CT	Chem	HER (%)	UTS (MPa)	$YS_{0.5\%}$ (MPa)	TE (%)	UE (%)	Grain Size/ Lath Width (μm)	Martensite %	Bainite %
890 610	A	32	815	655	21	12	N/A	2	<5%
	B	25	843	656	14	9	N/A	11	<5%
	C	32	787	670	18	11	1.8	5	<5%
	D	38	921	849	21	10	2.0	?	<5%
950 610	A	33	800	624	18	10	1.8	10	<5%
	B	25	886	644	18	10	1.6	16	<5%
	C	32	900	700	19	10	1.6	9	<5%
	D	35	1013	882	16	8	1.7	5	<5%
890 490	A	45	818	649	18	9	N/A	4	N/A
	B	35	845	729	17	8	N/A	5	N/A
	C	34	852	652	16	9	N/A	?	N/A
	D	28	945	835	15	7	N/A	?	N/A
950 490	A	58	815	652	18	9	0.54	3	97
	B	44	858	736	13	7	0.49	0	100
	C	32	877	664	18	9	N/A	2	N/A
	D	32	947	762	15	7	N/A	7	N/A
890 630 490	A	48	801	741	16	7	N/A	<5%	~100
	B	48	847	754	18	9	N/A	<5%	~100
	C	35	831	737	16	9	N/A	<5%	~100
	D	37	946	794	15	7	N/A	<5%	~100
950 630 490	A	68	879	835	13	5	N/A	<5%	~100
	B	41	896	799	15	7	0.36	<5%	~100
	C	45	926	882	11	4	0.30	<5%	~100
	D	41	1006	912	14	6	0.33	<5%	~100

The average UTS values are shown in Figure 4.1 and trends related to both chemistry and processing temperatures are evident. Chemistry A (in black) has the lowest UTS values aside from the sample processed at 890-610. The UTS of chemistries B and C (with added carbon and niobium respectively) increase with respect to chemistry A but there is little difference between the two. A large increase in strength is seen in the vanadium containing chemistry across all processing temperatures. The average UTS of all samples from chemistry D is 136 MPa higher than the base chemistry and 101 MPa higher than chemistry C.

The UTS is highest for material processed at 950-610 or 950-630-490 for chemistries B, C and D and surpasses the target of 980 MPa UTS using chemistry D. With a CT of 610 °C, a 950 °C FT produces higher strength material than with a FT of 890 °C for chemistries B, C and D. Averaging the UTS across all chemistries, the samples processed at 950-610 increase in strength by 58 MPa compared to those processed at 890-610 and by 83 MPa when excluding chemistry A. For the samples coiled at 490 °C, the FT appears to have little effect on the UTS. The benefit of a higher FT is seen again for the samples with intermediate cooling where the average UTS across all chemistries for 950-630-490 is 44 MPa higher than the samples processed at 890-630-490.

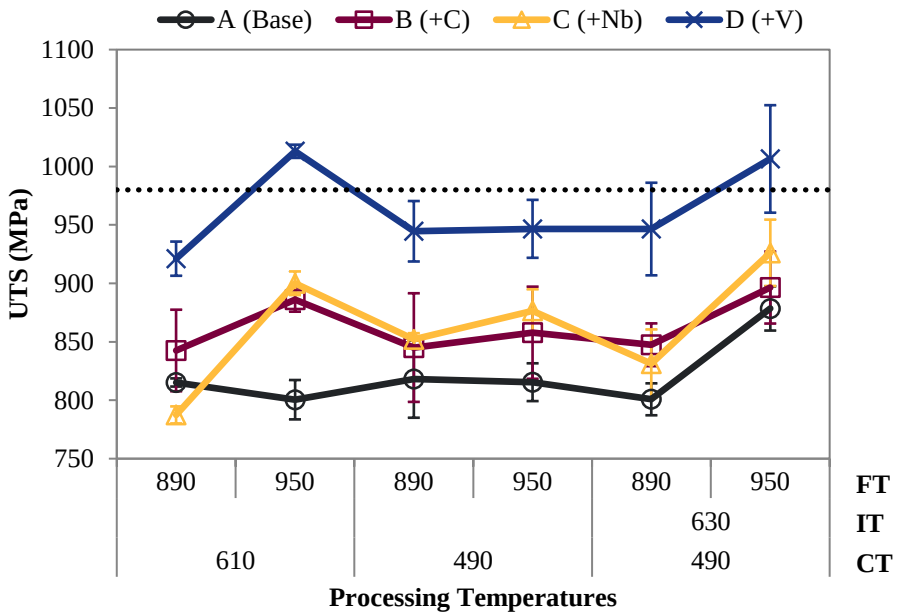

Figure 4.1. Average UTS for all chemistries and heat treatments with error bars showing standard deviation

The average YS values are shown in Figure 4.2. With the addition of vanadium, the YS can surpass the target value of 800 MPa. The vanadium containing material shows a large increase in YS particularly when processed with a 610 °C CT. The average YS for chemistry D processed with a CT of 610 °C is 238 MPa higher than chemistry A and 199 MPa higher than chemistry C. At a CT of 490 °C, the increased carbon content in chemistry B appears to have an important influence on the strength, increasing the YS by about 94 MPa compared to chemistry A. Additionally it can be seen that processing at 950-630-490 produces a high YS for all chemistries. Averaging across all chemistries, the YS is 95 MPa higher for material processed at 950-630-490 as compared to 890-630-490.

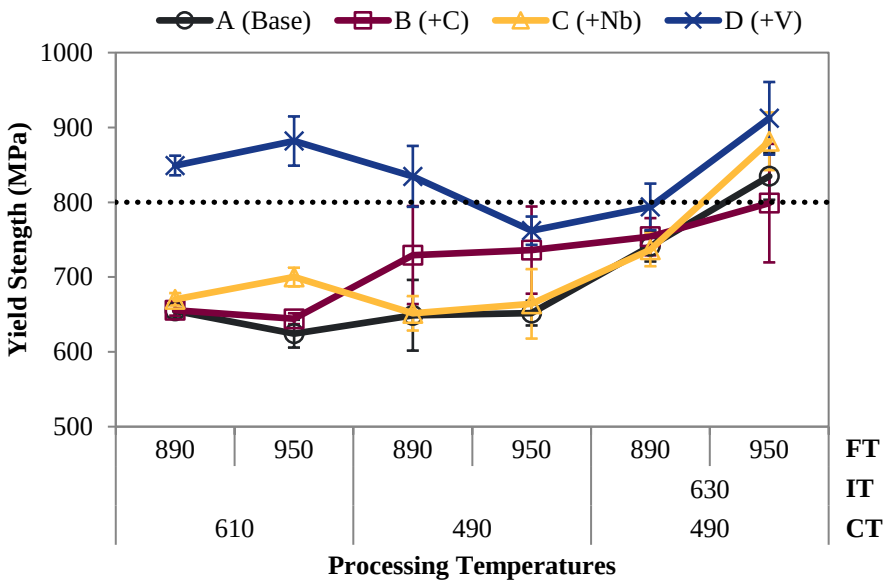

Figure 4.2. Average YS (0.5% offset) for all chemistries and heat treatments with error bars showing standard deviation

It is important to comment on the error bars in the data. In certain cases, the error is quite large and the inconsistency in the tests can be seen in more detail in the complete tensile curves in Appendix A. There are several factors which may have contributed to this. Surface milling was performed to remove rolled in scale but may itself have produced surface defects, or a work hardened surface, causing premature failure and affecting the results. This wide variation in properties of some samples need to be taken into account when interpreting the results.

The hole expansion values are shown in Figure 4.3. The variability in the data is characteristic of the hole expansion test. In general, the HER is highest for the base chemistry although the standard deviation is large in some cases especially for the sample

processed at 950-630-490 which has the highest average HER. The two samples which have HER values above the target of 50% are both from chemistry A and were processed at 950-490 and 950-630-490. The samples processed at 950-630-490 are the only samples from chemistries C and D with an average HER above 40%.

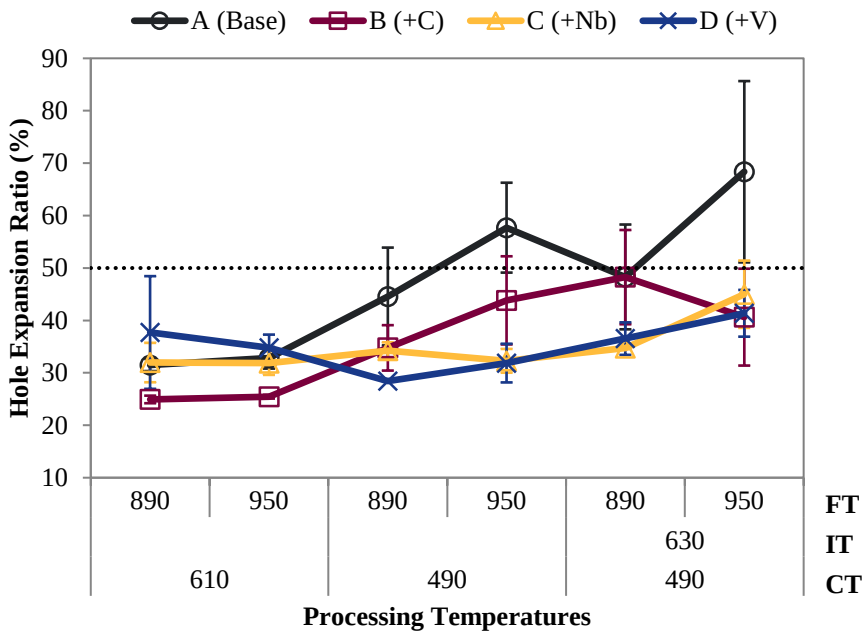

Figure 4.3. Average HER for all chemistries and heat treatments with error bars showing standard deviation

The uniform elongation (UE) and total elongation (TE) values are shown in Figures 4.4 and 4.5 respectively. The average UE values are all above 5% aside from the sample from chemistry C processed at 950-630-490. In general, the elongation values decrease with increasing UTS as can be expected. This is evident for the samples processed 950-610 as compared to 890-610 where, averaging across all chemistries, the UE and TE decrease by 1.1% and 0.8% respectively and the average UTS increases by 58 MPa for a 950 °C FT. This trend is more evident for the samples processed with

intermediate cooling. The UE and TE decrease 2.4% and 3.1% respectively for samples processed at 950-630-490 compared to 890-630-490 while the average UTS increases by 44 MPa. The average TE values ranged from approximately 11% to 21%. The TE values show some variability due to inconsistencies in the tensile curves however the values are all above 10%.

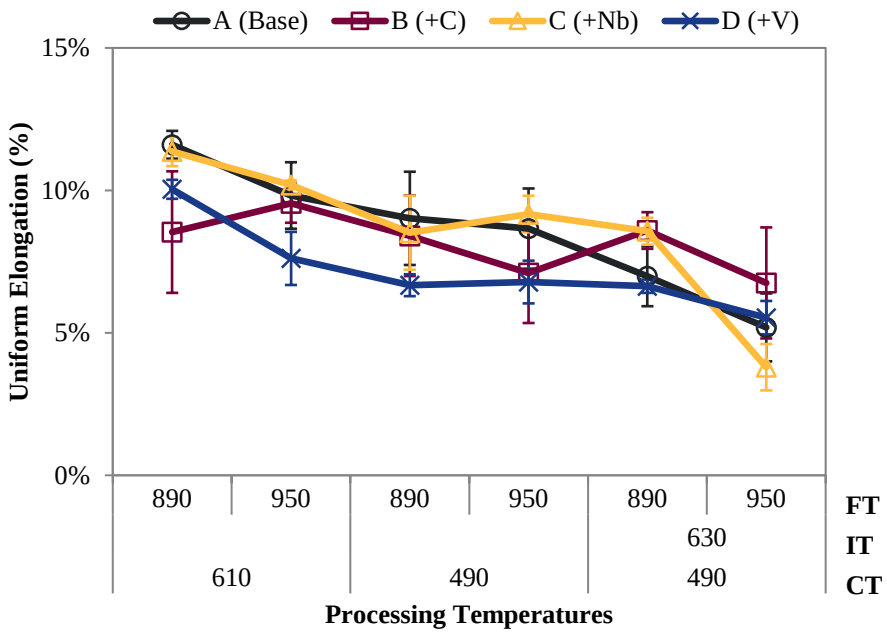

Figure 4.4. Average UE for all chemistries and heat treatments with error bars showing standard deviation

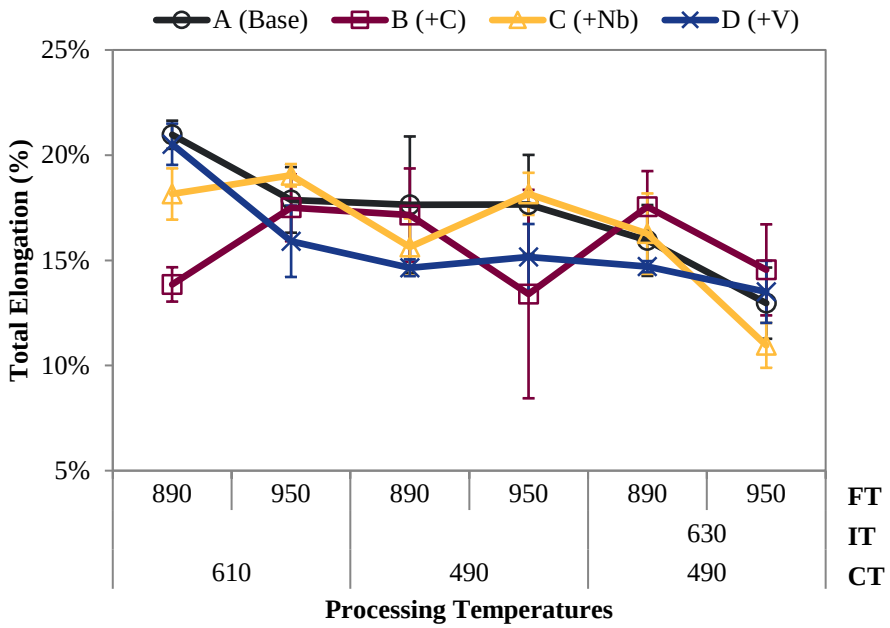

Figure 4.5. Average TE for all chemistries and heat treatments with error bars showing standard deviation

4.2 Microstructural Characterization

The following results are grouped by processing temperatures and show the microstructural analysis performed for the four chemistries within each heat treatment. The processing parameters are presented in the following order: 890-610, 950-610, 890-490, 950-490, 890-630-490, 950-630-490, first investigating material with a CT of 610 °C, followed by samples with a 490 °C CT and finishing with the material processed with intermediate cooling. Special focus is given to the samples which had favourable mechanical properties.

4.2.1 890-610

Samples from all four chemistries were processed with a FT of 890 °C and a CT of 610 °C. All optical and SEM images shown are of the through thickness plane along the rolling direction. Representative optical images for these processing temperatures are provided for chemistry D in Figure 4.6 and are similar to the microstructures of the other chemistries. Figure 4.6 a. and b. shows that banding is present in the sample and is more evident at the center of the sample than at quarter thickness. All samples regardless of processing temperatures displayed banding although to different extents.

In the following sections, one representative SEM image of each microstructure is shown to discuss the sample microstructure. SEM images (Figure 4.7) show that all four chemistries processed at 890-610 have a similar microstructure of ferrite with regions of bainite and martensite. The martensite fraction of chemistry B was the highest of the four chemistries at approximately 11% as determined using image analysis as described in the next paragraph. The other chemistries had martensite fractions less than or approximately equal to 5%. From these images, it appears that the grain size is refined from chemistry A to B with increased carbon and from chemistry C to D with increased vanadium.

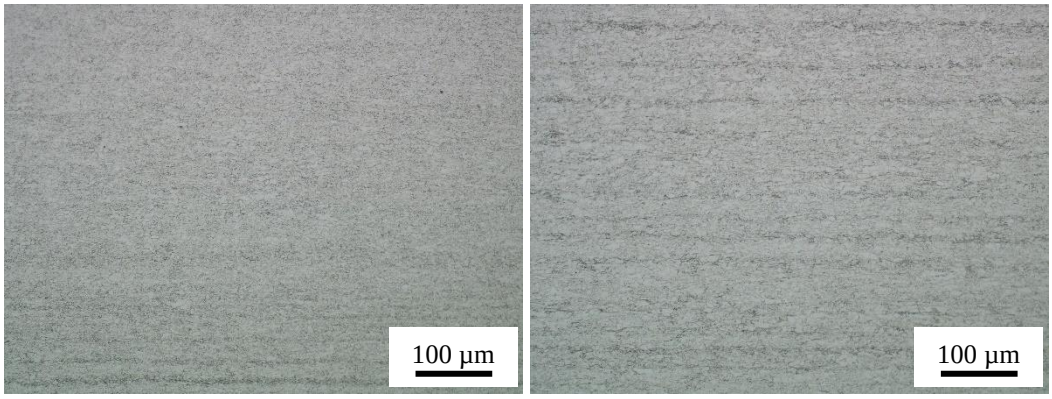

a. 500x magnification at quarter thickness b. 500x magnification at center

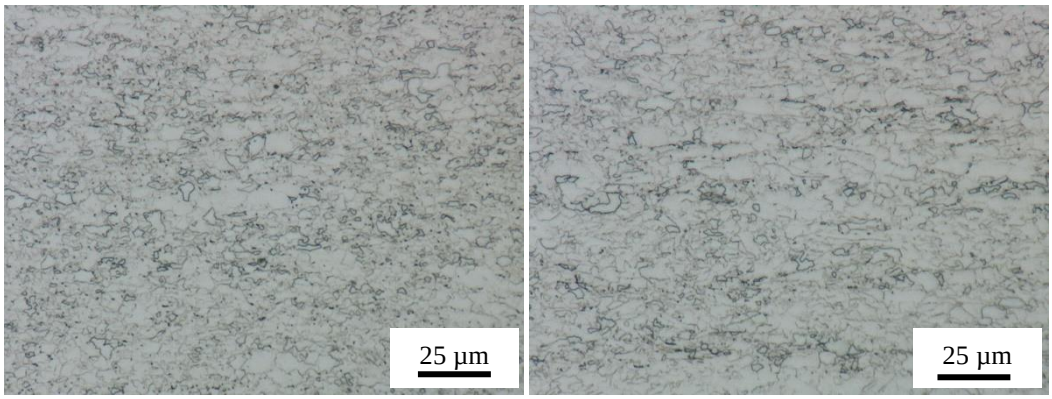

c. 2000x magnification at quarter thickness d. 2000x magnification at quarter thickness

Figure 4.6. Through thickness optical microscopy of chemistry D processed at 950-610

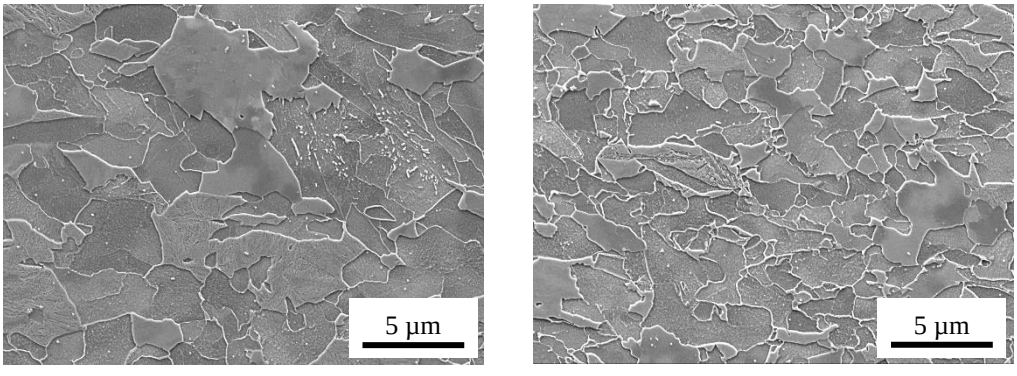

a. Chemistry A (base) at 5000x b. Chemistry B (+C) at 5000x

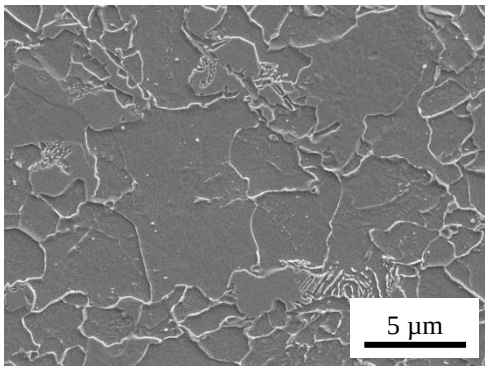

c. Chemistry C (+Nb) at 5000x

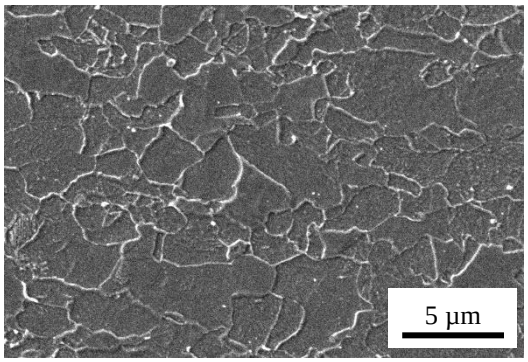

d. Chemistry D (+V) at 5000x

Figure 4.7. SEM images of all chemistries processed at 890-610

Semi-quantitative martensite fractions were determined using the SEM images and are shown in Table 4.1. The values determined using the following method are useful for comparing phase fractions of different samples. Phase fraction determination is necessary for microstructures containing both ferrite and martensite but using nital etched samples, distinguishing between ferrite and martensite was often ambiguous. To identify martensite, the hot rolled samples were tempered for 2 hours at 400 °C to produce tempered martensite which could easily be distinguished from the surrounding ferrite. To quantify the martensite fraction post tempering, ImageJ was used to trace the tempered martensite regions in five SEM images taken at 5000x magnification. The images were taken from the surface to centre of the sample to account for any variation in the microstructure through the thickness of the strip. Figure 4.8 illustrates this method of martensite fraction determination using an example from chemistry C processed at 950-610.

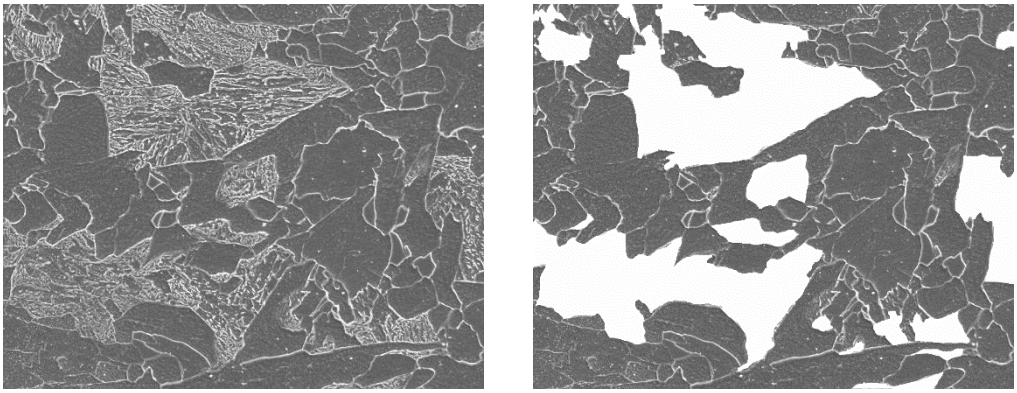

a. Example of tempered martensite post tempering heat treatment

b. Determining martensite fraction using ImageJ

Figure 4.8. Martensite fraction determination by tempering

4.2.2 950-610

The next samples were processed at 950-610, using a higher FT than the previous samples but with the same CT. The SEM images are shown in Figure 4.9. The phase morphology is similar to those with a FT of 890 °C showing ferrite with some regions of martensite and bainite. These samples have higher martensite fractions than the material processed at 890-610. Chemistry B again has the highest martensite fraction at approximately 16%. Using the linear intercept method on four images taken through the thickness of the sample at 5000x magnification, the grain size was estimated between 1.6 and 1.8 µm for the four chemistries.

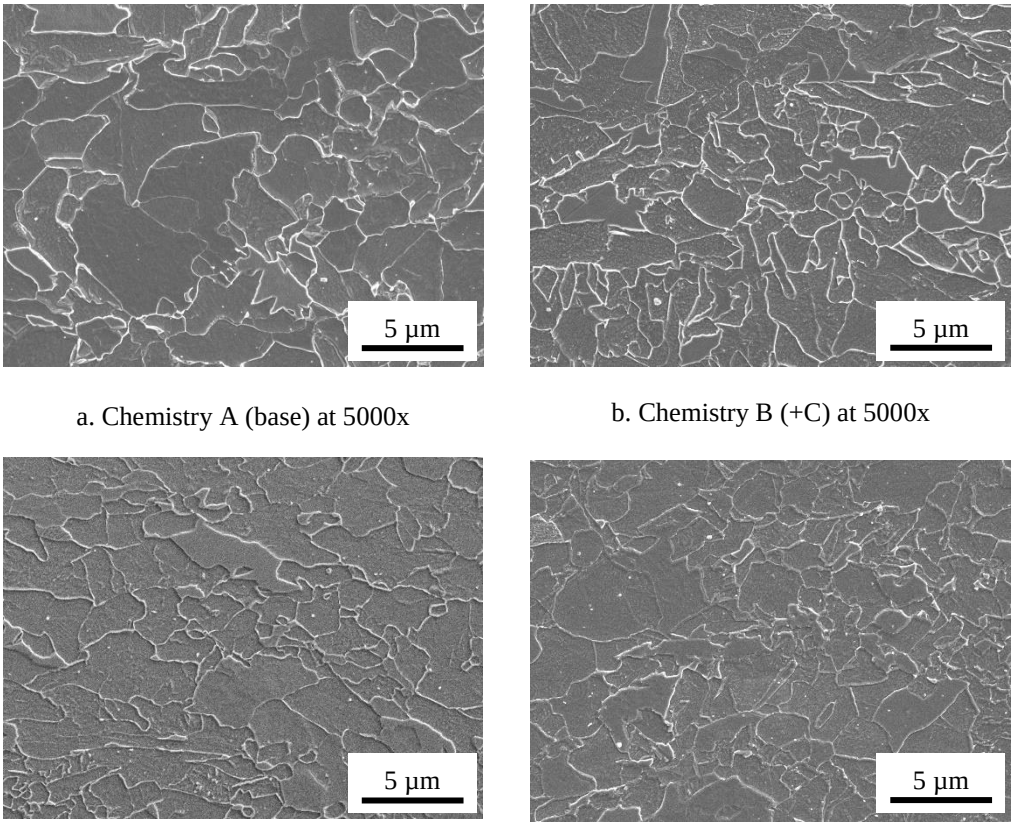

a. Chemistry A (base) at 5000x

b. Chemistry B (+C) at 5000x

c. Chemistry C (+Nb) at 5000x

d. Chemistry D (+V) at 5000x

Figure 4.9. SEM images of all chemistries processed at 950-610

Since the material processed at these temperatures has high strength, further microstructural analysis was completed to determine the strengthening mechanisms. The vanadium containing sample which had the best properties was analyzed using EBSD to investigate phase morphology (Figure 4.10). Figure 4.10 a. shows ferrite along with regions of poor band contrast which could be a result of higher dislocation density and may be martensitic regions. With the linear intercept method, the average grain size measured using EBSD is 1.6 µm or 1.8 µm at a critical misorientation angle of 5° or 10°

respectively. The grain size measured manually is 1.7 µm which confirms the accuracy of manual measurements.

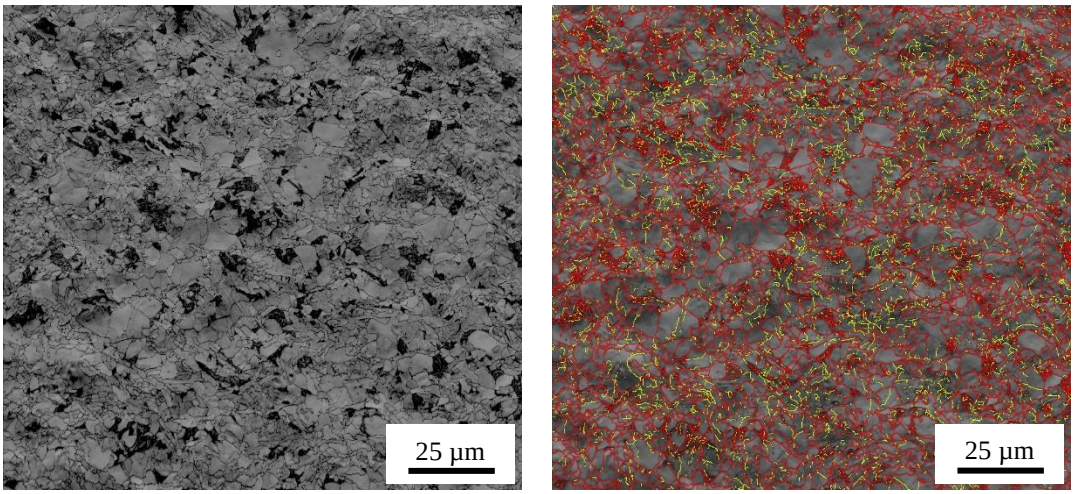

a. Band contrast map of chemistry D at 700x magnification

b. Grain boundary map with HAGB (≥15°) shown in red and LAGB in yellow

Figure 4.10. EBSD maps of chemistry D processed at 950-610

These processing conditions were expected to produce a ferritic microstructure with microalloyed interphase precipitates. TEM extraction replicas and thin foils were used to further characterize the microstructure and precipitation in chemistries C and D which contain additional niobium and vanadium respectively.

The thin foils show that both samples have similar microstructures consisting of complex ferrite with an irregular morphology and dislocation cell structure (Figure 4.11). Additional images are available in Appendix B. A very small fraction of a minor second martensite/austenite (M/A) phase is present in chemistry D. Qualitatively it was seen that fraction of the second M/A was slightly higher in chemistry C. Both samples contain some regions of lath ferrite or bainite.

Chemistry C

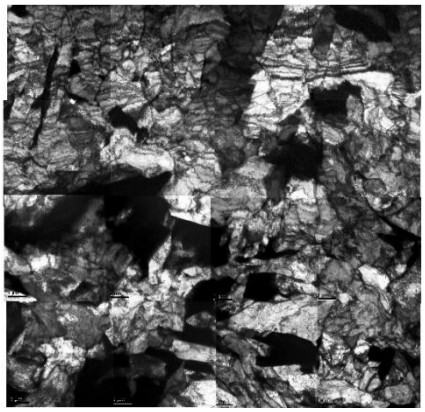

Chemistry D

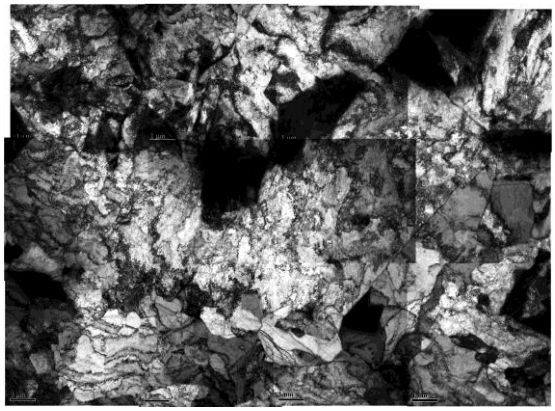

a. Overview of degenerate ferrite at low magnification including dark M/A regions

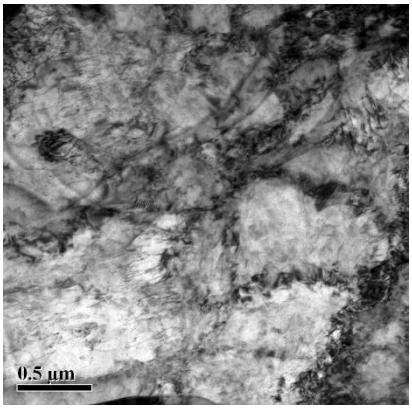

b. Dislocation sub-structure within ferrite

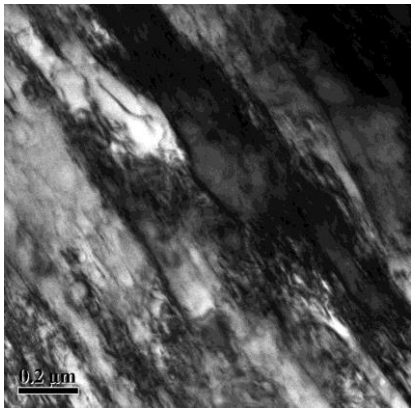

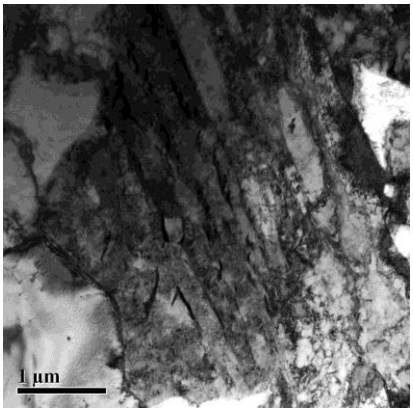

c. Regions of lath ferrite or bainite

Figure 4.11. TEM thin foil analysis of chemistries C and D processed at 950-610

Coarse square shaped precipitates and fine round precipitates are present in both samples (Figure 4.12). Additional images are available in Appendix B. Rows of fine precipitates were found in chemistry D with nearly constant row spacing parallel to the ferrite grain boundaries. In contrast, rows of precipitates were not found in chemistry C, but random distributions of fine precipitates exist and were found interacting with dislocations.

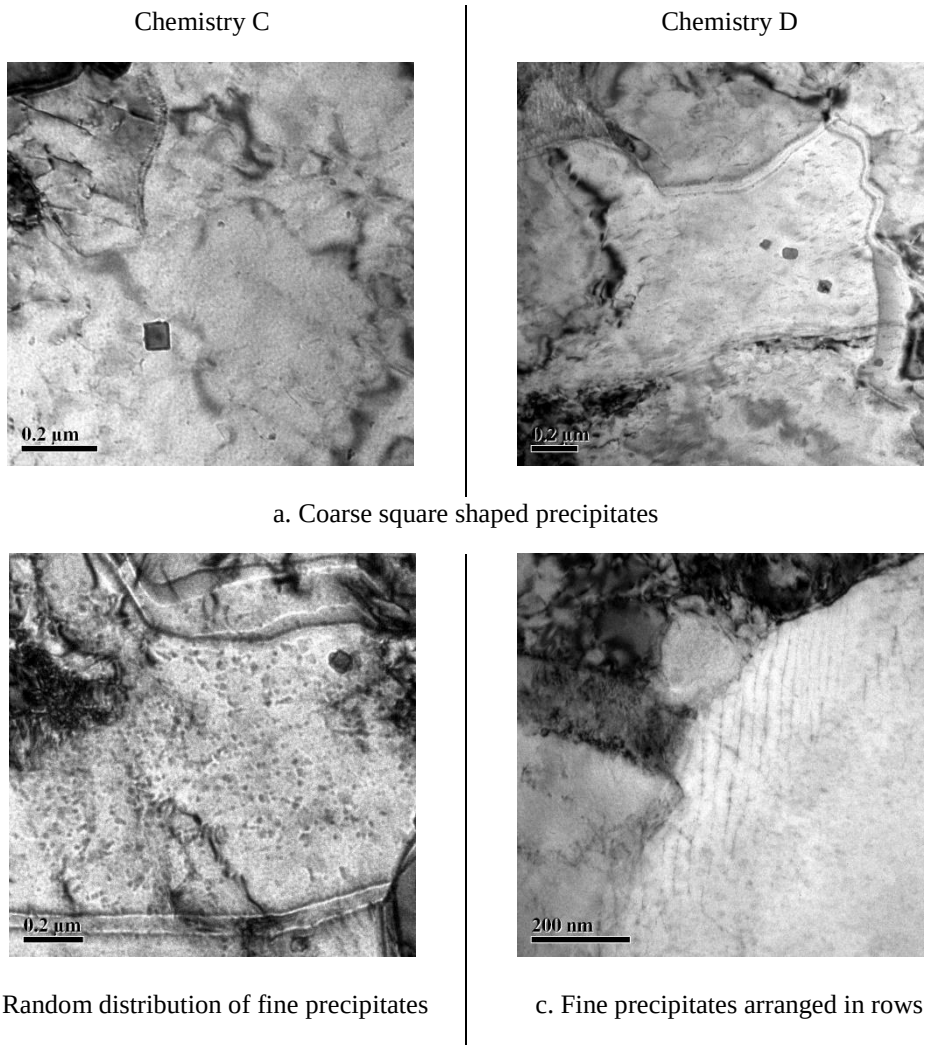

Figure 4.12. Precipitates found in TEM thin foil analysis of chemistries C and D processed at 950-610

Extraction replicas were used to quantitatively determine the distribution of coarse and fine precipitates in these samples. Chemistry D contains coarse and fine particles with square shape, quasi-square shape and elongated rods. Figure 4.13 a. shows a random distribution of both coarse and fine particles. Higher magnification images of these particles are shown in Figure 4.13 b. and c.

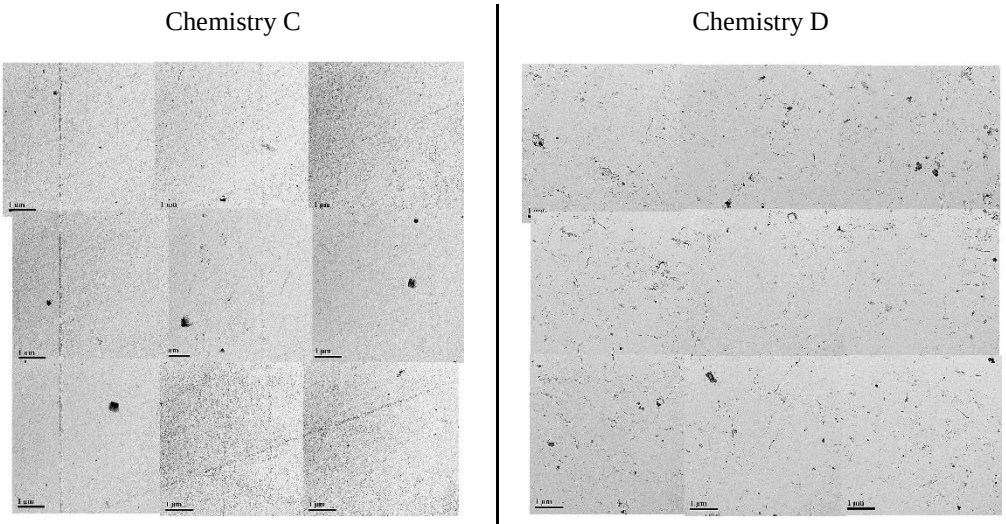

a. Low magnification of both coarse and fine preciptiates

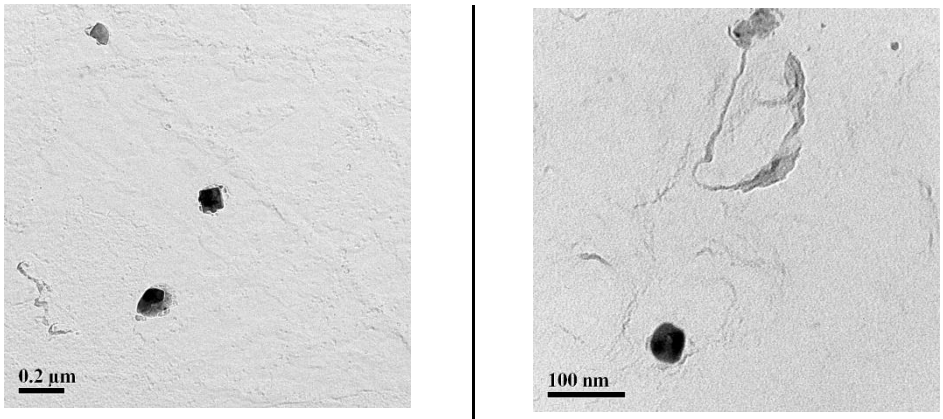

b. Coarse square shaped particles

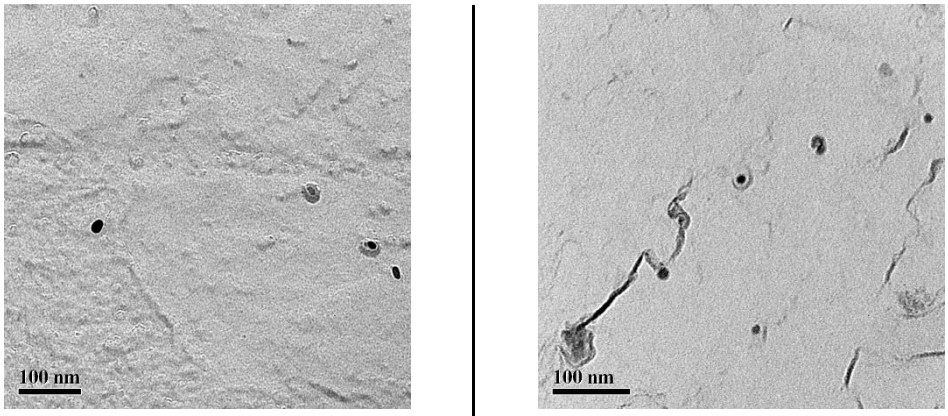

c. Fine round shaped particles

Figure 4.13. TEM extraction replicas of chemistries C and D processed at 650-610

The analysis was used to provide a particle size distribution. High and low magnification images were used to identify small and large particles respectively. The distribution in Figure 4.14 shows a much higher frequency of particles less than 10 nm in diameter in chemistry D.

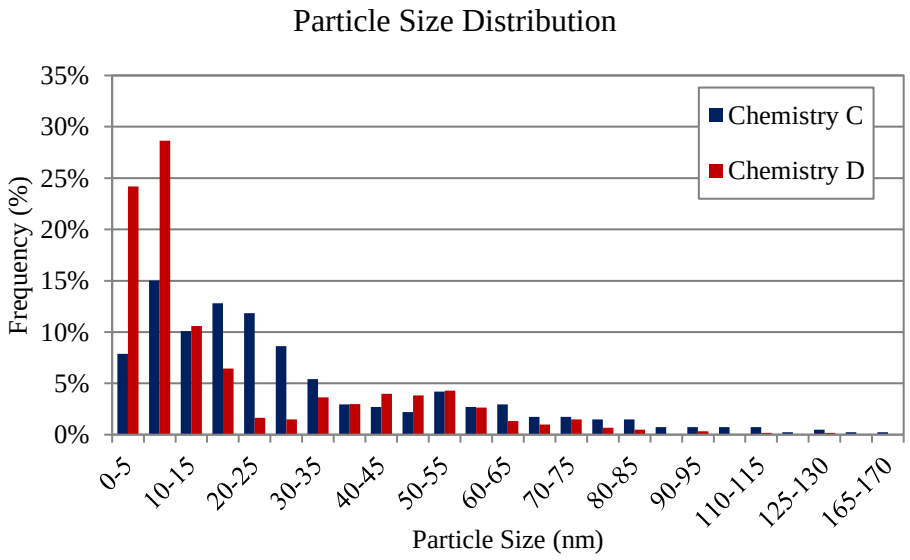

Figure 4.14. Distribution of particle size in chemistries C and D processed at 950-610

Atom probe tomography was conducted on these two samples to complement the TEM analysis. APT provides information on how the precipitates are arranged throughout the sample and their composition.

Two APT datasets were produced for chemistry C. Dataset 1 (Figure 4.15) shows two distinct regions, a high C and a low C region with some areas of C segregation. The C density with 1 at% Nb isosurfaces is seen in Figure 4.15 b., providing evidence of Nb precipitation in the low C region which does not exist in the high C region. Since ferrite and martensite regions were seen in SEM and TEM analysis, it can be concluded that the low C region is ferritic and contains niobium carbides and the high C region is martensitic. The compositions within the two regions of interest (ROI) in Figure 4.15 c. are provided in Table 4.2. The carbon levels of the high and low C regions are 2.18 at% and 0.09 at% respectively.

The second dataset from this sample also shows C segregation (Figure 4.16). Nb segregation is seen but appears to be more significant in certain regions of the sample as observed by the Nb isosurfaces along the top of Figure 4.16 b. Additional images are available in Appendix B.

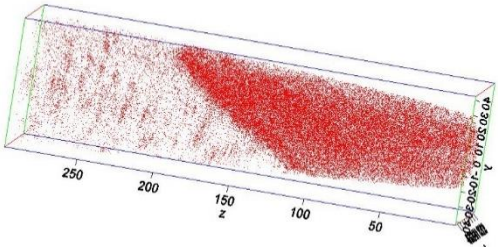

a. Dot map showing carbon density

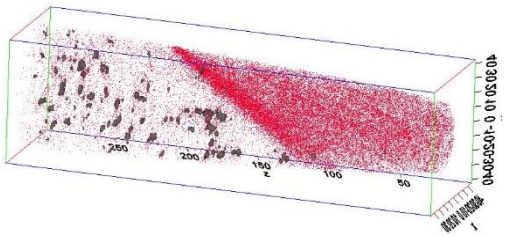

b. Carbon density in red with 1 at% Nb isosurfaces in grey

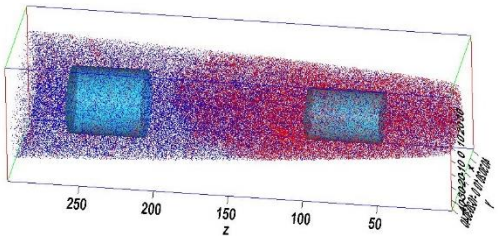

c. Two ROI's used for composition analysis

Figure 4.15. Atom probe dataset 1 from chemistry C processed at 950-610

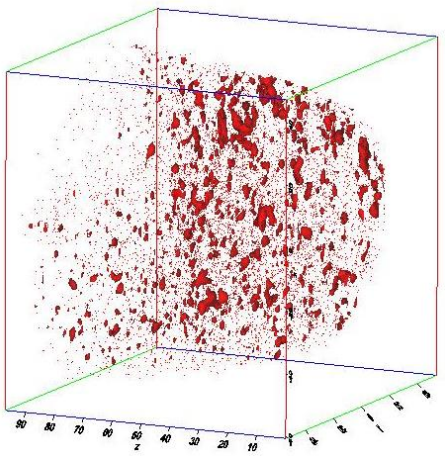

a. C density with 1.5 at% C isosurfaces

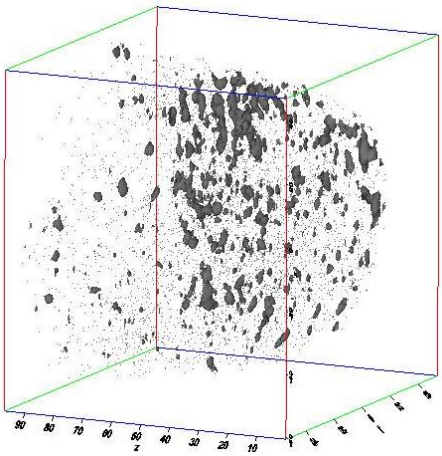

b. Nb density with 0.5 at% Nb isosurfaces

Figure 4.16. Atom probe dataset 2 from chemistry C processed at 950-610

The compositions in Table 4.2 show that dataset 2 from chemistry C is most similar in composition to the low carbon ROI in dataset 1 providing evidence that dataset 2 is also from within a ferrite grain.

Table 4.2. Concentration of elements in APT datasets from chemistries C and D processed at 950-610

	Chemistry C				Chemistry D	
	Dataset 1			Dataset 2	Dataset 1	Dataset 2
Element	**Bulk**	**High C ROI**	**Low C ROI**	**Bulk**	**Bulk**	**Bulk**
Fe	95.4%	94.3%	96.5%	96.6%	96.2%	96.3%
Mn	2.0%	1.9%	1.9%	1.8%	2.0%	1.9%
C	1.0%	2.2%	0.1%	0.1%	0.2%	0.1%
Cr	0.3%	0.3%	0.3%	0.3%	0.3%	0.3%
V	0.0%	0.0%	0.0%	0.0%	0.2%	0.2%
Mo	0.1%	0.1%	0.1%	0.1%	0.1%	0.1%
Nb	0.03%	0.03%	0.02%	0.02%	0.02%	0.03%

Two datasets were analyzed from chemistry D and are pictured in Figure 4.17 and 4.18. The chemical composition of these two datasets are also shown in Table 4.2 and are similar to the composition of the ferritic regions of chemistry C. The images of the second dataset in Figure 4.18 show C, Nb and V isosurfaces located in similar regions, providing evidence of co-segregation of these elements. Additional images are available in Appendix B.

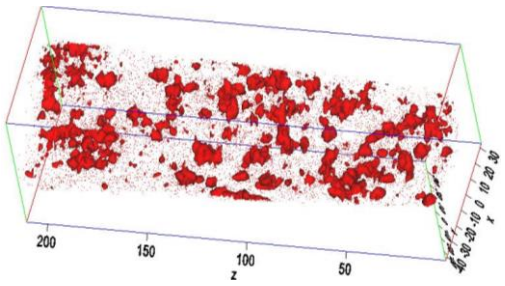

a. C density with 1.5 at% C isosurfaces

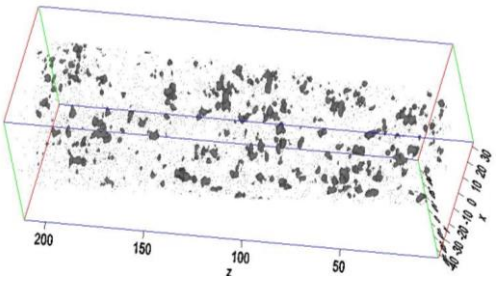

b. Nb density with 0.5 at% Nb isosurfaces

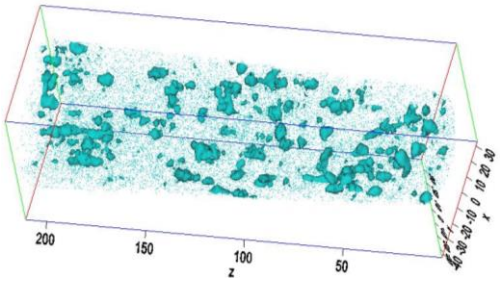

d. V density with 2 at% V isosurfaces

Figure 4.17. Atom probe dataset 1 from chemistry D processed at 950-610

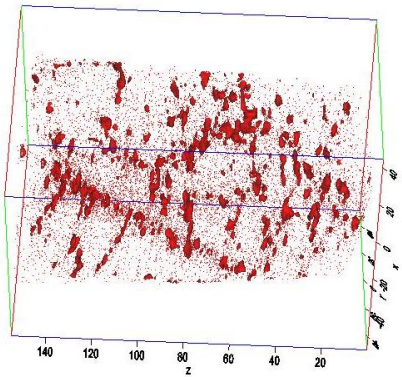

a. C density with 1.5 at% C isosurfaces

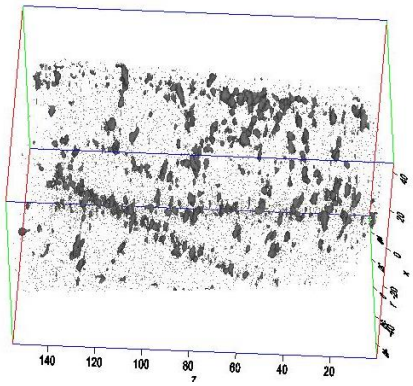

b. Nb density with 0.5 at% Nb isosurfaces

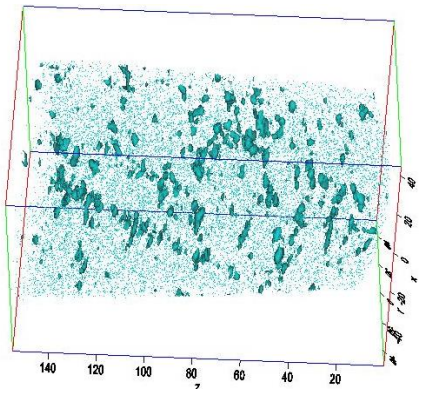

c. V Density with 1 at% V isosurfaces

Figure 4.18. Atom probe dataset 2 from chemistry D processed at 950-610

4.2.3 890-490

This section shows the microstructure of samples processed with a low FT and low CT. The optical microscopy images in Figure 4.19 below show chemistry D and can be compared to the ferritic samples processed at 890-610 in Figure 4.6. It is evident that the low CT produces a bainitic microstructure instead of a ferritic microstructure.

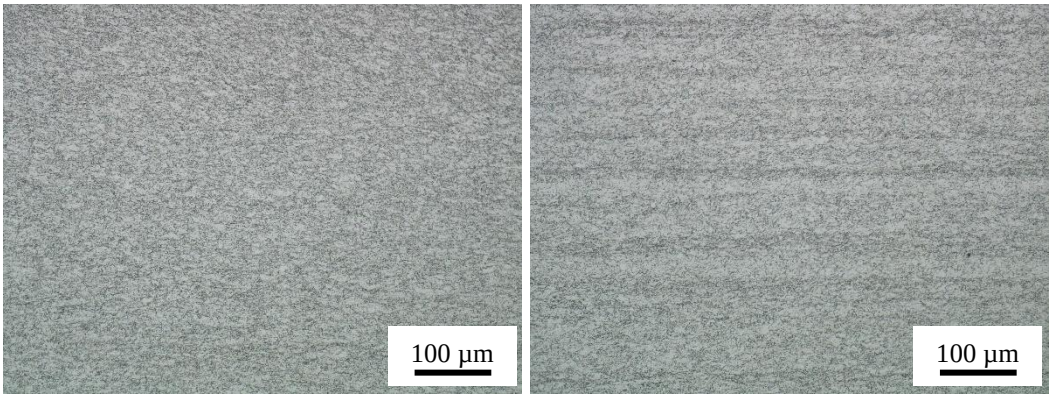

a. 500x magnification at quarter thickness b. 500x magnification at center

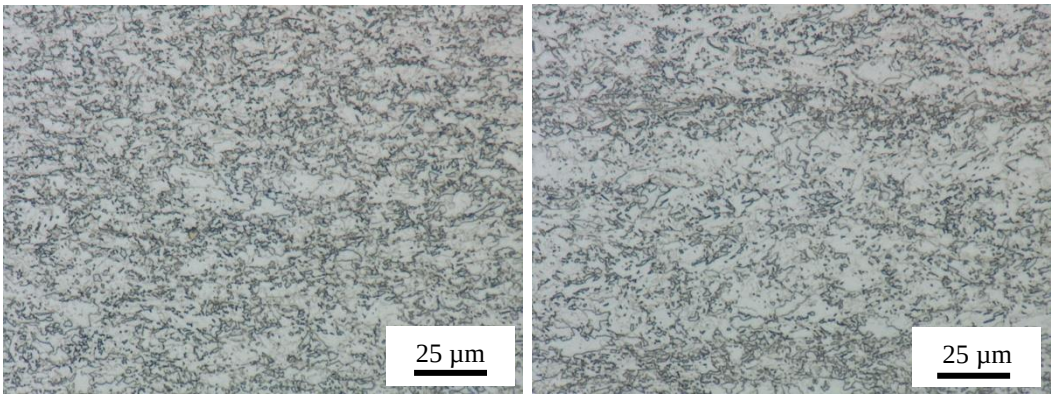

c. 2000x magnification at quarter thickness d. 2000x magnification at quarter thickness

Figure 4.19. Through thickness optical microscopy of chemistry D processed at 890-490

The SEM images in Figure 4.20 show a much finer microstructure than was present at 610 °C CT especially in chemistry B. The morphology is irregular. In some images, laths are visible but the microstructure is largely irregular ferrite or granular bainite. It is important to note that these samples were the third samples placed in the coiling simulation furnace so they were cooled immediately upon being placed in the furnace. This will be discussed further in the context of the samples processed at 950-490.

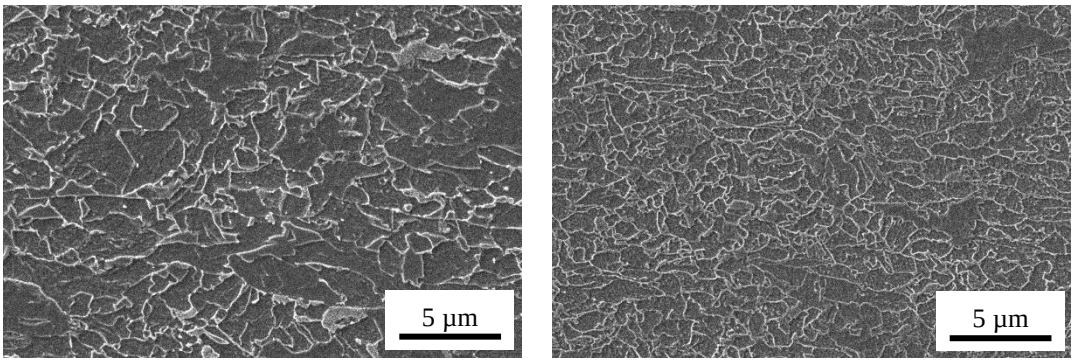

a. Chemistry A (base) at 5000x b. Chemistry B (+C) at 5000x

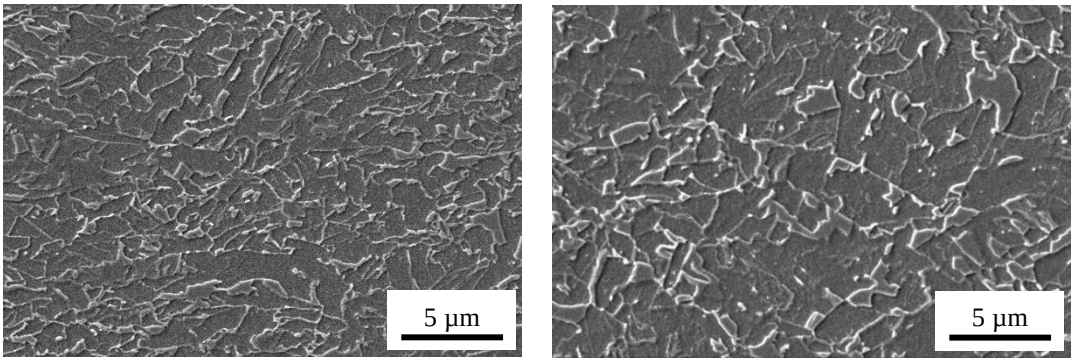

c. Chemistry C (+Nb) at 5000x d. Chemistry D (+V) at 5000x

Figure 4.20. SEM images of all chemistries processed at 890-490

4.2.4 950-490

The effects of a higher FT on a bainitic microstructure are investigated next. Images taken using optical microscopy look very similar to the previous sample with a lower FT of 890 °C. With a low CT, a bainitic structure is produced. The SEM images in Figure 4.21 demonstrate that two different bainite morphologies are present in the samples. Chemistries A and B have a very clear lath structure while chemistries C and D have an irregular morphology. It should be noted that the samples from chemistries C and D were the second samples to be placed in the furnace. As a result, they were held for approximately one hour at the CT of 490 °C before being cooled to room temperature. This isothermal hold could have influenced the bainite morphology. See Chapter 5 for a more detailed discussion.

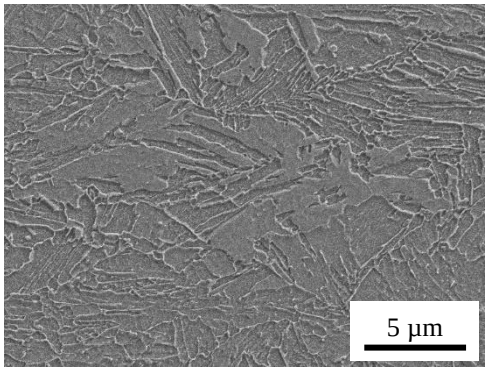

a. Chemistry A (base) at 5000x

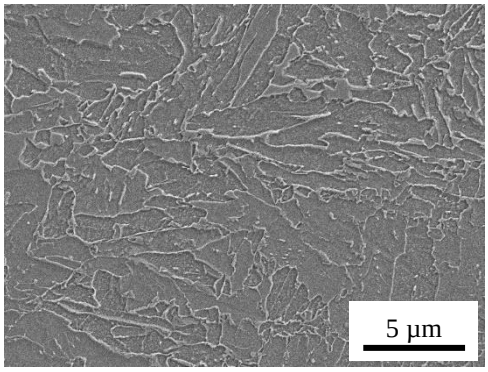

b. Chemistry B (+C) at 5000x

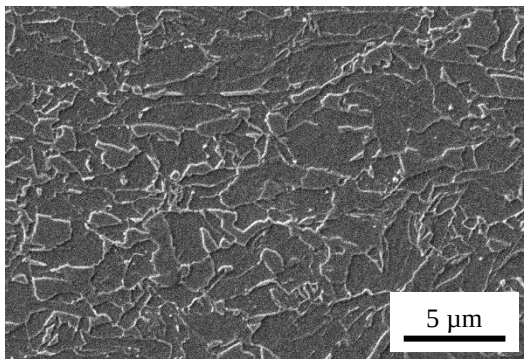

c. Chemistry C (+Nb) at 5000x

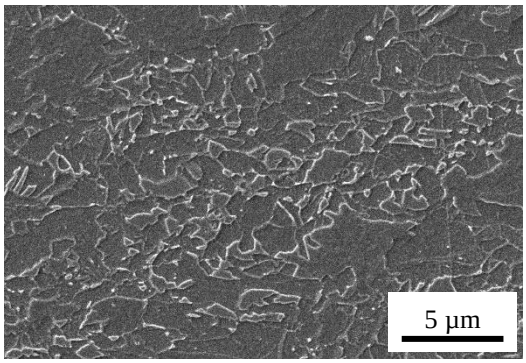

d. Chemistry D (+V) at 5000x

Figure 4.21. SEM images of all chemistries processed at 950-490

EBSD analysis was performed on chemistries A and B and are shown in Figure 4.22. Using the linear intercept method, the average grain size of chemistries A and B are 1.7 µm and 1.5 µm respectively using a critical misorientation angle of 5°. Using the multiplier from Hell at al. [32] in equation (1.19) which accounts for inaccuracies in the EBSD measurements of bainite lath width, the lath width measurements can be adjusted to 0.54 µm and 0.49 µm for chemistries A and B respectively. The band contrast images also show that chemistry B contains more regions of poor band contrast which could be martensitic regions or areas with relatively high dislocation density.

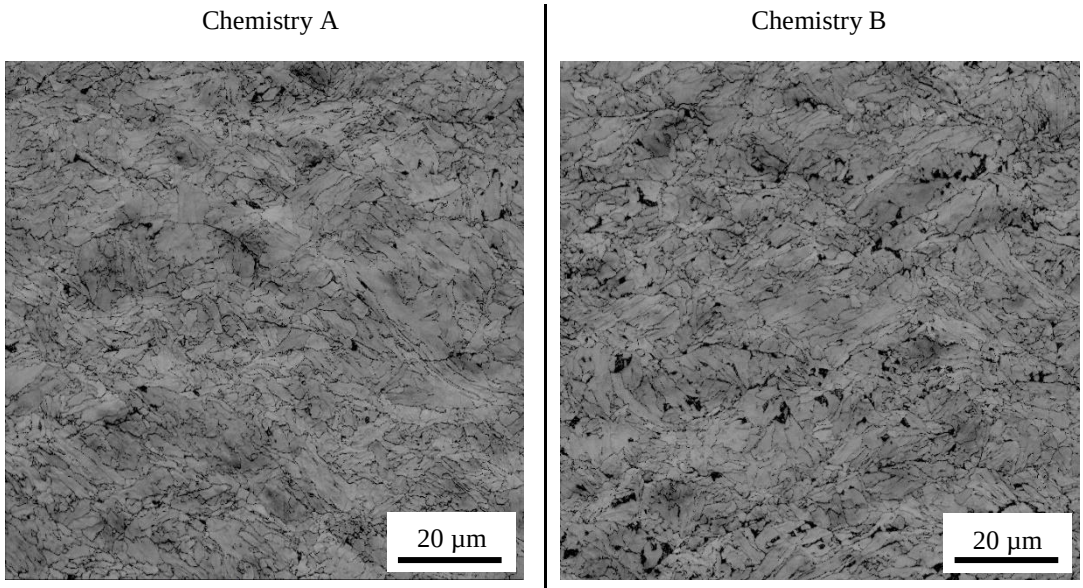

a. Band contrast map at 700x magnification

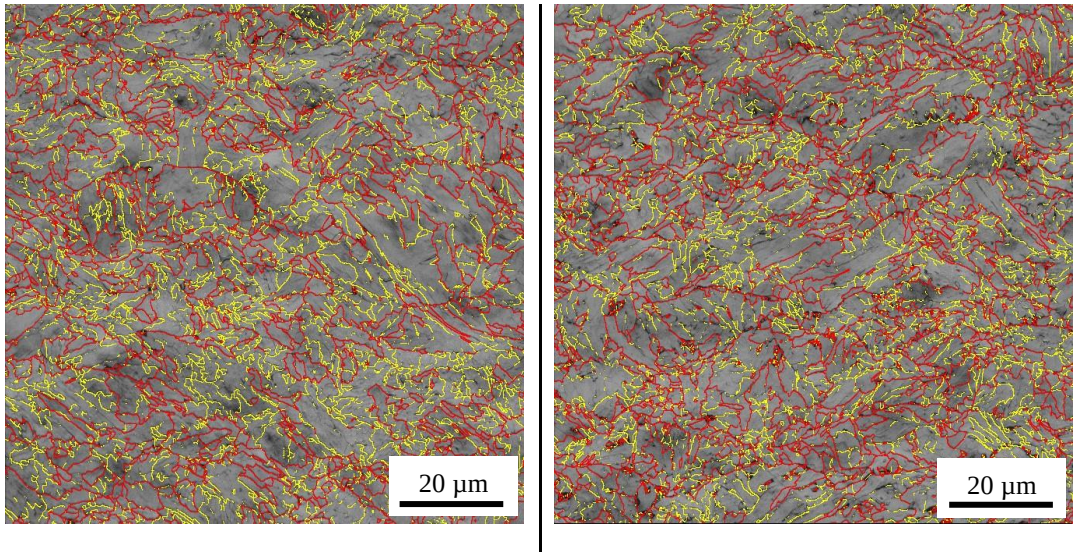

b. Grain boundary map with HAGB (≥15°) shown in red and LAGB in yellow

Figure 4.22. EBSD maps of chemistries A and B processed at 950-490

For a thorough analysis of the effect of CT without intermediate cooling, thin foil TEM analysis was completed on the sample from chemistry D (Figure 4.23). The microstructure consists mostly of irregular or degenerate ferrite with a dislocation cell

structure. A minor granular second M/A phase is also present along with some regions of lath ferrite or bainite. No precipitates are found in the microstructure.

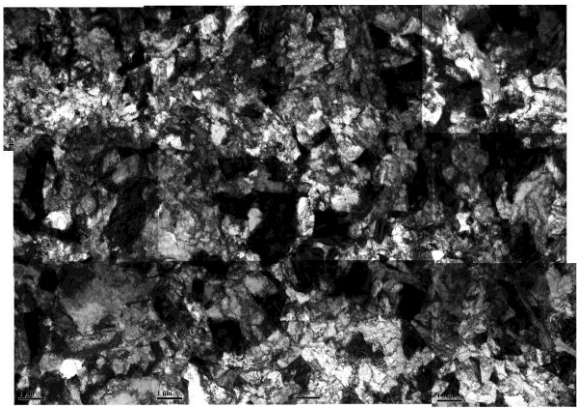

a. Overview of degenerate ferrite at low magnification include black M/A regions

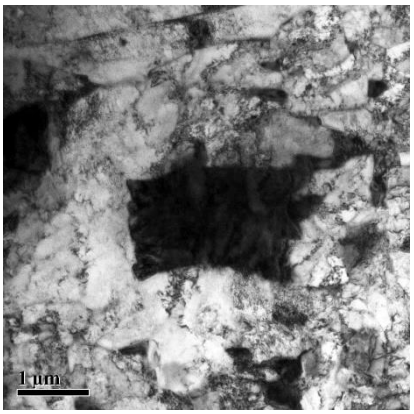

b. Higher magnification of M/A region

c. Dislocation sub-structure within ferrite

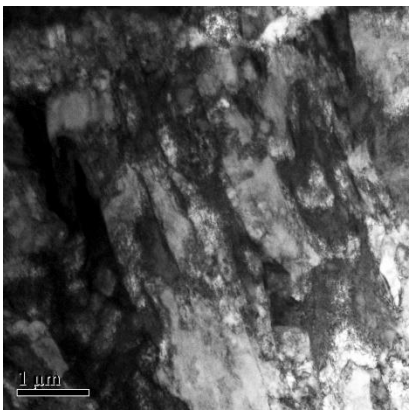

d. Regions of lath ferrite or bainite

Figure 4.23. TEM thin foil analysis of chemistry D processed at 950-490

Two atom probe tips from the vanadium containing material were analyzed to provide more detail on the composition and arrangement of atoms within the material. The first tip in Figure 4.24 a. contained a high and low carbon region, likely showing the presence of both martensite and ferrite. The compositions of both regions were determined using ROI's (Figure 4.24 b.) and the results are displayed in Table 4.3.

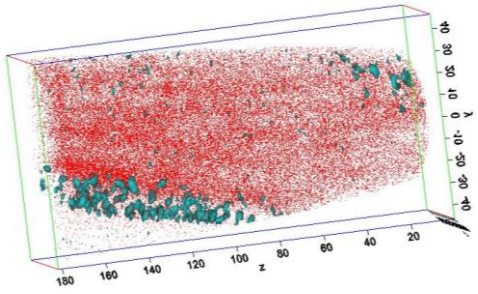

a. Carbon density in red with 1 at% V isosurfaces

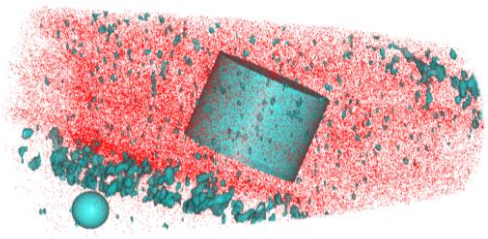

b. Two ROI's used for composition analysis

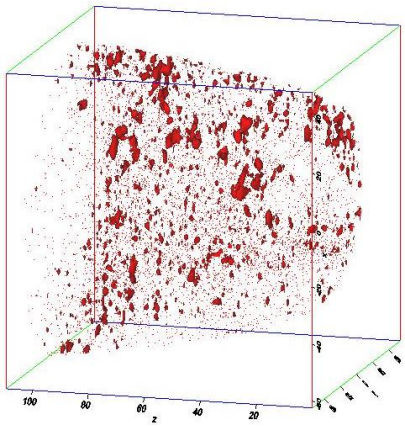

c. C density with 1 at% C isosurfaces

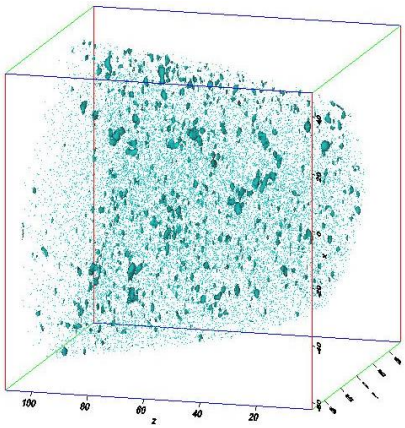

d. V density with 0.8 at% V isosurfaces

Figure 4.24. Atom probe datasets 1 (a,b) and 2 (c,d) from chemistry D processed at 950-490

Table 4.3. Concentration of elements in atom probe datasets 1 from chemistry D processed at 950-490

Element	Bulk	High C ROI	Low C ROI
Fe	94.4%	94.3%	96.4%
Mn	2.0%	2.0%	1.8%
C	1.9%	1.9%	0.1%
Cr	0.3%	0.3%	0.3%
V	0.2%	0.2%	0.2%
Mo	0.1%	0.1%	0.1%
Nb	0.03%	0.03%	0.02%

Figure 4.24 a. shows the carbon density with vanadium isosurfaces of 1 at%. The vanadium isosurfaces are concentrated outside of the interface between the high and low carbon region. The effect of processing temperatures on the segregation of vanadium in this sample is discussed in Chapter 5.

Dataset 2 shows some regions of carbon and vanadium segregation (Figure 4.24 c. and d.) Niobium was largely segregated on the poles which is an artefact of the reconstruction. The vanadium isosurfaces demonstrate that vanadium is not evenly distributed through the matrix.

4.2.5 890-630-490

The following section show the effects of intermediate cooling with a low FT and low CT. These results can be compared to the samples directly cooled from finishing to the CT to see the effects of intermediate cooling. The optical images are shown in Figure 4.25 and the SEM images in Figure 4.26. A FT of 890°C is below the no-recrystallization temperature so that some of the strain applied during rolling is retained in the austenite, resulting in pancaked grains. The structure in Figure 4.25 c. appears more pancaked than the sample in Figure 4.27 a. which has a higher FT of 950 °C.

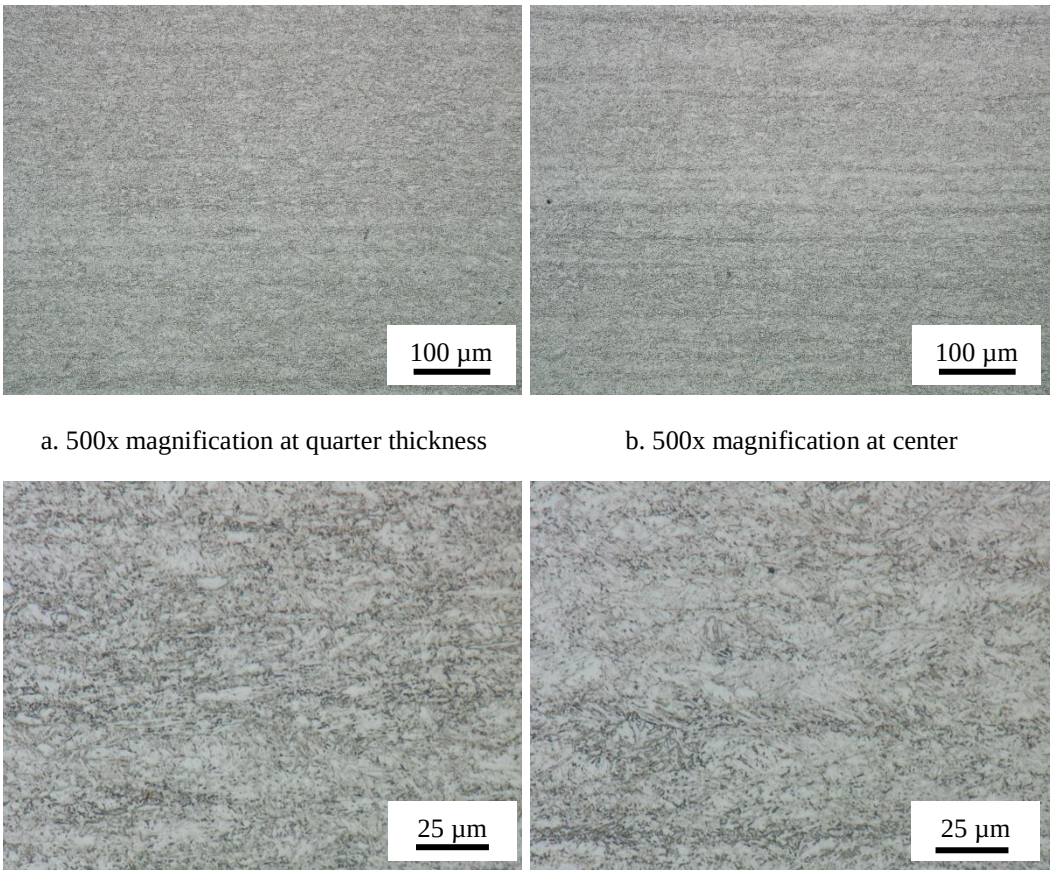

a. 500x magnification at quarter thickness b. 500x magnification at center

c. 2000x magnification at quarter thickness d. 2000x magnification at quarter thickness

Figure 4.25. Through thickness optical microscopy of chemistry D processed at 890-630-490

The SEM images show that the bainite is composed of both laths and irregularly shaped bainite. There appear to be more laths present in these samples as compared to the material without intermediate cooling shown in Figure 4.20. Chemistry D (Figure 4.26 d.) seems to have a finer structure than the other chemistries.

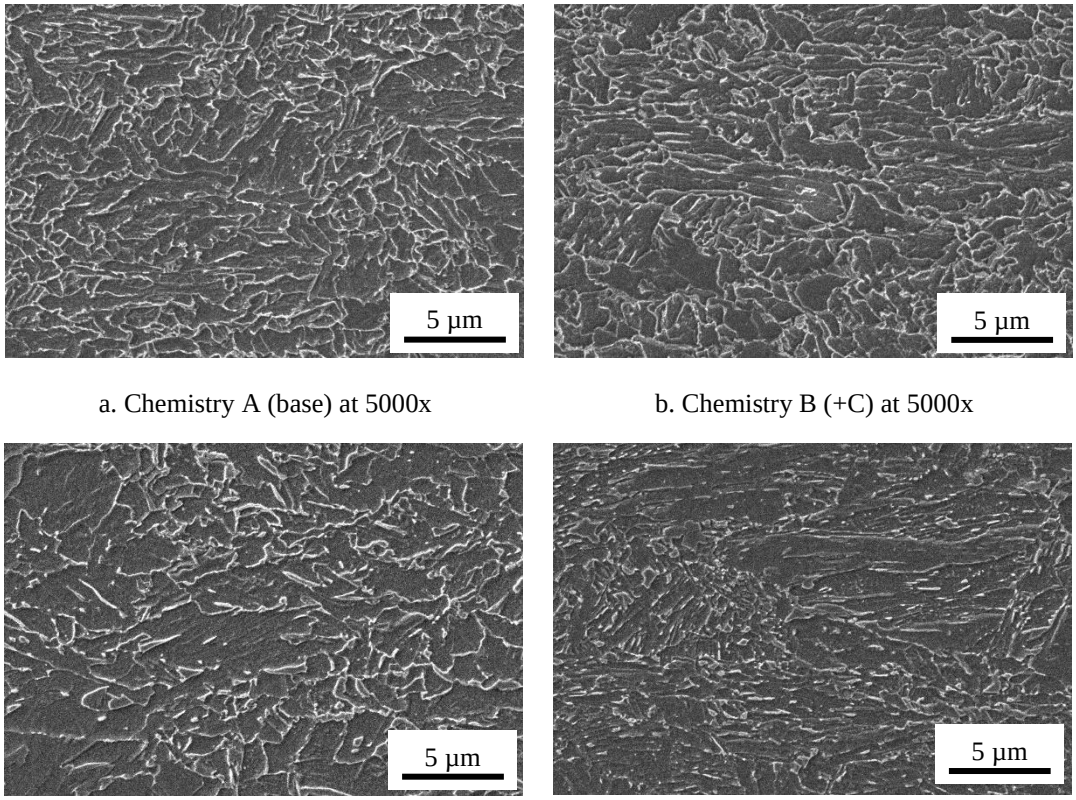

a. Chemistry A (base) at 5000x

b. Chemistry B (+C) at 5000x

c. Chemistry C (+Nb) at 5000x

d. Chemistry D (+V) at 5000x

Figure 4.26. SEM images of all chemistries processed at 890-630-490

4.2.6 950-630-490

The final processing parameters to be discussed involved intermediate cooling with a high FT. Very similar observations are made for this sample as the above sample but as mentioned, there seems to be less pancaking present in this microstructure, especially based on the optical images taken at quarter thickness (Figure 4.27 a.).

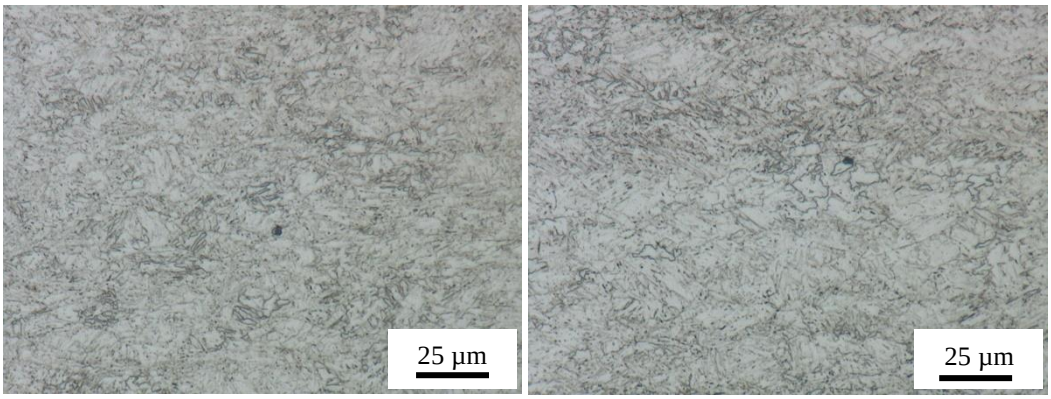

a. 2000x magnification at quarter thickness b. 2000x magnification at quarter thickness

Figure 4.27. Through thickness optical microscopy of chemistry D processed at 950-630-490

SEM images (Figure 4.28) show a majority of lath bainite with some regions of granular bainite. The four different chemistries appear to be quite similar based on SEM imaging.

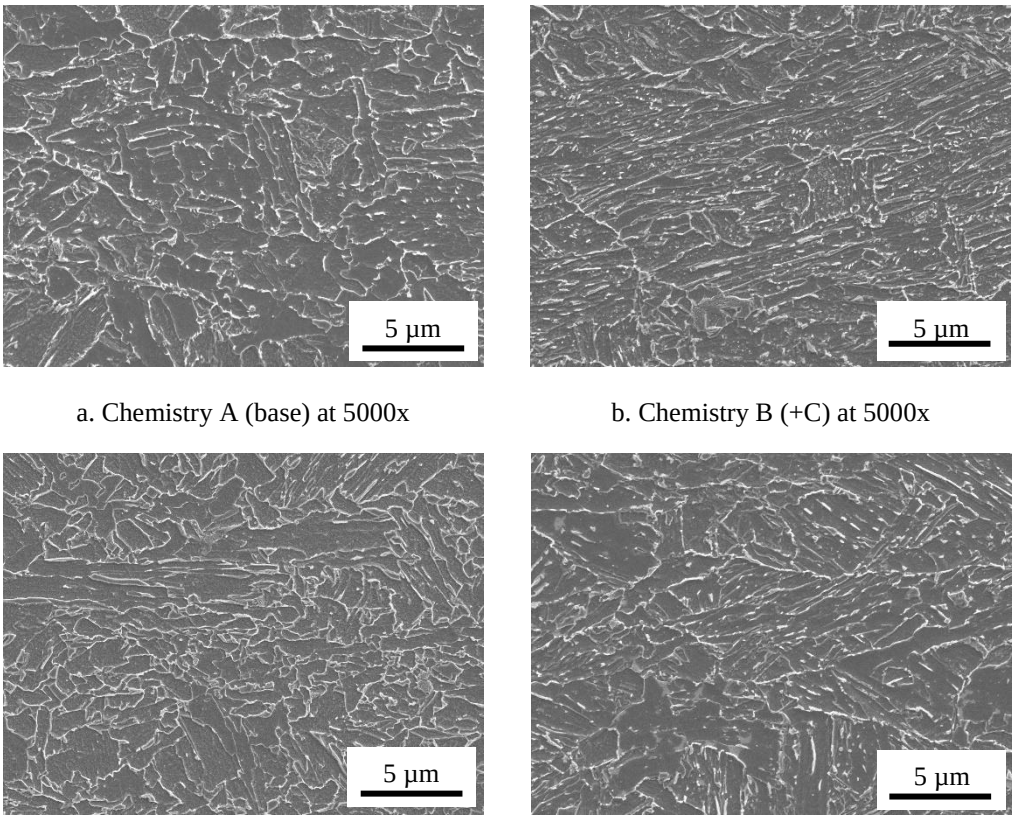

a. Chemistry A (base) at 5000x

b. Chemistry B (+C) at 5000x

c. Chemistry C (+Nb) at 5000x

d. Chemistry D (+V) at 5000x

Figure 4.28. SEM images of all chemistries processed at 950-630-490

These samples showed the best combination of both strength and stretch flangeability and for this reason they were analyzed extensively using EBSD, TEM and APT. SEM imaging does not show significant microstructural differences between the four chemistries but further analysis using these methods helps to explain the difference in properties and the significant improvement in the strength of the vanadium containing sample.

EBSD maps from chemistries B and D and are shown in Figure 4.29. The bainitic lath structure is evident from the band contrast images. Chemistry B contains more

regions of poor band contrast than in chemistry D (Figure 29 a.) Chemistry D has a finer microstructure than chemistry B with many high angle grain boundaries as seen in the grain boundary maps in Figure 4.29 b. The grain size was measured using the linear intercept method with a 5° misorientation angle and using the formula by Hell at al [32] the bainite lath width was determined to be 0.36 µm and 0.32 µm for chemistries B and D respectively. The lath width measured using EBSD analysis was confirmed using TEM analysis for chemistry D which measured an average lath width of 0.33 µm. TEM analysis is discussed in the following pages.

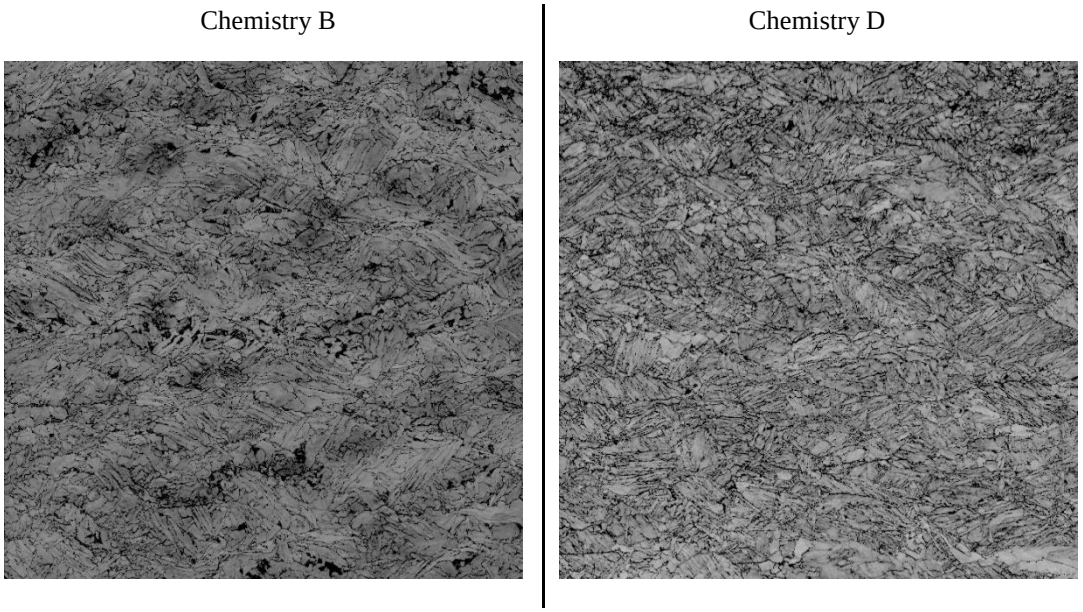

a. Band contrast maps at 700x magnification

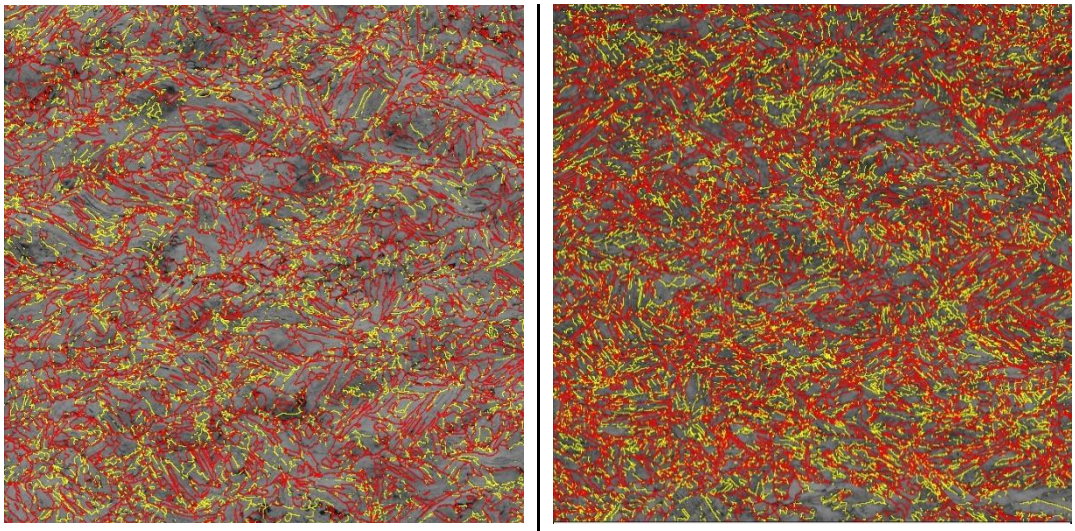

b. Grain boundary maps with HAGB (≥15°) shown in red and LAGB in yellow

Figure 4.29. EBSD maps of chemistries B and D processed at 950-630-490

Extraction replicas were taken from chemistries B and D to analyze the particles present in the steel. Low magnification images provide an overview of the sample. Both samples show large precipitates present in the overall microstructure (Figure 4.30 a.). High magnification images were taken of the particles. Figure 4.30 b. shows examples of the large square shaped particles present in both samples. Both samples contain randomly distributed particles of square or quasi-square shape and some rectangular particles. Examples of small round particles are displayed in Figure 4.30 c. Fewer fine particles are present in either sample compared to the coarse particles. The fine particles observed in chemistry D were frequently found attached to the square or quasi-square shaped particles as shown, demonstrating that the large square precipitates act as nucleation points for the smaller particles.

Chemistry B

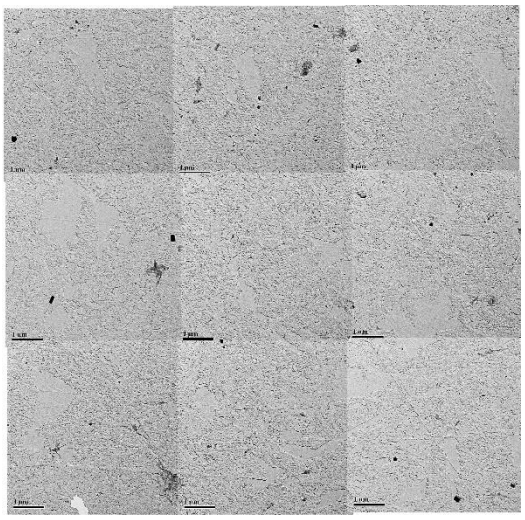

Chemistry D

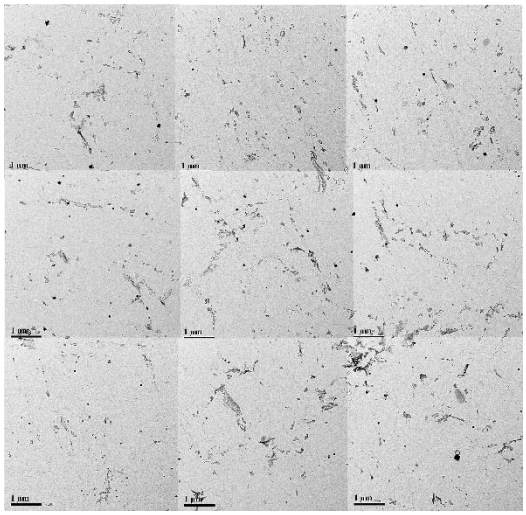

a. Low magnification of both coarse and fine preciptiates

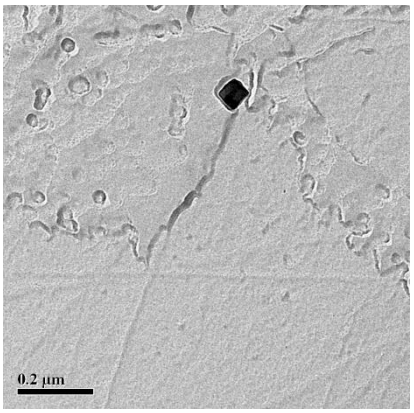

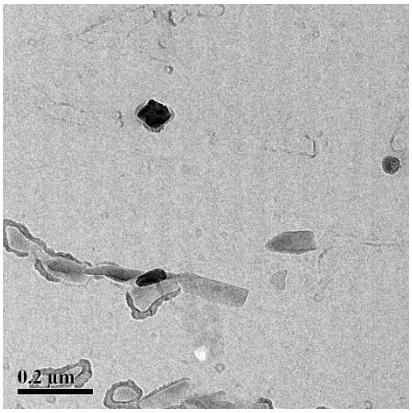

b. Coarse square or quasi-square shaped particles

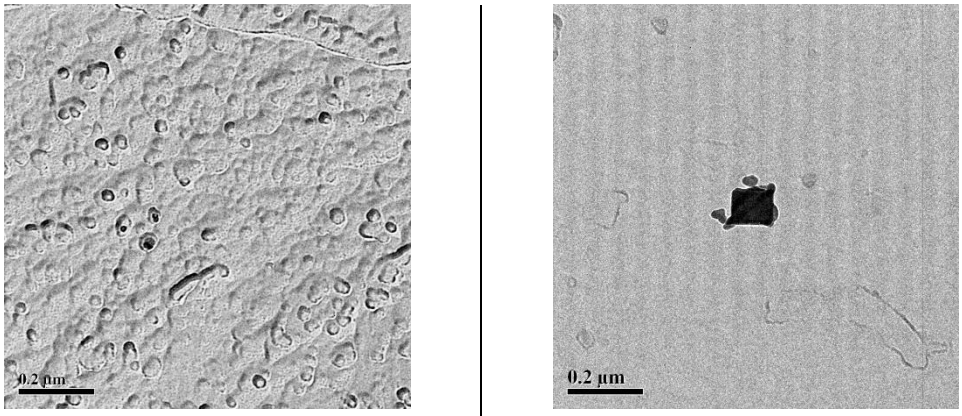

c. Fine round shaped particles which in chemistry D are seen attached to a large square particle

Figure 4.30. TEM extraction replicas of chemistries B and D processed at 950-630-490

To produce a particle size distribution (Figure 4.31), the particles from 100 areas and 139 areas were measured in chemistries B and D respectively. The two chemistries are compared in Table 4.4, showing that the average particle size is larger for chemistry D which contains vanadium. The average particle number density and total area fraction are also higher in chemistry D.

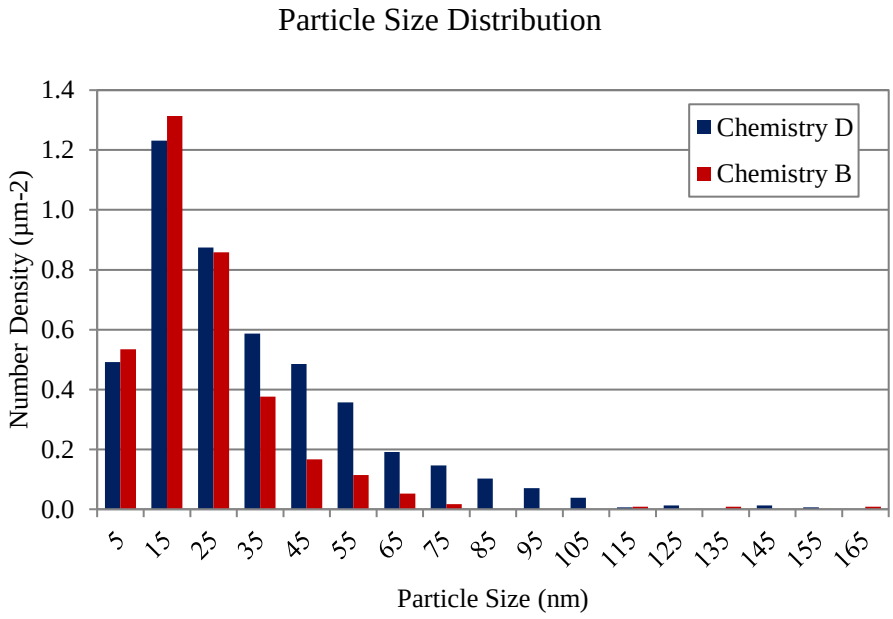

Figure 4.31. Particle size distribution from chemistries B and D processed at 950-630-490

Table 4.4. Summary of TEM particle analysis using extraction replica method

Chem	Length range (nm)	Average length (nm)	Average particle area (nm^2)	Number density (μm^{-2})	Area fraction (10^{-3})
B	3-168	23 ± 17	529	3.46	1.8
D	2-284	33 ± 26	1089	4.62	5

The compositions of the particles were determined using EDS analysis (Figures 4.32 to 4.35). Both samples contain silicon particles which are a remnant from polishing with silicon carbide. The copper peak is from the replica support grid holder and the carbon peak is partially due to the carbon film of the replicas. The large square or quasi-square particles in both samples have a high titanium peak followed by niobium and vanadium. In contrast, the small round or elongated particles have a higher niobium peak

than titanium peak. A vanadium peak is also present for both coarse and fine particles in chemistry D but is the smallest peak of the three microalloying elements, titanium, niobium and vanadium. Both samples contain irregularly shaped particles which are iron, chromium and manganese rich.

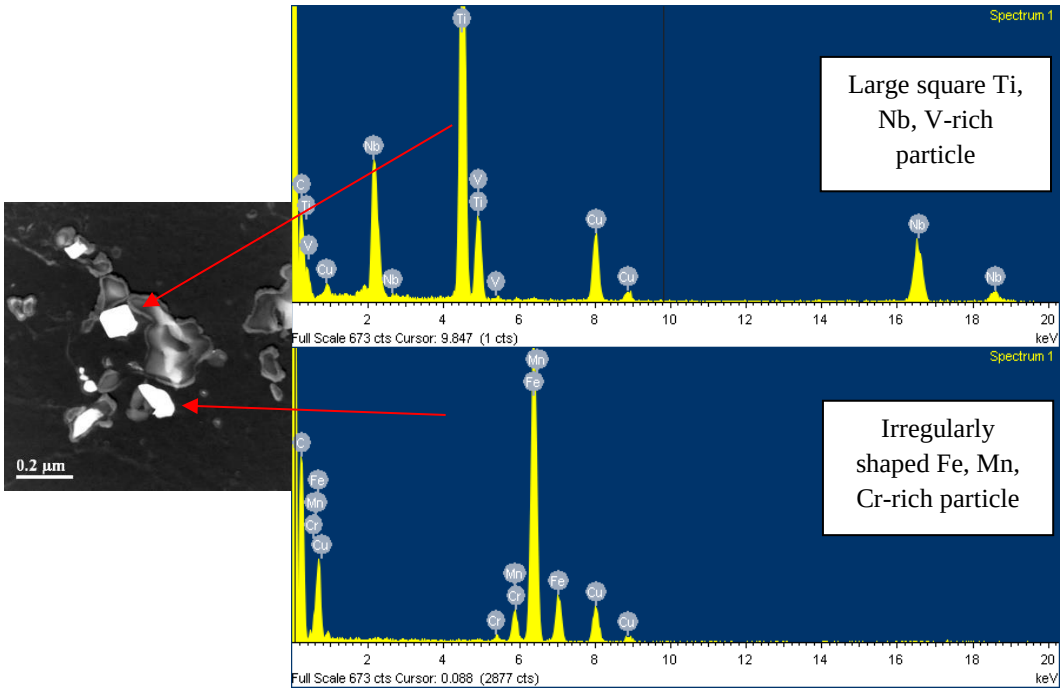

Figure 4.32. Precipitates from chemistry D showing two types of particles

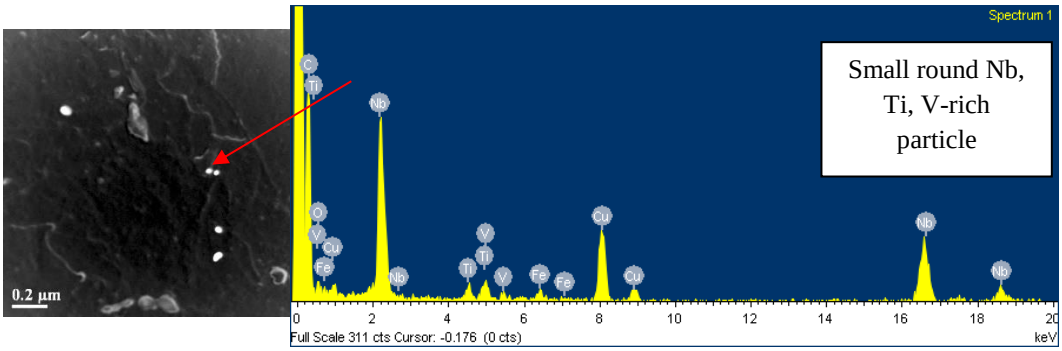

Figure 4.33. Small round precipitates from chemistry D with high Nb peaks

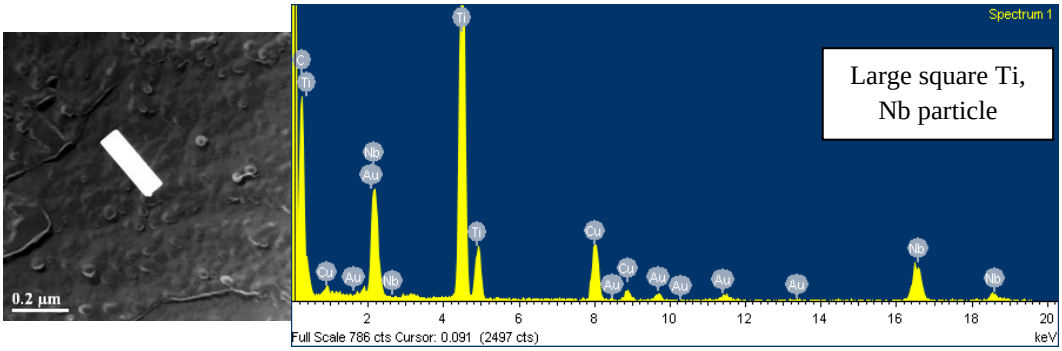

Figure 4.34. Large square Ti-rich particle in chemistry B

In chemistry D, round particles are sometimes attached to larger square shaped particles (Figure 4.35). This is likely evidence that the large titanium nitrides which form earlier in the hot rolling process act as nucleation for Nb precipitation later in the hot rolling process.

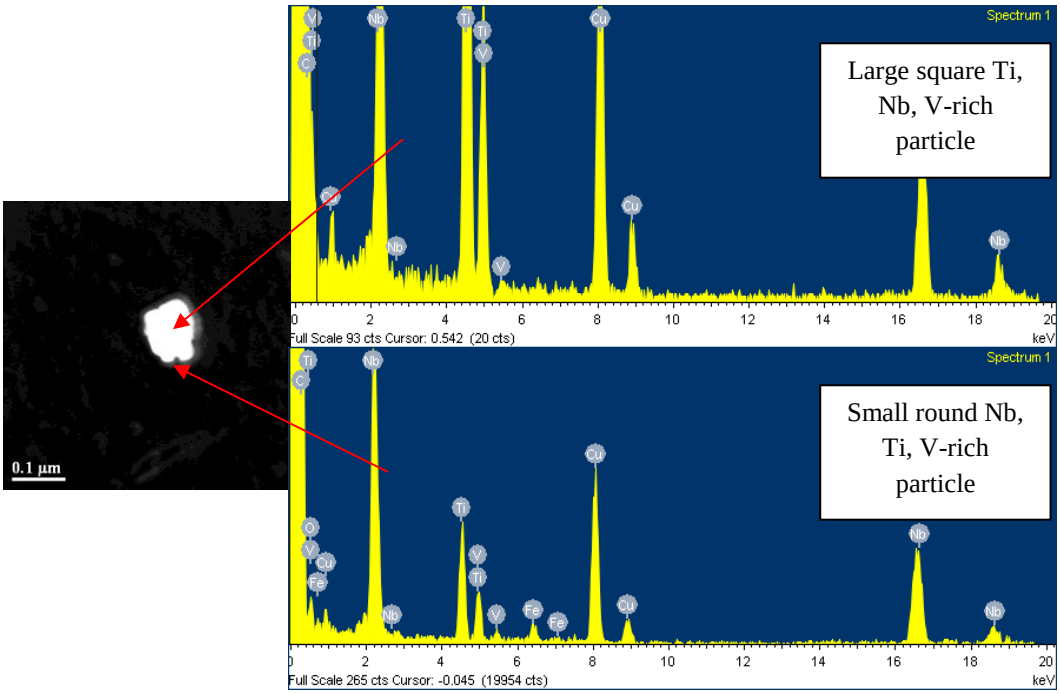

Figure 4.35. Particles from chemistry D showing Ti rich center with small round Nb-rich particles attached

Thin foil TEM analysis was performed on chemistries C and D to obtain more details on the bainite morphology. Chemistry C is shown in Figure 4.36 and chemistry D in Figure 4.37. Both samples have similar microstructures of lath and irregularly shaped bainite with high dislocation density. Thin retained austenite (RA) films between bainite laths also exist in both samples. Chemistry C appears to have more parallel lath shaped bainite than chemistry D. The irregular shaped bainite found in chemistry D is likely found nearer the surface of the sample rather than center. Chemistry C contains a small fraction of plate-like or block-shaped auto-tempered martensite between bainite laths which is not seen in chemistry D. The martensite regions contain precipitates of multiple cementite variants. Carbides are also found at the bainite lath boundaries in chemistry C.

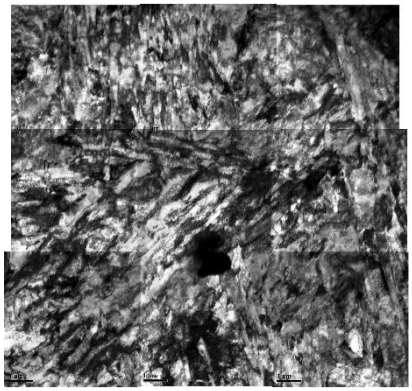

a. Overview of bainitic microstructure with high dislocation density

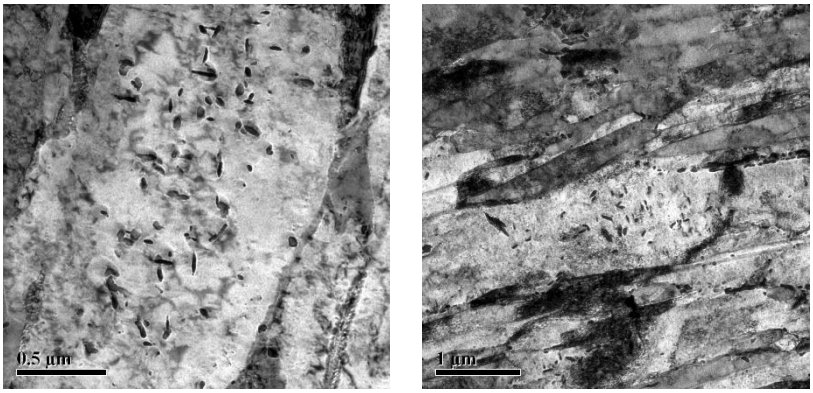

b. Cementite present within martensite regions

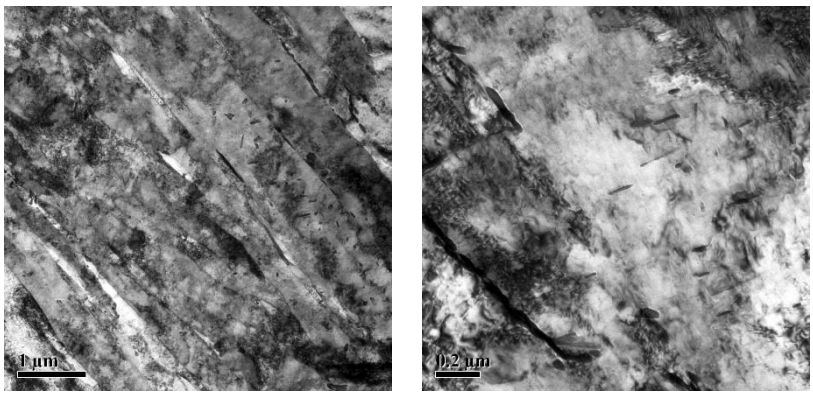

c. Carbides present at lath boundaries

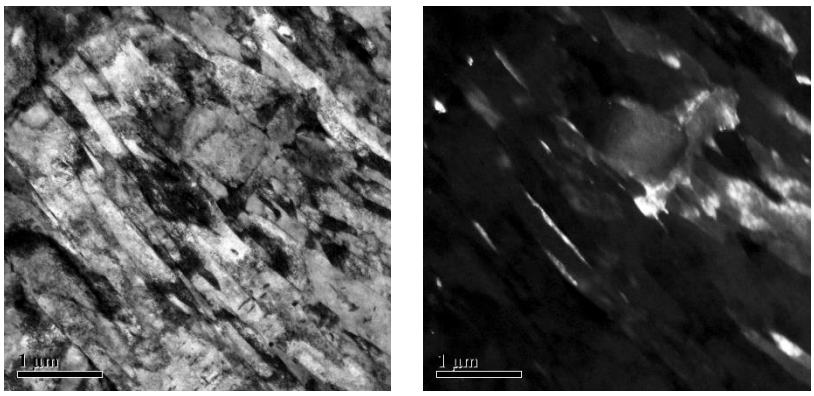

d. Retained austenite between bainite laths

Figure 4.36. TEM thin foil analysis of chemistry C processed at 950-630-490

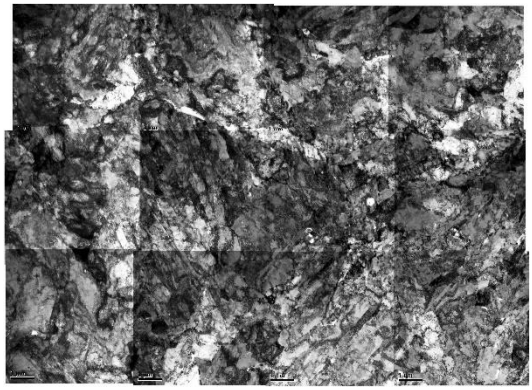

a. Overview of bainitic microstructure with high dislocation density

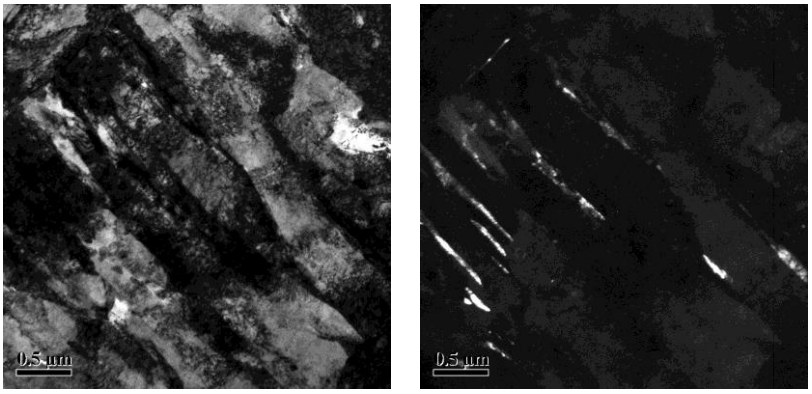

b. Retained austenite between bainite laths

Figure 4.37. TEM thin foil analysis of chemistry D processed at 950-630-490

Images of precipitates are shown in Figure 4.38. Chemistry C contains both coarse square shaped precipitates and fine precipitates (Figure 4.38 a.). A few fine precipitates are found in chemistry D within the bainite lath (Figure 4.38 b.)

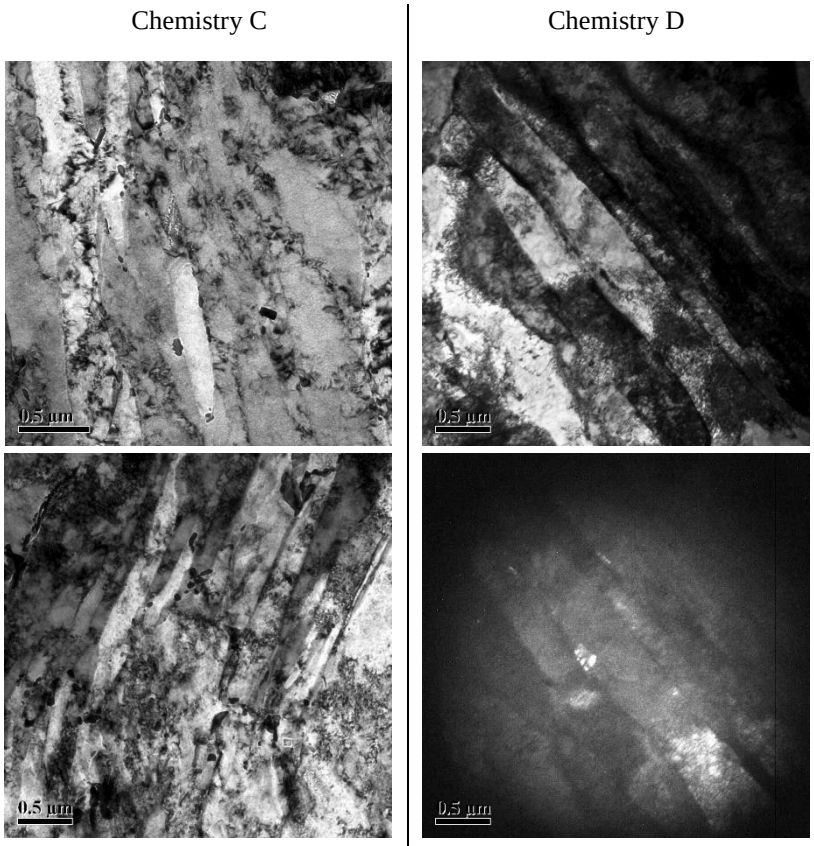

a. Coarse and fine precipitates

b. Fine precipitates within bainite laths (bright and dark field images)

Figure 4.38. Precipitates in chemistries C and D processed at 950-630-490 using TEM thin foil analysis

The bainite lath width was measured along a line perpendicular to the lath as shown in Figure 4.39. The lath width in chemistry C was measured in 18 fields with 287 measurements and in 22 fields with 252 measurements in chemistry D producing the distribution in Figure 4.40. The average lath width in chemistry D is 333 nm +/- 203 nm while the average lath width in chemistry C is 300 +/- 180 nm demonstrating that there is no significant difference in lath width between the two samples.

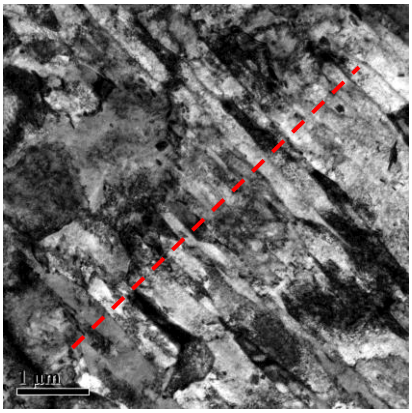

Figure 4.39. Method of measuring bainite lath width. (Example taken from chemistry C.)

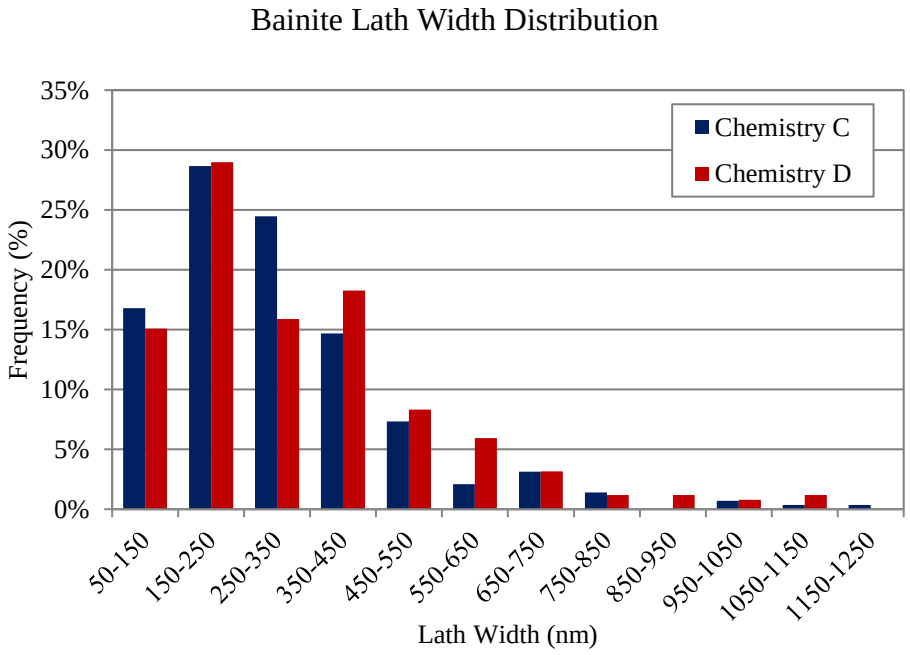

Figure 4.40. Bainite lath width distribution in chemistries C and D processed at 950-630-490

APT analysis was also performed on chemistries B, C and D to complement the TEM analysis. Two datasets were produced for chemistry B and are displayed in Figure 4.41. The first dataset shows a fairly uniform distribution of all elements. The second

dataset contains some large regions of carbon segregation, but they do not coincide with segregation of microalloying elements.

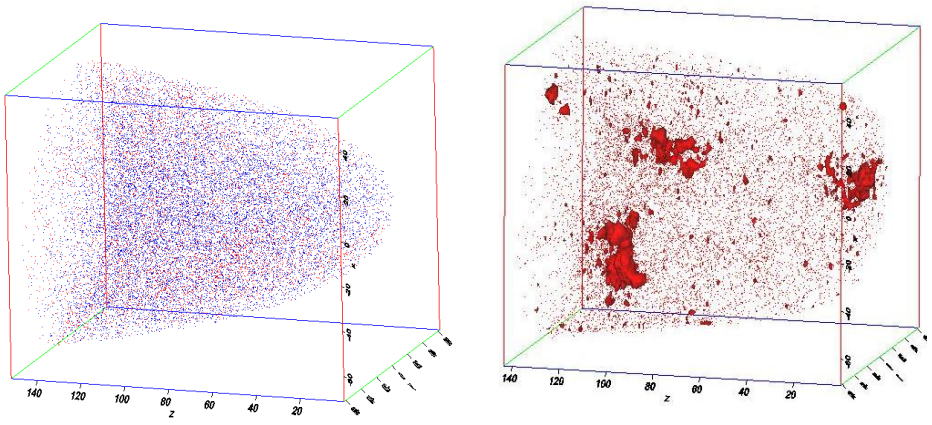

a. Dataset 1 showing dot map of Fe (blue) and C (red) density

b. Dataset 2 showing C density with 1 at% C isosurfaces

Figure 4.41. Atom probe datasets 1 and 2 from chemistry B processed at 950-630-490

One atom probe dataset was produced for chemistry C. The carbon isosurfaces in Figure 4.42 show regions of carbon segregation which is focussed especially at the end of the tip. The ROI shown in Figure 4.42 b. was used to determine the matrix composition of the sample shown in Table 4.5, excluding the region with higher carbon concentration.

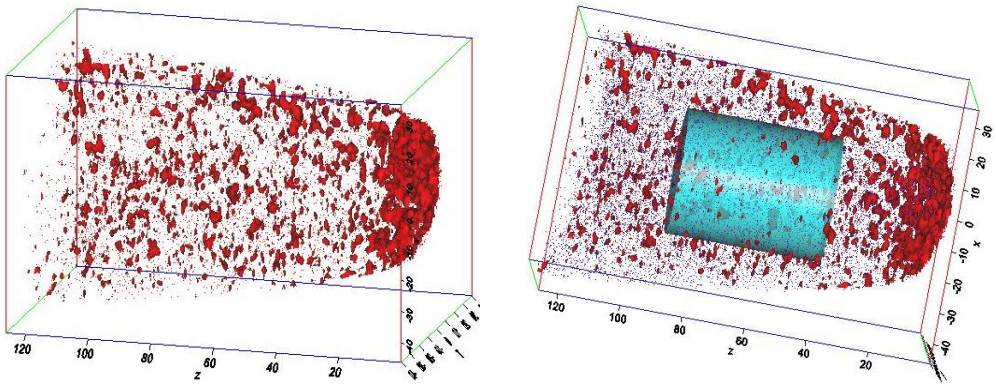

a. C density with 1 at % C isosurfaces b. ROI used to determine matrix composition

Figure 4.42. Atom probe datasets from chemistry C processed at 950-630-490

Table 4.5. Concentration of elements in atom probe dataset from chemistry C processed at 950-630-490

Element	ROI
Fe	96.6%
Mn	2.0%
Cr	0.3%
C	0.1%
Mo	0.1%
Nb	0.02%

Three datasets were produced for chemistry D. The first dataset (Figure 4.43) contains two regions of particularly high carbon concentration. Given the morphology of this sample these regions are likely bainite lath boundaries. Vanadium isosurfaces are shown in Figure 4.43 b. and are also located along the boundaries identified by the carbon isosurfaces. Niobium isosurfaces for this dataset are not displayed because niobium appeared to segregate along a crystallographic pole which is an artefact of the APT reconstruction.

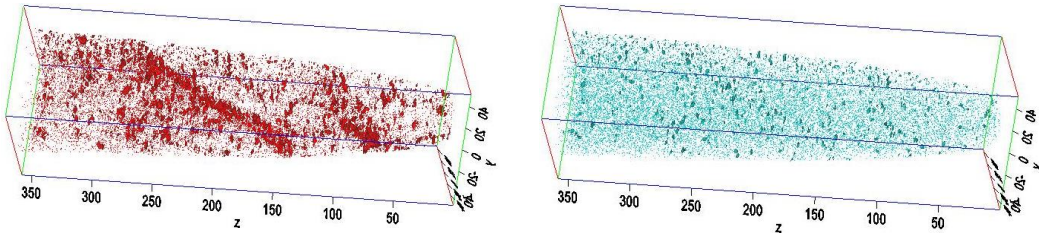

a. C density with 1 at% C isosurfaces b. V density with 1 at% V isosurfaces

Figure 4.43. Atom probe dataset 1 from chemistry D processed at 950-630-490

The second dataset (Figure 4.44) also contains regions of carbon segregation. It is evident that niobium and vanadium segregation appear in similar regions, providing evidence of co-segregation. Additional images are available in Appendix B.

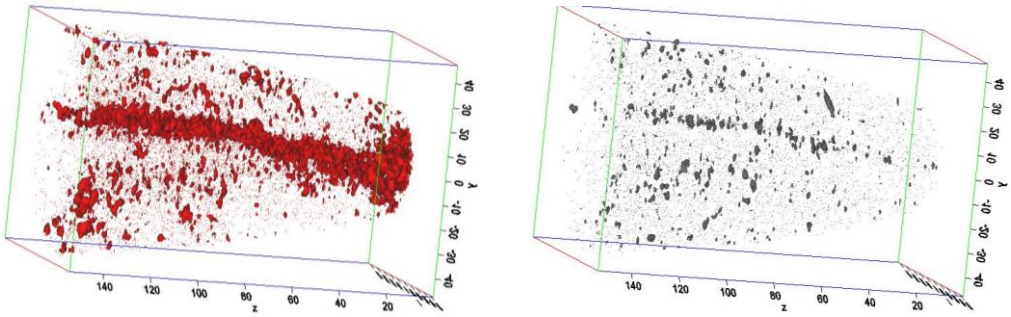

a. C density with 1 at% C isosurfaces b. Nb density with 0.4 at% Nb isosurfaces

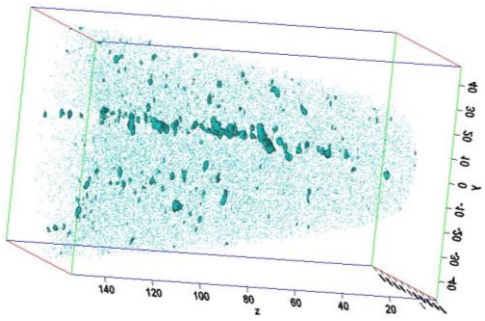

c. V density with 1 at% V isosurfaces

Figure 4.44. Atom probe dataset 2 from chemistry D processed at 950-630-490

The third dataset was within a high carbon region and did not provide any additional information of interest. The composition of the three datasets are shown in Table 4.6 and the difference in carbon concentration in dataset 3 shows that this was likely from within a martensite or retained austenite region. The composition of datasets 1 and 2 are taken from the matrix, avoiding the carbon rich regions.

Table 4.6. Concentration of elements in APT datasets 1-3 from chemistry D processed at 950-630-490

Element	Dataset 1	Dataset 2	Dataset 3
Fe	96.5%	96.2%	93.8%
C	0.1%	0.2%	2.7%
Mn	1.9%	1.9%	2.0%
Cr	0.4%	0.3%	0.3%
Mo	0.1%	0.1%	0.1%
Nb	0.02%	0.03%	0.02%
V	0.2%	0.2%	0.0%

4.3 Dilatometry

Dilatometry analysis was performed to simulate TMP and determine the effects of processing and chemistry on the phase transformations. The effects of CT (630 °C and 490 °C), deformation at the FT, intermediate cooling and the vanadium content are investigated here.

The following two chemistries shown in Table 4.7 were investigated. The vanadium content is 0 % in chemistry 1 and 0.1% in chemistry 2. Chemistries 1 and 2 are similar to chemistries C and D of the hot rolled trial material. The main differences are the manganese content which is 0.2 wt% less in the dilatometry samples and the

vanadium content of chemistry 2 which is 0.1 wt% while the vanadium content of chemistry D is 0.2 wt%.

Table 4.7. Dilatometry trial chemistries given in wt%

Chemistry	C	Mn	Si	Nb	Al	Ti	Mo	N	Cr	V
1	0.08	1.7	0.55	0.05	0.035	0.02	0.2	0.005	0.3	0
2										0.1

Seven dilatometry tests were conducted for each chemistry. The following section shows the cooling routine conducted during the test along with the resulting cooling curve. Optical microscopy was performed to relate the cooling curves to the final microstructure.

All tests involved heating the specimen to 1050 °C at 10 °C/s, holding it there for 5 seconds and applying 15% deformation at that temperature to simulate roughing rolling. Tests 1 to 3 (Figure 4.45) were subsequently cooled to 950 °C at a rate of 20 °C/s. The samples were held at 950 °C for 10 s and at the end of the isothermal holding, test 1 was direct quenched to room temperature from 950 °C. Test 2 was cooled at 75 °C/s to 630 °C and held there for 300 s. To study the effect of a change in CT, test 3 was cooled at 110 °C/s to 490 °C and held there for 300 s. The cooling rates were selected based on the cooling rates applied during the hot rolling trials. After the final isothermal holding step, all samples were direct quenched to room temperature.

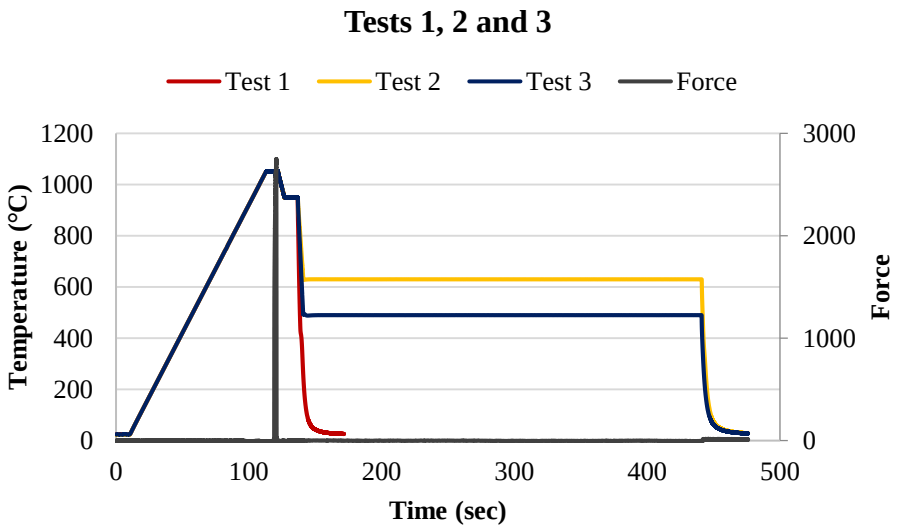

Figure 4.45. Dilatometry tests 1 to 3

Tests 4 through 7 were cooled to 890 °C instead of 950 °C. The samples were held at 890 °C for 10 s and at the end of the isothermal holding, 30% deformation was applied to simulate finishing rolling. Tests 4 and 5 (Figure 4.46) replicate tests 2 and 3 respectively but with the second deformation step to determine the effect of finishing rolling on the final microstructure.

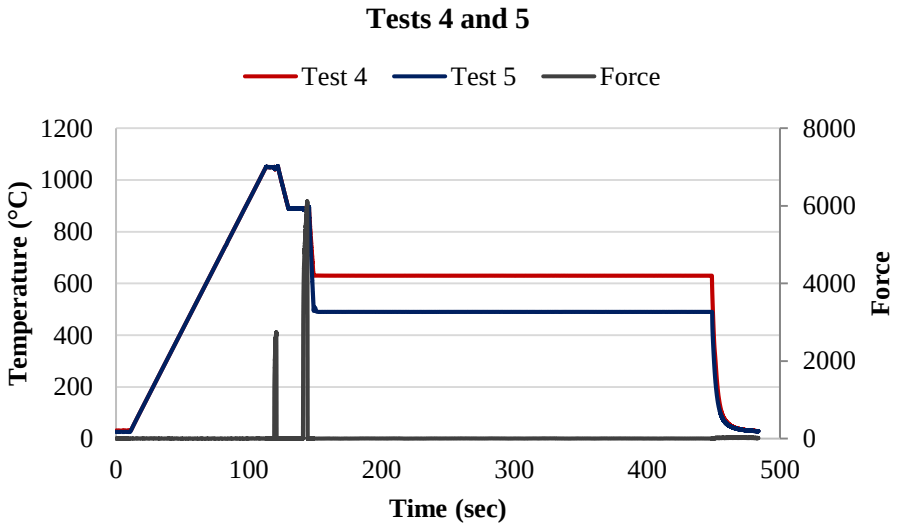

Figure 4.46. Dilatometry tests 4 and 5

Test 6 was similar to test 4 but was held at 630 °C for only 5 seconds and then quenched to room temperature. This test was performed to study the effect of the short intermediate cooling step which produced favourable mechanical properties. Test 6 can be compared to test 7 which after a 5 second isothermal hold at 630 °C, was cooled to 490 °C at 45 °C/s and held there for 300 s before quenching to room temperature. Test 7 replicates the processing parameters which produced the best mechanical properties (950-630-490). Tests 6 and 7 are seen in Figure 4.47.

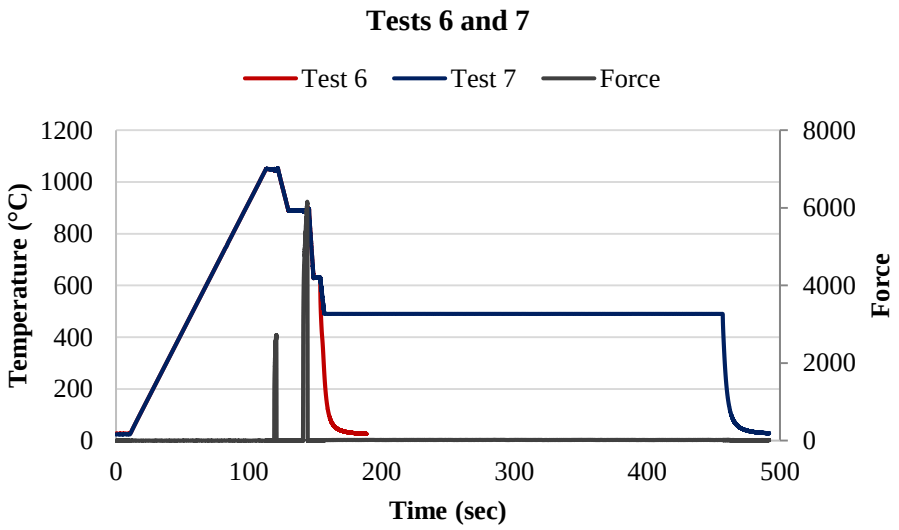

Figure 4.47. Dilatometry tests 6 and 7

The transformations are measured as the percentage length change relative to the total change in length during cooling. An example taken from test 2 is shown in Figure 4.48 to demonstrate how the percent relative change in length was determined from the cooling curves. The transformation start and finish temperatures during cooling to room temperature were found by determining the temperature at which the cooling curve deviates from the extrapolated slopes seen in Figure 4.48. The percent relative change in length and the transformation temperatures are presented in Tables 4.8 and 4.9 respectively.

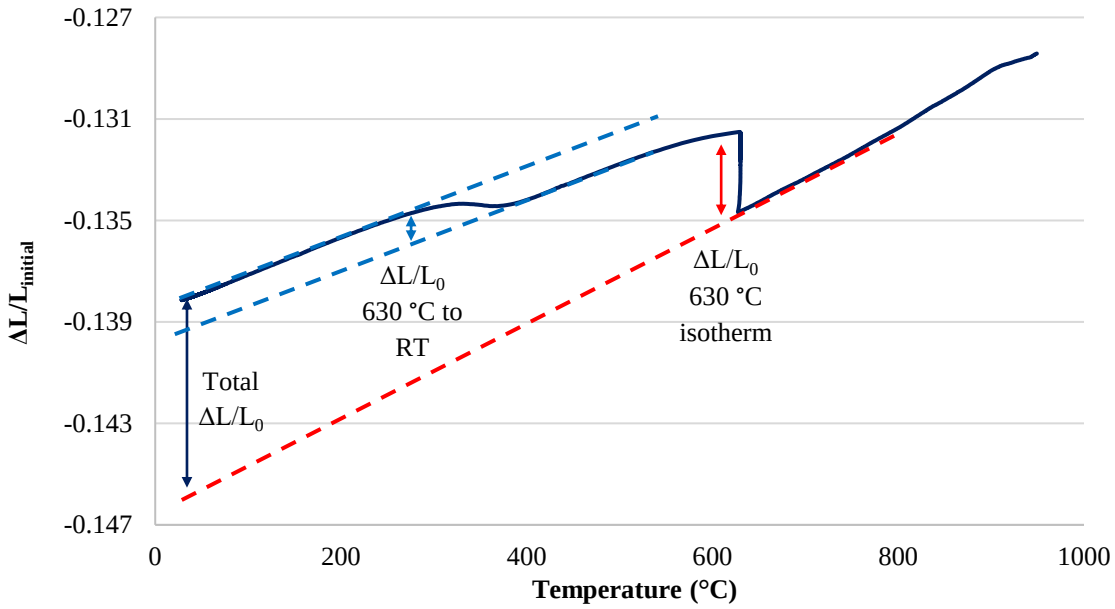

Figure 4.48. Example from Test 2 demonstrating how transformations were quantified from cooling curves

Table 4.8. Dilatometry data showing percent relative change in length of the total change in length during cooling. The column headers, 1 and 2, identify the chemistry.

Test No	Test ID	630 Isotherm 1	630 Isotherm 2	630 to RT 1	630 to RT 2	490 Isotherm 1	490 Isotherm 2
1	a			76.7%	77.8%		
	b			78.4%	77.0%		
2	a	37.3%	28.5%	16.1%	27.7%		
	b	37.9%	26.7%	17.1%	28.3%		
3	a					60.3%	62.5%
	b					60.8%	62.4%
4	a	42.0%	35.2%	17.0%	23.4%		
	b	41.4%	34.3%	18.6%	23.0%		
5	a					56.4%	64.6%
	b					53.7%	64.3%
6	a	12.7%	7.1%	15.3%	34.1%		
	b	17.2%	6.1%	19.6%	36.8%		
7	a	16.2%	6.2%			11.0%	27.4%
	b	15.5%	7.7%			12.9%	21.3%

Table 4.9. Dilatometry data showing transformation start and finish temperatures during cooling from 630 °C to RT. The column headers, 1 and 2, identify the chemistry.

Test No	Test ID	630 to RT			
		T_{start}	T_{finish}	T_{start}	T_{finish}
		1		2	
1	a	515	295	531	302
	b	545	300	540	313
2	a	387	243	442	251
	b	381	246	434	273
3	a				
	b				
4	a	373	247	396	253
	b	371	246	406	254
5	a				
	b				
6	a	428	279	473	279
	b	460	278	463	284
7	a				
	b				

The cooling curves from test 1 (Figure 4.49) show nearly identical curves for both chemistries with no difference in the amount of transformation or transformation temperatures between the two chemistries. Taking an average of the four transformations, approximately 78% of the total length change during cooling is due to the transformation occurring around 400 °C. The microstructure is martensitic as shown in Figure 4.50.

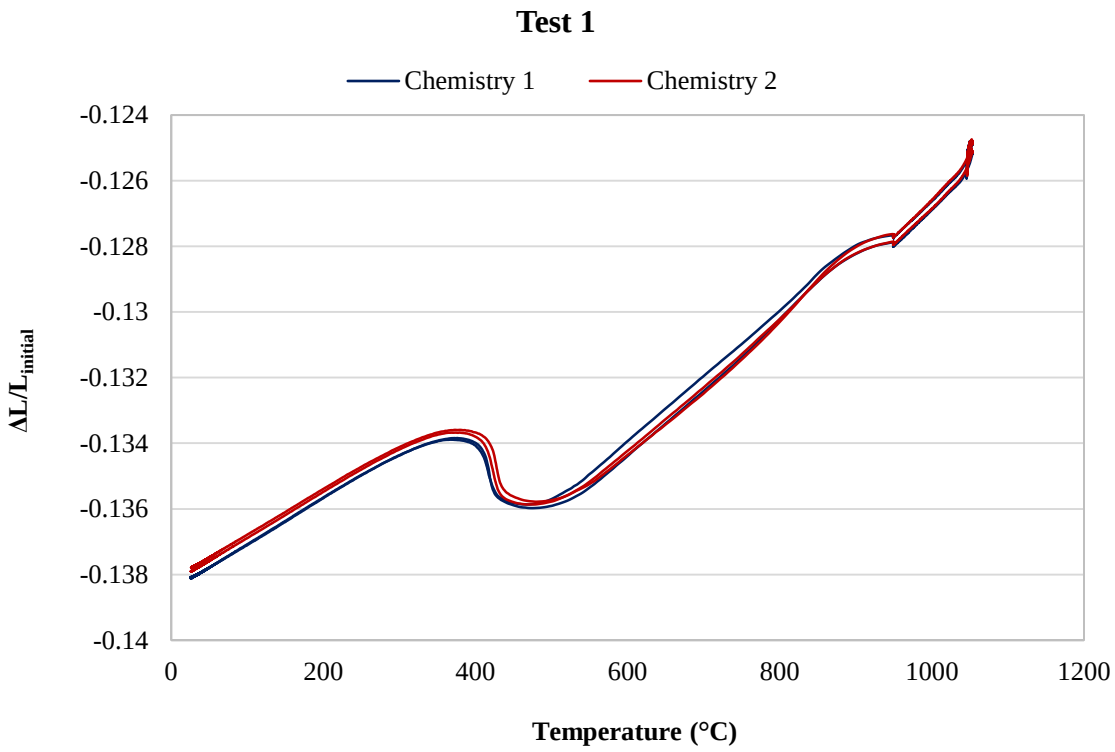

Figure 4.49. Cooling curves from test 1

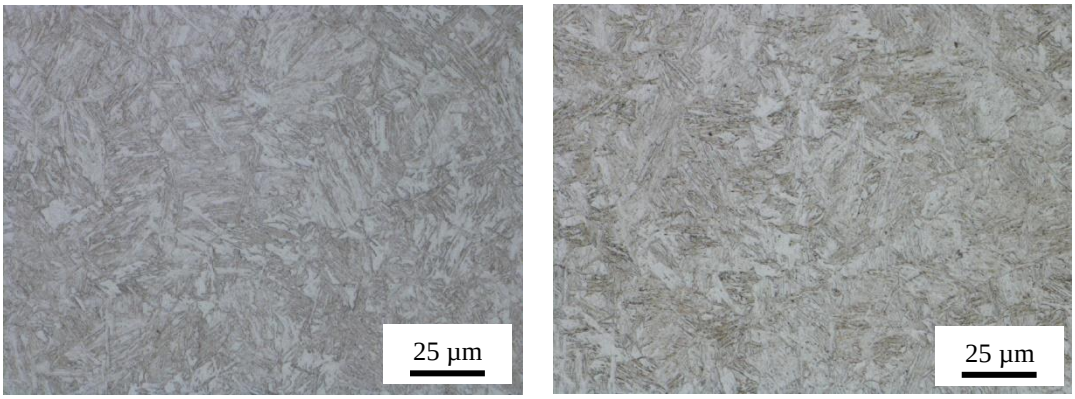

a. Chemistry 1, test 1, 500x magnification

b. Chemistry 2, test 1, 500x magnification

Figure 4.50. Optical microscopy of final microstructure from test 1

The cooling curves from tests 2 and 4 are shown in Figure 4.51. Chemistry 1 is shown in the blue curves and chemistry 2 in the red curves which contains vanadium. The transformation during isothermal holding at 630 °C is larger for chemistry 1 than for chemistry 2 in both tests 2 and 4. When deformation is applied (test 4), this transformation is also larger.

The second major transformation occurs during cooling to room temperature and is larger in the vanadium containing chemistry. Deformation has little impact on chemistry 1 during cooling to room temperature but when deformation is applied to the vanadium containing sample, the transformation is smaller than in the sample without vanadium. The second transformation starts at higher temperatures in the vanadium containing chemistry for both tests 2 and 4. The microstructures produced are a combination of ferrite and martensite (Figure 4.52).

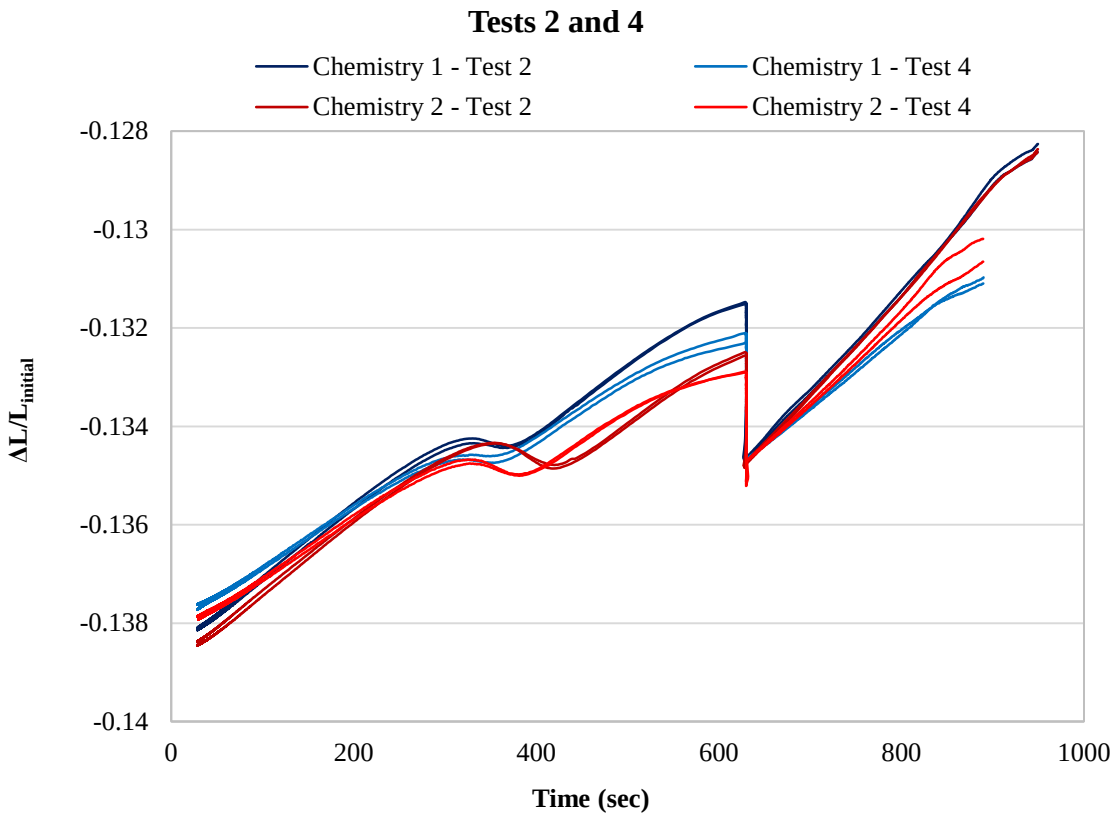

Figure 4.51. Cooling curves from tests 2 and 4

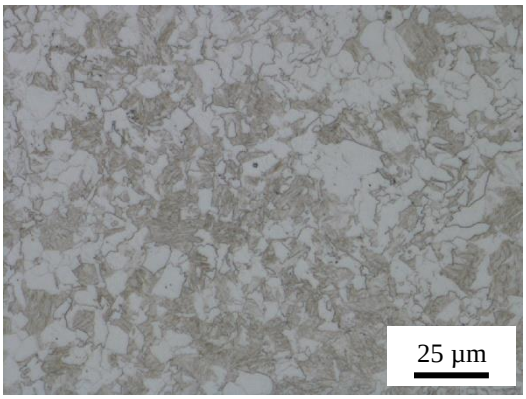

a. Chemistry 1, test 2, 500x magnification

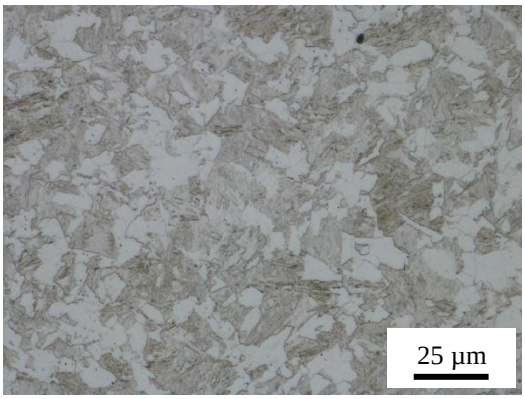

b. Chemistry 2, test 2, 500x magnification

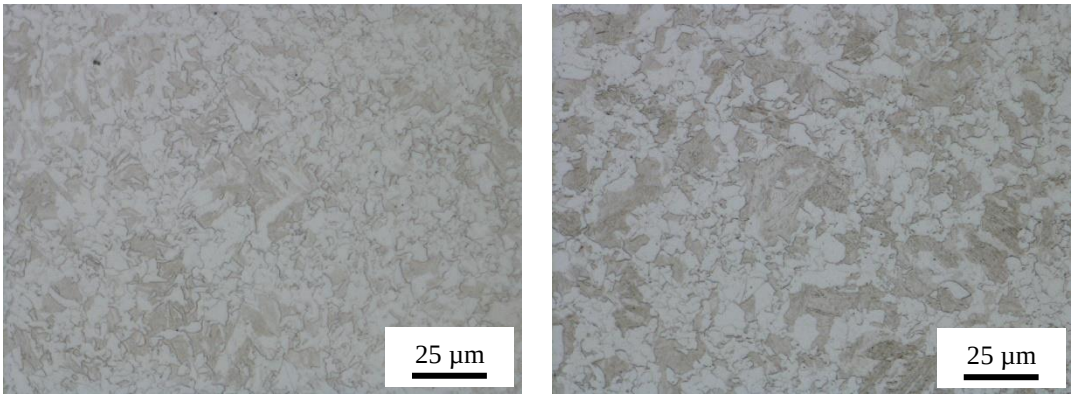

c. Chemistry 1, test 4, 500x magnification b. Chemistry 2, test 4, 500x magnification

Figure 4.52. Optical microscopy of final microstructure from tests 2 and 4

The transformations occurring during isothermal holding at 490 °C in tests 3 and 5 are shown in Figure 4.53. In test 3, the transformation in chemistry 2 is slightly larger than in chemistry 1. In test 5 which includes a second deformation step, the difference between the two chemistries is larger. Figure 4.54 shows a bainitic microstructure present in the samples.

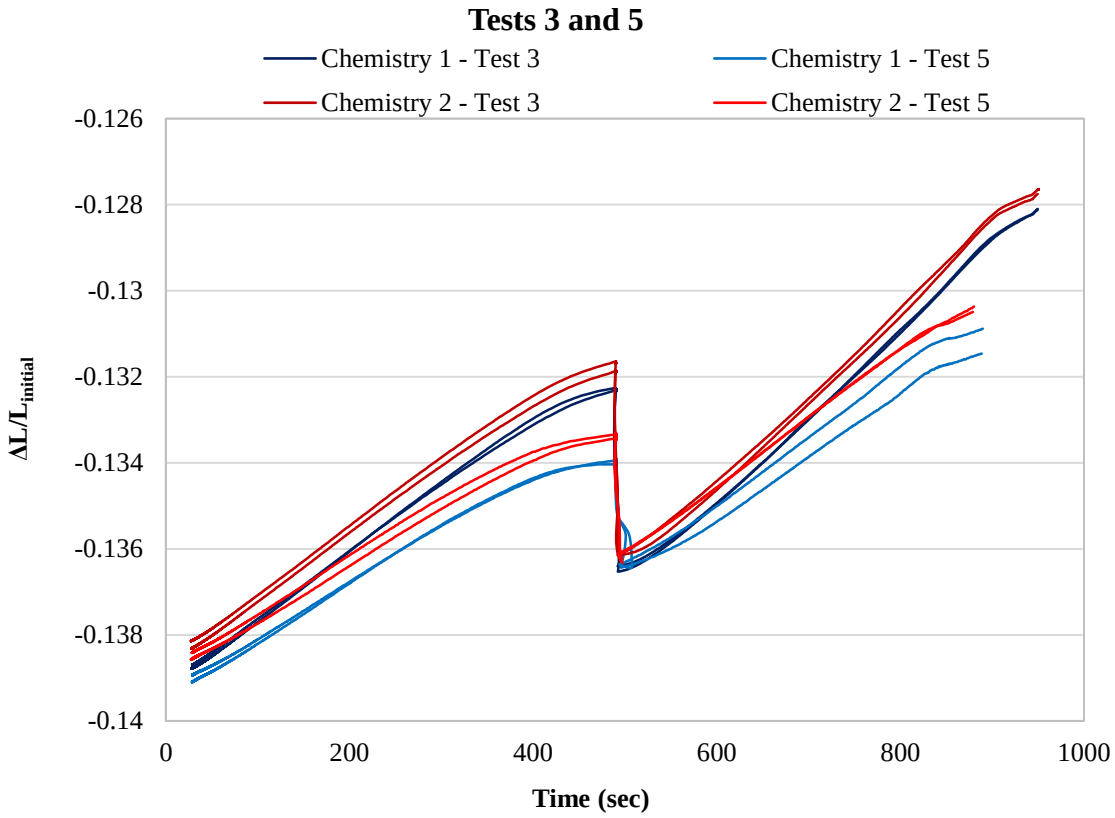

Figure 4.53. Cooling curves from tests 3 and 5

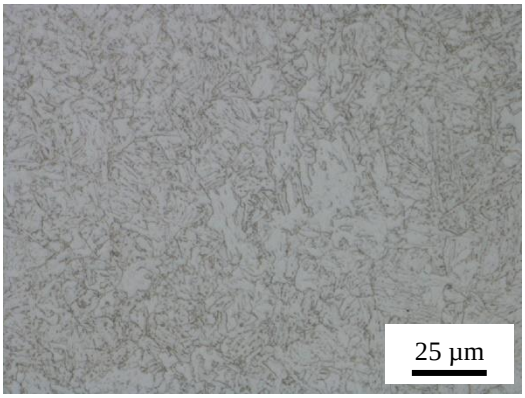

a. Chemistry 1, test 3, 500x magnification

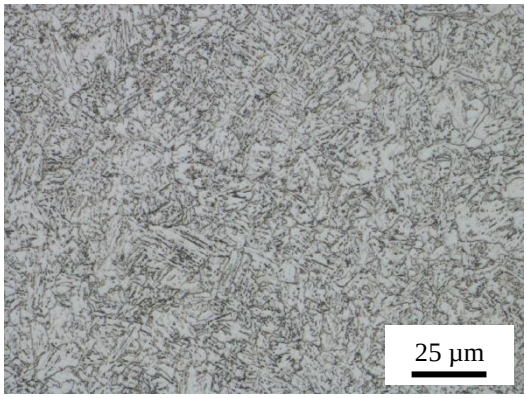

b. Chemistry 2, test 3, 500x magnification

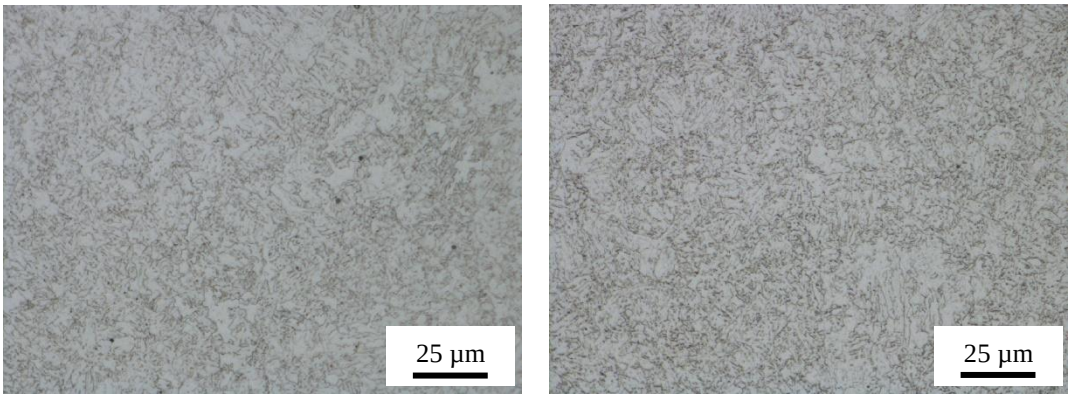

c. Chemistry 1, test 5, 500x magnification b. Chemistry 2, test 5, 500x magnification

Figure 4.54. Optical microscopy of final microstructure from tests 3 and 5

The cooling curves from test 6 are shown in Figure 4.55 and contain two transformations. The first transformation occurring during isothermal holding at 630 °C is smaller in chemistry 2 while the second transformation during cooling to room temperature is larger for chemistry 2 and starts at slightly higher temperatures. This test allows very little time for a transformation to occur at 630 °C and the consequences of this can be seen in the microstructures in Figure 4.56. While both microstructures consist of ferrite and martensite, chemistry 1 contains a higher fraction of ferrite. This corresponds to the results shown in Table 4.8 which show a larger deformation in chemistry 1 at 630 °C corresponding to the austenite to ferrite transformation and a smaller deformation while quenching to room temperature which produces martensite.

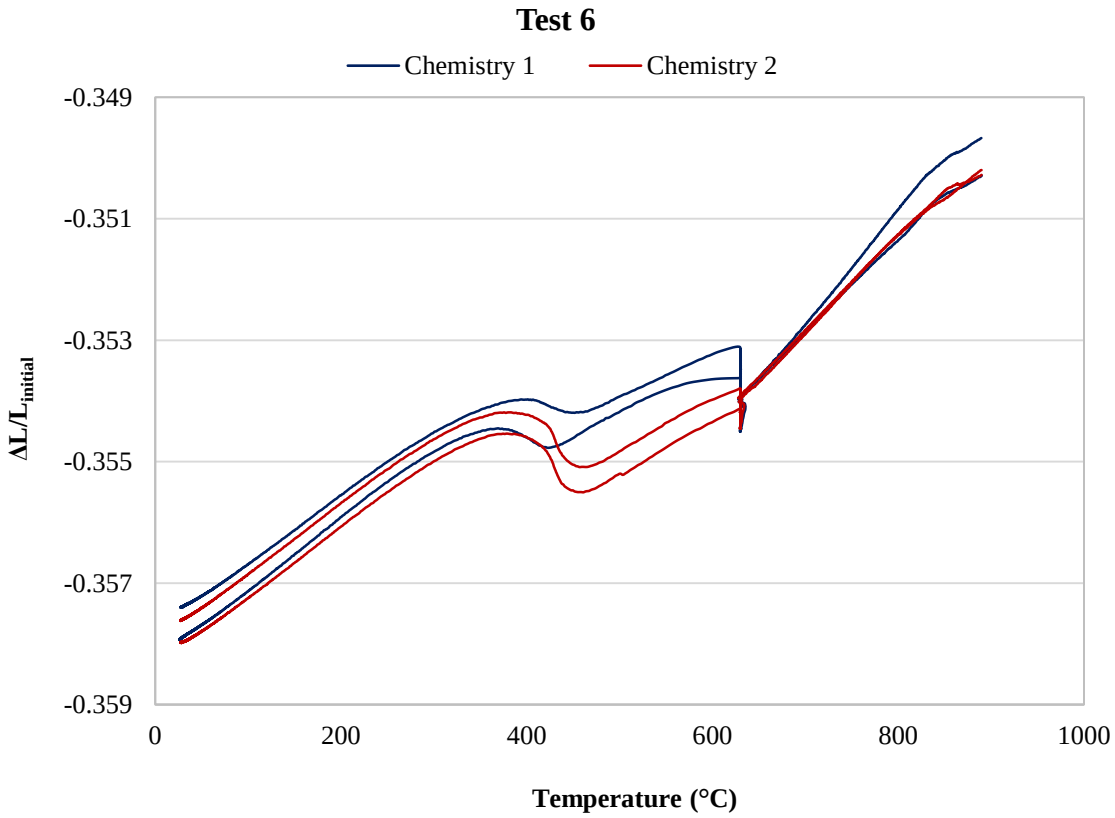

Figure 4.55. Cooling curves from test 6

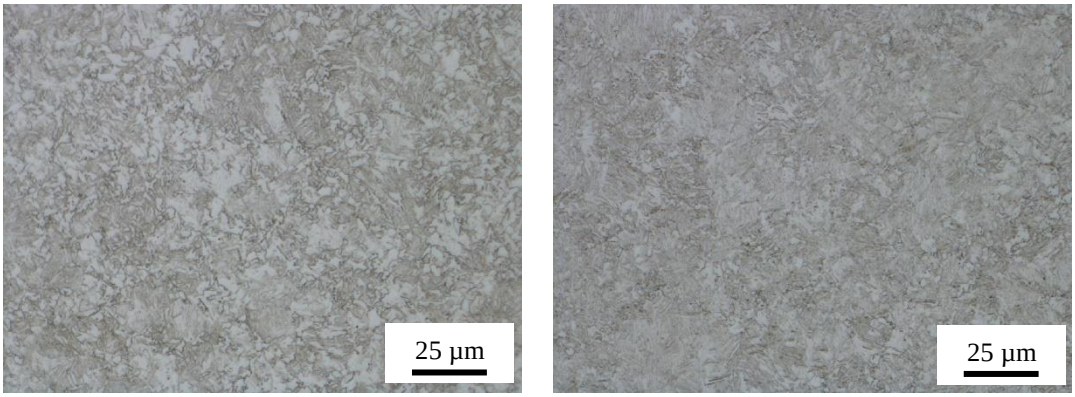

a. Chemistry 1, test 6, 500x magnification

b. Chemistry 2, test 6, 500x magnification

Figure 4.56. Optical microscopy of final microstructure from test 6

The cooling curves for test 7 are shown in Figure 4.57. The transformation during isothermal holding at 630 °C is smaller in the vanadium containing chemistry while the transformation at 490 °C is larger for chemistry 2. The microstructure in Figure 4.58 is similar for both chemistries and appears to be granular bainite.

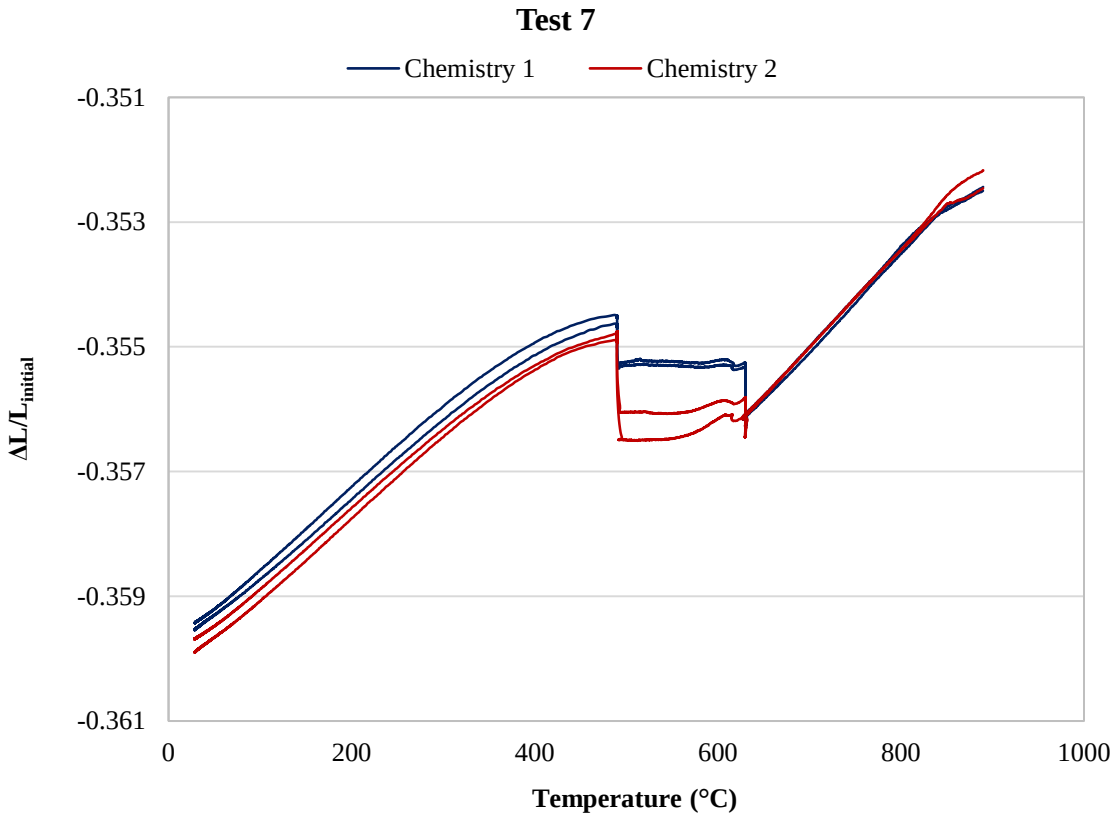

Figure 4.57. Cooling curves from test 7

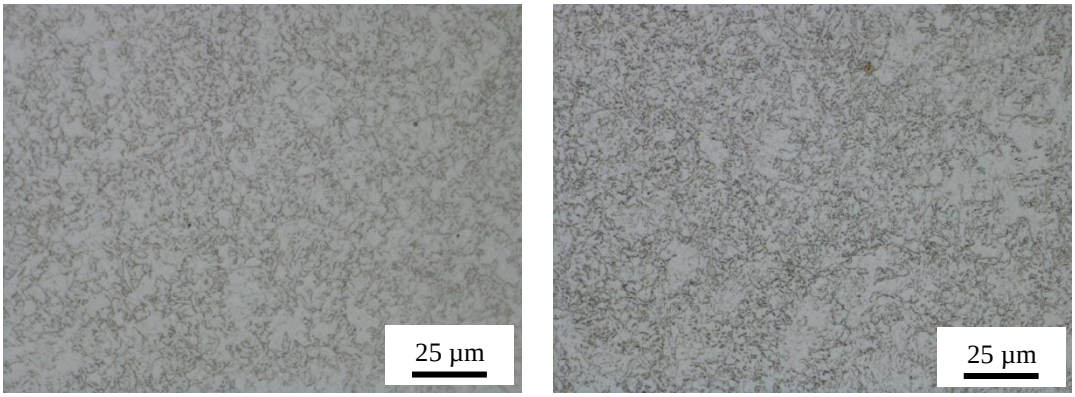

a. Chemistry 1, test 7, 500x magnification b. Chemistry 2, test 7, 500x magnification

Figure 4.58. Optical microscopy of final microstructure from test 7

In general, the following statements can be made. The transformation to ferrite during isothermal holding at 630 °C is smaller for the vanadium containing chemistry. During the subsequent quench to room temperature where the remaining austenite transforms to martensite, the transformation is larger for the vanadium containing chemistry. The transformation start temperature during quenching shifts to higher temperatures for the vanadium containing chemistry. During isothermal holding at 490 °C, the transformation to bainite is larger for the vanadium containing chemistry. When deformation is applied at the finishing temperature, the transformation occurring at the 630 °C isotherm increases. The transformation at the 490 °C isotherm decreases with strain in chemistry 1 and increases slightly in chemistry 2.

Chapter 5

Discussion

Coiling at 610 °C leads to ferritic microstructures, while coiling at 490 °C leads to the formation of bainite. The mechanical properties and corresponding microstructural features will, therefore, be discussed based on the CT. Samples with a CT of 610 °C are discussed first (4.1), followed by samples with a CT of 490 °C (4.2) and finally samples with intermediate cooling and a CT of 490 °C (4.3).

5.1 610 °C Coiling Temperature

At a CT of 610 °C the samples are largely ferritic with regions of martensite. The CCT curves predict this microstructure and the dilatometry results also confirm both the austenite to ferrite and the austenite to martensite transformations in tests 2 and 4. When the steel is cooled from the FT to the CT of 610 °C, the ferrite transformation occurs. The solubility of carbon in ferrite is low so as it forms, carbon is pushed out into the austenite.

This stabilizes the austenite, lowering the martensite start temperature of the remaining austenite. During cooling to room temperature, the remaining austenite transforms to martensite. This is confirmed by the dilatometry results of tests 2 and 4 which contain a combination of both ferrite and martensite after isothermal holding at 630 °C for 300 s and quenching to room temperature. The TEM thin foil analysis also shows a dislocation sub-structure within the ferrite and some regions of Widmanstatten ferrite or bainite.

To compare the strength of different samples, the trends in the UTS values are clearer than the trends in YS values. For this reason, the UTS values will be used more frequently. With a CT of 610 °C, all chemistries with the exception of the base chemistry saw an increase in UTS with an increase in FT from 890 °C to 950 °C. Chemistry D processed with a FT of 950 °C achieves a UTS and YS beyond the targets of 980 MPa and 800 MPa but the target HER of 50% is not achieved by any of the samples at a CT of 610 °C. The samples processed with a FT of 890 °C were not studied extensively but based on the results of the samples with a FT of 950 °C, the strengthening contributions can be surmised.

With an increase in FT from 890 °C to 950 °C, the UTS of chemistries B, C and D increase. The average UTS of chemistry B increases by 44 MPa, chemistry C by 113 MPa and chemistry D by 92 MPa with a FT of 950 °C in comparison to 890 °C. The average UTS for chemistry B increases by 44 MPa but the standard deviation error bars are overlapping, showing that this increase is less significant. Given that the increase in UTS is especially high for chemistries C and D which contain higher niobium and

vanadium, it is likely that the increase in strength can be attributed to increased precipitation strengthening. A FT of 890 °C would reduce the solubility of microalloyed carbonitrides and promote strain-induced precipitation in the austenite during hot rolling, thereby reducing the amount of solute available for interphase precipitation during the austenite to ferrite transformation. Since a fine distribution of precipitates is required for a high strengthening contribution, the overall contribution to the strength of the material from precipitation would decrease as a result.

It is important to consider the interpass time with respect to precipitation strengthening. The steel sheet was held between finishing passes to allow it to air cool to the temperature set for the next rolling pass. This provides time for diffusion to occur and precipitates to nucleate and grow in the austenite. The interpass time between passes 1 - 4 was approximately 14 seconds for the material with a FT of 890 °C and 7 seconds for material processed with a FT of 950 °C. After pass 4, the steel was at a temperature of approximately 1000 °C to 1100 °C. From passes 4 - 7, the average interpass time is about one second longer for the material with the lower FT. The longer interpass time for the material process at 890 °C would result in a larger volume fraction of precipitates in the austenite, limiting interphase precipitation and lowering the total precipitation strengthening contribution.

Evidence of a fine distribution of precipitates in the samples processed with a FT of 950 °C is seen in the TEM and APT analyses of chemistries C and D. Based on the TEM thin foil analysis, the distribution is random in chemistry C. If the electron beam is

not aligned parallel to the sheet of interphase precipitates, the characteristic rows will not be observed, and interphase precipitates may appear to be distributed randomly [44]. However, it is also possible that the fine precipitates (<10 nm) formed after transformation in the ferrite resulting in a random distribution. The defined rows of precipitates seen in chemistry D are characteristic of interphase precipitation and demonstrate that the processing conditions and chemistry were suitable for interphase precipitation to occur.

An important finding is seen in the precipitate size distribution of chemistries C and D which shows a marked increase in frequency of precipitates <10 nm in diameter in chemistry D. Based on these results, it can be concluded that the difference in strength between chemistries C and D processed at 950-610 is due to interphase precipitation which is promoted by the addition of vanadium. This assumes that all other strengthening mechanisms are relatively unaffected.

The importance of particle spacing is discussed by various researchers [5], [45], [46]. The Ashby-Orowan equation for precipitation strengthening is often presented as a function of volume fraction and precipitate diameter. Strengthening increases with decreasing particle spacing and this can be accounted for with volume fraction and particle diameter. For a given volume fraction of precipitates, the particle spacing decreases with decreasing precipitate diameter and for a given particle diameter, the particle spacing decreases with increasing volume fraction. Particle spacing is incorporated into the Ashby-Orowan equation using equations (5.1) to (5.3) taken from

Kamikawa et al [5] where v is Poisson's ratio, L is the spacing between precipitates, x is the average particle diameter on the slip plane and r and f are the average radius and volume fraction of the precipitates respectively.

$$\sigma_{ppt} = \left(\frac{0.8MGb}{2\pi\sqrt{1-vL}}\right) * \left(\ln\left(\frac{x}{2b}\right)\right) \quad (5.1)$$

$$L = \sqrt{\frac{2}{3}}\left(\sqrt{\frac{\pi}{f}} - 2\right)r \quad (5.2)$$

$$x = 2\sqrt{\frac{2}{3}}r \quad (5.3)$$

The solid solution strengthening contribution is affected by how much precipitation occurs. A larger volume fraction of precipitates reduces the amount of solute in solution, lowering the solid solution strengthening contribution. Since more precipitation in austenite is expected to occur with a lower FT, the solid solution strengthening contribution would also decrease. It is assumed that the solid solution strengthening contribution is the same across all chemistries processed at each set of processing parameters. The contribution from V and Nb is small [39] and although carbon has a large solute strengthening coefficient, due to its low solubility in ferrite at room temperature, most of the carbon exists in carbides and its contribution to solute strengthening is small [47].

The grain size measurements showed little difference in grain size between the different samples. With the decrease in FT from 950 °C to 890 °C, the grain size of chemistries C and D increase by 0.2 µm and 0.3 µm respectively. Accounting for error in the grain size measurements and given the difference in grain size of only 0.3 µm between the two finishing temperatures, it can be concluded that the FT had little effect on the grain size. In addition, the difference of 0.3 µm would only account for 33 MPa of strength using the Hall-Petch equation (5.4), showing that the difference in grain size does not explain the total increase in strength, again pointing to the importance of precipitation strengthening.

$$\sigma_{gb} = 0.55d^{-1/2} \quad (5.4)$$

The FT of 890 °C was expected to produce a more pancaked microstructure with finer grain size due to the effect of retained strain when hot rolling below T_{nr}. Since no impact of FT on grain size was observed, it was concluded that the FT was not far enough below T_{nr} to observe the effect of retained strain.

The final strengthening contribution to be considered is dislocation strengthening. In this case, a combination of ferrite and martensite, with small fractions of bainite are observed. Various researchers apply a law of mixtures shown in equation (5.5) when determining the strength of steel with multiple phases [48], [49]. The strength can simply be represented by summation of the strength of each component (σ_i) multiplied by the component's volume fraction (V_i).

$$\sigma = \sum_{i=1}^{N} V_i \sigma_i \quad (5.5)$$

The semi-quantitative martensite fractions for each sample were given in Table 4.1 which can be used for comparison purposes between the samples. Two points can be concluded from these values. First, in comparison to the other chemistries, the martensite fraction is highest for chemistry B when processed at both 890-610 and 950-610. This is likely a result of the increased hardenability that comes with increasing the carbon content from 0.08 wt% to 0.11 wt%, promoting the formation of martensite.

Second, the martensite fraction is higher for the samples with a higher FT. A comparison of the results from dilatometry tests 2 and 4 can be used to determine the effect of deformation applied below T_{nr} (as seen in test 4) on the phase transformations. The second deformation step promotes the ferrite transformation, reducing the amount of martensite formed during cooling from 630 °C to RT. This explains the results showing that the martensite fraction is lower in the samples processed with a FT of 890 °C. With a higher martensite fraction in the material with a FT of 950 °C, the dislocation density increases which would have a contribution to the increase in strength. At the same time, the increased fraction of a brittle phase can negatively affect the elongation values. This is also seen in the results where, aside from chemistry B, the UE values decrease with increased strength at the higher FT.

Finally, the HER will be discussed for these eight samples. The FT seems to have little effect on the HER but the effect of chemistry may be more important. According to

literature, inhomogeneities within the microstructure impact the HER. Mechanical contrast between phases with hardness variations, such as ferrite and martensite, leads to damage nucleation during hole expansion testing [50], [51]. Chemistry B has the lowest HER for both 890-610 and 950-610 samples. As stated, chemistry B also contains the highest martensite fraction compared to the other chemistries. Another possible explanation is a larger fraction of large carbonitrides which form early in the hot rolling process and act as nucleation sites for cracks during the hole expansion test [50], [51]. Given the higher carbon content of chemistry B this also offers an explanation as to why the HER is lower than the other chemistries.

5.2 490 °C CT

With a reduced CT of 490 °C, the samples have a lath bainite and granular bainite or degenerate ferrite morphology. This was predicted using the CCT diagrams and is confirmed by the dilatometry results from tests 3 and 5 showing that the bainite transformation occurs during isothermal holding at 490 °C.

A FT of 890 °C as compared to 950 °C has little effect on the UTS values, showing that the impact of cooling rate overshadows the effect of FT on the strengthening mechanisms. The UTS values of samples with a 490 °C CT are similar to the samples processed at 890-610 and none of the UTS values reach the target UTS. At both 890-490 and 950-490, the UTS increases sequentially from chemistries A to D where the largest jump in strength is seen for chemistry D which is approximately 100 MPa higher than the other chemistries on average. The FT does not affect the UE which

can be expected given the fact that the FT also has little effect on the UTS and YS. The UE is lower in the samples coiled at 490 °C compared to the samples coiled at 610 °C.

The lath width and dislocation density are important contributors to the strength of the material. The literature review found that precipitation strengthening plays a role but is less important than the former strengthening mechanisms in bainite. The impact of chemistry on the UTS is the most important observation for the samples coiled at 490 °C. With a higher carbon content, the hardenability of chemistry B increases, refining the bainitic structure and explaining the increase in strength from the base chemistry. The increased niobium content of chemistry C produces UTS values close to those of chemistry B. Since precipitation is expected to be minimal because of the low CT, this may show that niobium has a similar effect as vanadium in limiting recovery, strengthening bainite by increasing dislocation density. The largest increase in strength is seen in chemistry D with the addition of vanadium. As discussed, vanadium has been shown to limit recovery so that a relatively high dislocation density is maintained after coiling.

The grain boundary strengthening depends on lath width in lath bainite or grain size in granular bainite. Whether granular or lath bainite is present, the microstructures of the samples processed with a 490 °C CT are much finer than those processed with a CT of 610 °C. This would cause increased strengthening due to grain size but the UTS values do not reflect this which shows that strength from other strengthening mechanisms, primarily precipitation strengthening, is lost with a reduction in CT. The lath width

strengthening contribution can be determined for chemistries A and B processed at 950-490 using the EBSD measurements of approximately 0.5 µm.

The difference in bainite morphology between chemistries A and B as compared to chemistries C and D processed at 950-490 must be addressed. Chemistries A and B contain mostly lath bainite while chemistries C and D contain granular bainite or degenerate ferrite with a dislocation sub-structure as shown in the TEM thin foils. The samples from chemistries C and D were isothermally held at the CT of 490 °C for one hour before cooling to RT at a rate of 30 °C/h while chemistries A and B began cooling to RT as soon as they were placed in the coiling furnace. This was to make effective use of coiling furnace space during hot rolling. Based on findings in literature, bainite granularization can occur during isothermal holding, where dislocation recovery results in the formation of granular bainite from lath bainite [52], [53]. The differences in bainite morphology is not evident in the mechanical properties.

Precipitation strengthening is not expected to have as significant a contribution in samples coiled at 490 °C as the samples coiled at 610 °C. The cooling rate from the FT to 490 °C is too high for interphase precipitation to occur during the austenite to bainite transformation. Consequently, fine precipitates are less likely to be found in the final microstructure given the processing temperatures. The APT datasets do show some clustering of vanadium and carbon in the lower carbon regions which may contribute to the strength of the material. It cannot be determined from the results however, whether segregation is occurring uniformly throughout the sample or whether these precipitates

formed in the austenite or in the bainite after the bainite transformation. Based on the second APT dataset, it can simply be concluded that a fine distribution of vanadium and carbon segregation is possible.

5.3 Intermediate Cooling

This final section will cover the samples with intermediate cooling. These samples have a lath bainite structure with some granular bainite as seen in the SEM and thin foil images. The dilatometry results from test 7 show that the ferrite transformation begins during isothermal holding at 630 °C. The addition of vanadium limits this transformation. During cooling to the second isothermal holding step at 490 °C, a transformation is also occurring which competes with thermal contraction of the specimen as evidenced by the small reduction in length. At 490 °C, the bainite transformation proceeds. With a FT of 890 °C the UTS is very similar to the samples without intermediate cooling. When the FT is increased to 950 °C the UTS increases by an average of 70 MPa across all chemistries resulting in UTS values comparable to the values for samples processed at 950-610. The UTS of chemistry D processed with a 950 °C FT surpasses the target UTS of 980 MPa.

Intermediate cooling also improves the YS in comparison to other TMP parameters. With a FT of 950 °C the YS of chemistries A, C and D are all above the target YS of 800 MPa. The elongation values drop with increasing UTS and YS for the high FT samples. Although these samples have the lowest elongation values of all

processing parameters, the average TE values of all chemistries are above 11% which is sufficient for this product.

Aside from chemistry B, the HER of these samples is also high when processed at 950-630-490 in comparison to the other processing temperatures. The base chemistry reaches a HER of 68% when processed with a FT of 950 °C although the large SD shows that there is inconsistency in the measurements. The average HER of chemistry C is 45% which is 10% higher than the next highest HER value for chemistry C processed at 890-630-490. The average HER of chemistry D is 41.4% and approximately 4% higher than the next highest value processed at 890-610. The combination of high HER and strength are what distinguishes 950-630-490 as the most favourable processing temperatures.

The microstructure is fairly uniform and less hardness deviations are expected than in the samples coiled at 610 °C. However, the HER still does not reach the target properties. The coarse precipitates formed at high temperatures during the long interpass times could be a contributing factor as sources for crack nucleation during hole expansion testing [50], [51].

Since microstructural analysis of the samples processed at 890-630-490 was limited to optical microscopy and SEM, most of the conclusions about the relationship between microstructure and mechanical properties will be drawn from the samples processed at 950-630-490. The microstructure of all chemistries from both finishing temperatures is largely composed of lath bainite. As a result, the primary strengthening

contributions in these samples is expected to come from a fine lath width and high dislocation density.

The strength increase with FT can be explained largely by an increase in dislocation density. Based on SEM imaging, the samples processed with a lower FT of 890 °C contain more granular bainite or degenerate ferrite than the samples with a FT of 950 °C which primarily contains lath bainite. During the 5 s isothermal holding step at 630 °C, the austenite to ferrite transformation is promoted more in the sample with a FT of 890 °C than with a FT of 950 °C because of higher levels of retained strain. This is confirmed by the dilatometry data comparing the transformation during isothermal holding in tests 2 (without deformation) and test 4 (with deformation and analogous to a FT of 890 °C). More ferrite forms in the sample from test 4, consequently limiting the bainite transformation at 490 °C. The larger ferrite fraction and smaller bainite fraction results in an overall decrease in dislocation density. As discussed previously, it is also likely that with a lower FT, a larger portion of solute formed relatively large precipitates in the austenite, reducing solute strengthening and precipitation strengthening.

TEM thin foils were used to analyze the microstructure of chemistries C and D processed at 950-630-490 to determine the effect of added vanadium in chemistry D. In chemistry C, cementite particles exist in the martensite laths and carbides are present at the lath boundaries which is not the case for chemistry D. As described by Edmonds and Cochrane, interstitial carbon can be bound to dislocations, causing carbon to remain in solution [49]. Since vanadium has been shown to limit recovery, a higher dislocation

density in the vanadium containing samples will cause more carbon to remain in solution. The APT datasets of chemistry D also show co-segregation of carbon and vanadium which shows that vanadium competes with iron, preventing the formation of cementite particles and large carbides between laths as seen in chemistry C. Although dislocation density was not measured, based on evidence presented in the literature review it can be concluded that the effect of vanadium on strength is due to an increased dislocation density.

Neither precipitation strengthening or differences in lath width can be used to explain the increased strength of chemistry D. The extraction replicas show few small precipitates <10 nm in diameter. The small fraction of precipitates that were found may have formed during the austenite to ferrite transformation at 630 °C. EDS of the coarse and fine precipitates show that the fine precipitates contain more Nb and V than the coarse precipitates. Therefore, the formation of fine precipitates was promoted by the microalloying additions, but the limited quantity has a small effect on strength. The clustering seen in the APT datasets could also have a small contribution to the strength but the uniformity throughout the sample is unknown. The effect of chemistry on lath width is insignificant. The lath width of chemistries B, C and D with a FT of 950 °C were measured using EBSD and TEM thin foil analysis and range from 0.30 µm to 0.36 µm. Therefore, an increase in dislocation density remains a more suitable explanation for the strength increase in chemistry D.

The samples processed at 950-630-490 have a higher strength than those processed at 950-490. The SEM images of the samples with and without intermediate cooling show that intermediate cooling refines the bainite lath structure. This can be seen in the EBSD lath width measurements of chemistry B when processed at 950-490 as compared to 950-630-490 where the lath width is 0.49 μm and 0.36 μm respectively. One possible explanation is that the intermediate cooling step and reduced cooling rate from 630 °C to 490 °C allows more segregation of vanadium to occur, preventing recovery and refining the bainite structure.

5.4 Strength Calculations

The strength can be broken down into individual strengthening mechanisms using the results. The effect of solid solution strengthening, grain size, precipitation and dislocation strengthening can be approximately calculated to determine which strengthening mechanisms helped to achieve a high strength material.

The solid solution strengthening contribution can be estimated by determining how much solute precipitates out of the matrix and how much is left in solution to contribute to solute strengthening. As discussed in the chapter 2, the weight fraction of solute which precipitates out was determined with a combination of ThermoCalc and the TMP model. The Scheil solidification model provides information on the composition of precipitates that form during solidification, the TMP model developed at McMaster University can estimate how much precipitation subsequently occurs during hot rolling and finally, the matrix composition after TMP is input into ThermoCalc to determine how

much precipitation occurs during coiling at 610 °C. Following these steps and using equation (5.6) with solid solution strengthening coefficients provided by Gladman, the solid solution strengthening contribution was estimated at 100 MPa for all samples.

$$\sigma_{ss} = 5082[C] + 31.5[Mn] + 83[Si] + 11[Mo] - 31[Cr] \quad (5.6)$$

Carbon, manganese and silicon have the largest solid solution strengthening coefficients. However, the strengthening contribution from carbon is minimal since much of it exists in precipitates. It is assumed that the nitrogen and titanium have precipitated out as TiN at high temperatures and do not contribute to solid solution strengthening. Taking these assumptions into account, the difference in solid solution strengthening at different coiling temperatures is small.

5.4.1 Ferritic Microstructures

Chemistries C and D processed at 950-610 were studied extensively and will be used to investigate the breakdown of strengthening contributions. The grain strengthening contribution is high due to the small grain size. Equation (5.4) was used to calculate a strengthening contribution of 390 MPa with an approximate grain size of 2 μm. This contribution is high but could be affected by the inclusion of martensite in the grain size measurements.

The dislocation density was not measured but can be estimated based on work of other researchers. The dislocation density in a similar microalloyed ferritic steel was estimated at 5.2 x 10^{13} m^{-2} in work by Kestenbach et al. [44]. Kimikawa et al. measured a dislocation density between 2.7 – 8 x 10^{13} m^{-2} for vanadium microalloyed ferrite.

Assuming a dislocation density of 5 x 10^{13} m^{-2}, the dislocation strengthening contribution is 150 MPa using equation (1.17) from the literature review.

The Ashby-Orowan equation is used to determine precipitation strengthening with the measured volume fraction and average diameter of precipitates. In the extraction replicas for chemistries C and D, the precipitate size distribution was determined only from regions where precipitates were present, so the overall volume fraction is unknown since the precipitates are not distributed uniformly through the sample. This was seen in the thin foil images which show an uneven distribution even within individual grains which has also been observed by other researchers [54]. Kestenbach et al. performed a statistical analysis on the precipitate size distribution and determined that interphase precipitation existed in 50% of the ferrite grains [44].

Without a measured volume fraction, the precipitate strengthening contribution is determined by eliminating the other strengthening contributions from the experimentally measured yield strength. The experimentally measured YS of chemistries C and D processed at 950-610 are approximately 700 and 880 MPa respectively. With an intrinsic strength of 50 MPa, solid solution strengthening of 100 MPa, grain size strengthening of 390 MPa and dislocation strengthening of 150 MPa a linear addition of the strengthening mechanisms provides a strength of 690 MPa without yet accounting for precipitation strengthening. The precipitation strengthening contribution in chemistry C is more than 10 MPa and therefore it is concluded along with Kamikawa et al. that a linear addition of precipitation and dislocation strengthening overestimates the contribution of these

factors. Instead, a square root of the sum of squares is taken [5],[28]. Using this method and assuming all other strengthening contributions remain the same, the precipitation strengthening in chemistries C and D are 56 and 305 MPa respectively. The combined contribution with 150 MPa dislocation strengthening contribution is 160 and 340 MPa respectively. The strengthening contributions of these two chemistries are summarized in Table 5.1.

Table 5.1. Breakdown of strengthening mechanisms in chemistries C and D processed at 950-610

Chemistry	σ_y **(exp)**	σ_0	σ_{ss}	σ_{gb}	σ_{ppt}	σ_{dis}	$\sigma_{ppt}+\sigma_{disl}$	$\sqrt{\sigma_{ppt}^2+\sigma_{dis}^2}$
C	700	50	100	390	56	150	206	160
D	880	50	100	390	305	150	455	340

The approximate volume fraction of precipitates can be calculated using the Ashby-Orowan equation. Focusing on the particles <20 nm in diameter [5], the average particle diameter is 8.5 nm in chemistry C and 7.5 nm in chemistry D. The volume fraction of precipitates in chemistries C and D are determined to be 0.0003 and 0.0077 respectively, demonstrating the important effect of vanadium on producing a relatively high volume fraction of fine precipitates important for strengthening.

5.4.2 Bainitic Microstructures

The UTS values show an increase of 80 MPa for chemistry D while the YS only has an increase of 31 MPa. There is a large SD in both UTS and YS values in this case so an increase in YS of 55 MPa will be estimated for the following calculations. This is assumed to be a result of dislocation strengthening. The lath width is approximated at

0.32 μm for both chemistries C and D. Using equation (1.18) and the constants provided by Fazeli et al. as found in the literature review, the contribution to strengthening from lath width is approximately 360 MPa.

The volume fraction of precipitates <20 nm is size for chemistry D is 0.0003 with an average diameter of 12.5 nm as determined from the extraction replicas. This corresponds to a strengthening contribution of 42 MPa but must be combined with dislocation strengthening using the square root of the sum of squares. The volume fraction of fine precipitates in chemistry C was not measured but is expected to be approximately the same given that the results for chemistry B are also very similar to chemistry D. It must be noted that when combined with the large dislocation strengthening contribution, the effect of precipitation strengthening is very small.

A bainitic microstructure contains a higher dislocation density than ferrite [47]. Edmonds and Cochrane state a dislocation density of 10^{14} m^{-2} for bainitic structures [49]. Kamikawa et al. provide a dislocation density of 1.5 – 1.9 x 10^{14} m^{-2} for vanadium microalloyed bainite [5]. Fazeli et al. used a dislocation density of 3.34 x 10^{14} m^{-2} for a vanadium free bainitic steel and 5.8 x 10^{14} m^{-2} for a vanadium containing steel [28]. This shows a large range in dislocation densities depending on processing conditions and alloying. For the current steels, using values of 50 MPa and 100 MPa for intrinsic and solid solution strengthening and the calculated values for precipitation and lath width strengthening, the dislocation strengthening contribution can be determined. The dislocation density of chemistries C and D are calculated at 2.9 x 10^{14} m^{-2} and

3.8×10^{14} m^{-2} respectively which are reasonable based on the values stated from literature.

The summary of the individual strengthening contribution is shown in Table 5.2 based on YS values of 870 MPa and 925 MPa. These do not equal the measured values but are used to illustrate an assumed difference in YS of 55 MPa. Multiple assumptions are made here but this method illustrates how the strength of a bainitic microstructure can be split into their individual components and the effect of vanadium on the dislocation density.

Table 5.2. Breakdown of strengthening mechanisms in chemistries C and D processed at 950-630-490

Chemistry	σ_y (approx)	σ_0	σ_{ss}	σ_{lath}	σ_{ppt}	σ_{disl}	$\sigma_{ppt}+\sigma_{dis}$	$\sqrt{\sigma_{ppt}^2+\sigma_{dis}^2}$
C	870	50	100	360	42	358	400	361
D	925	50	100	360	42	413	455	416

5.5 Recommendations

The processing parameters of 950-610 and 950-630-490 and microalloying with vanadium produced ferritic and bainitic microstructures respectively with the most favourable mechanical properties. The long interpass times used in the pilot mill had a negative impact on the mechanical properties. It is expected that using shorter interpass times, like those used in industrial steel processing, will further improve the properties.

In a ferritic structure, shorter interpass times will reduce the amount of coarse precipitates that form at higher temperatures, thereby leaving more solute available for increased strengthening. To achieve the target HER, inhomogeneities in the

microstructure must be eliminated including martensitic regions and large coarse precipitates. A shorter interpass time is expected to have this effect by reducing the amount of coarse precipitates. To reduce the fraction of martensite in the ferrite, it may be beneficial to lower the alloying content of elements which increase the steel hardenability including C, Mn, Mo, Cr. This will reduce their solid solution strengthening contribution but the reduction will be insignificant with the increase in precipitation strengthening.

The bainitic structures will also benefit from shorter interpass times for the same reasons stated. The main issue with this material was the HER. Since it is expected that the HER was negatively affected by coarse precipitation, a shorter interpass time may enable a HER past the target value.

Increased precipitation strengthening with shorter interpass times may also allow for the reduction of microalloying elements, niobium and vanadium. These samples showed that vanadium promoted interphase precipitation. In contrast, interphase precipitation was not observed in the steels that only contained Nb. This could be because niobium had already precipitated out in the austenite during hot rolling. With shorter interpass times, more niobium would remain in solution and could contribute to interphase precipitation during the austenite to ferrite transformation along with vanadium. Shorter interpass times would allow expensive microalloying additions to be used more efficiently for strengthening, so that their content can be reduced.

Chapter 6

Conclusions

This work has determined how a range of TMP parameters and alloying contents affect the microstructural features and corresponding mechanical properties of a microalloyed steel. This knowledge helps in the selection of processing conditions and alloying contents to produce a material that achieves the desired strength and stretch flangeability for structural automotive applications.

The most important result of varying the FT was seen in its effect on precipitation strengthening. At a FT of 950 °C as compared to 890 °C, less precipitation in the austenite occurs during hot rolling. This leaves higher concentrations of solute available to form interphase precipitates during the austenite to ferrite transformation in ferritic microstructures or to contribute to the strength of bainitic structures.

When considering CT, a higher CT of 610 °C produces a ferritic structure where the primary sources of strength come from fine ferrite grain size and precipitation strengthening from interphase precipitation. With a CT of 490 °C a bainitic structure forms where the main strengthening contributions come from a fine lath width and high dislocation density. A low CT prevents significant strengthening from precipitation.

With a high FT and low CT, an intermediate cooling step increases the strength of the material and produces the best HER compared to all other processing parameters studied. Inhomogeneities in the microstructure contributed to poor stretch flangeability. Less inhomogeneities were seen in the samples with intermediate cooling as compared to the ferritic samples coiled at 610 °C where the presence of martensitic regions contributed to hardness deviations.

The addition of vanadium increases the strength of both ferritic and bainitic structures. Vanadium increases precipitation strengthening in ferrite by promoting interphase precipitation and contributes to dislocation strengthening in bainite by retarding recovery during coiling.

The processing parameters and microalloying additions recommended for achieving the target mechanical properties are 950-630-490 with the addition of V. To further improve on the mechanical properties achieved in this work, the section 5.5 outlines how shorter interpass times will benefit the HER, which is expected to produce a material that achieves all of the target mechanical properties.

REFERENCES

[1] M. Meyers and K. Chawla, Mechanical Behavior of Materials, New York: Cambridge University Press, 2009.

[2] W. D. Callister, Materials Science and Engineering An Introduction, New York: John Wiley & Sons, Inc., 2007.

[3] T. Gladman, The Physical Metallurgy of Microalloyed Steels, London: The Institute of Materials, 1997.

[4] T. Courtney, Mechanical Behavior of Materials, Long Grove: Waveland Press, Inc., 2000.

[5] N. Kamikawa, K. Sato, G. Miyamoto, M. Murayam, N. Sekido, K. Tsuzaki and T. Furuhara, "Stress-Strain Behavior of Ferrite and Bainite with Nano-Precipitation in Low Carbon Steels," *Acta Materialia,* vol. 83, pp. 383-396, 2015.

[6] X. Mao, X. Huo, X. Sun and Y. Chai, "Strengthening Mechanisms of a New 700 MPa Hot Rolled Ti-Microalloyed Steel Produced by Compact Strip Production," *Journal of Materials Processing Technology,* vol. 210, pp. 1660-1666, 2010.

[7] Y. Funakawa, T. Shiozaki, K. Tomita, T. Yamamoto and E. Maeda, "Development of High Strength Hot-Rolled Sheet Steel Consisting of Ferrite and Nanometer-Sized Carbides," *ISIJ International,* vol. 44, no. 11, pp. 1945-1951, 2004.

[8] Y. Saito, "Modelling of Microstructural Evolution in Thermomechanical Processing of Structural Steels," *Materials Science and Engineering A,* vol. 223, no. 1-2, pp. 134-145, 1997.

[9] M. Militzer, E. B. Hawbolt and T. R. Meadowcroft, "Microstructural Model for Hot Strip Rolling of High-Strength Low-Alloy Steels," *Metallurgical and Materials Transactions A,* pp. 1247-1259, 2000.

[10] P. D. Hodgson and R. K. Gibbs, "A Mathematical Model to Predict the Mechanical Properties of Hot Rolled C-Mn and Microalloyed Steels," *ISIJ International,* pp. 1329-1338, 1992.

[11] K. Zhang, Z. Li, Z. Wang, X. Sun and Q. Yong, "Precipitation Behavior and Mechanical Properties of Hot-Rolled High Strength Ti-Mo Bearing Ferritic Sheet Steel," *Journal of Materials Research,* vol. 31, no. 9, pp. 1254-1263, 2016.

[12] B. Dutta and C. M. Sellars, "Effect of Composition and Process Variables on Nb(C,N) Precipitation in Niobium Microalloyed Austenite," *Materials Science and Technology,* vol. 3, pp. 197-206, 1987.

[13] K. Rehman and H. S. Zurob, "Novel Approach to the Static Recrystallization of Austenite During Hot-Rolling of Nb-Microalloyed Steel: Effect of Precipitates," *Materials Science Forum,* vol. 753, pp. 417-422, 2013.

[14] C. M. Sellars and J. A. Whiteman, "Recrystallization and Grain Growth in Hot Rolling," *Metal Science,* Vols. March-April, pp. 187-194, 1979.

[15] C. Sellars and J. Beynon, "Conference Proceedings on High Strength Low Alloy Steels," Wollongong, 1984.

[16] M. Umemoto, Z. H. Guo and I. Tamura, "Effect of Colling Rate on Grain Size of Ferrite in a Carbon Steel," *Materials Science and Technology,* pp. 249-255, 1987.

[17] M. Suehiro, K. Sato, Y. Tsukano, H. Yada, T. Senuma and Y. Matsumura, "Computer Modeling of Microstructural Change and Strength of Low Carbon Steel in Hot Strip Rolling," *Transactions ISIJ,* vol. 27, pp. 439-445, 1987.

[18] N. Kamikawa, "Tensile Behavior of Ti,Mo-added Low Carbon Steels with Interphase Precipitation," *ISIJ International,* vol. 24, no. 1, pp. 212-221, 2014.

[19] R. Honeycombe, "Transformation from Austenite in Alloy Steels," *Metallurgical Transactions A,* vol. 7A, no. July, pp. 915-936, 1976.

[20] S. Nafisi, B. S. Amirkhiz, F. Fazeli, M. Arafin, R. Glodowski and L. Collins, "Effect of Vanadium Addition on the Strength of API X100 Linepipe Steel," *ISIJ International,* vol. 56, no. 1, pp. 154-160, 2016.

[21] R. A. Ricks and P. R. Howell, "The Formation of Discrete Precipitate Dispersions on Mobile Interphase Boundaries in Iron-Base Alloys," *Acta Metallurgica,* vol. 31, no. 6, pp. 853-861, 1983.

[22] G. Miyamoto, R. Hori, B. Poorganji and T. Furuhara, "Interphase Precipitation of VC and Resultant Hardening in V-added Medium Carbon Steels," *ISIJ International,* vol. 51, no. 10, pp. 1733-1739, 2011.

[23] Y. Zhang, G. Miyamoto, K. Shinbo, T. Furuhara, T. Ohmura, T. Suzuki and K. Tsuzaki, "Effects of Transformation Temperature on VC Interphase Precipitation and Resultant Hardness in Low-Carbon Steels," *Acta Materialia,* vol. 84, pp. 375-384, 2015.

[24] E. J. Chun, D. Hyeonghyeop, S. Kim, D.-G. Nam, Y.-H. Park and N. Kang, "Effect of nanocarbides and interphase hardness deviation on stretch-flangeability in 998 MPa hot-rolled steels," *Materials Chemistry and Physics,* no. 104, pp. 307-315, 2013.

[25] J. Jang, Y. Heo, C. Lee, H. Bhadeshia and D. Suh, "Interphase Precipitation in Ti-Nb and Ti-Nb-Mo Bearing Steel," *Materials Science and Technology,* vol. 29, no. 3, pp. 309-313, 2013.

[26] C. Y. Chen, C. C. Chen and J. R. Yang, "Microstructure Characterization of Nanometer Carbides Heterogeneous Precipitation in Ti-Nb and Ti-Nb-Mo Steel," *Materials Characterization,* vol. 88, pp. 69-79, 2014.

[27] H. Kestenbach, "Dispersion Hardening by Niobium Carbonitride Precipitation in Ferrite," *Materials Science and Technology,* vol. 13, no. 9, pp. 731-739, 1997.

[28] F. Fazeli, B. S. Amirkhiz, C. Scott, M. Arafin and L. Collins, "Kinetics and Microstructural Change of Low-Carbon Bainite Due to Vanadium Microalloying," *Materials Science and Engineering A,* vol. 720, pp. 248-256, 2018.

[29] T. Siwecki, J. Eliasson, R. Lagneborg and B. Hutchinson, "Vanadium Microalloyed Bainitic Hot Strip Steels," *ISIJ International,* vol. 50, no. 5, pp. 760-767, 2010.

[30] K. Zhu, O. Bouaziz, C. Oberbillig and M. Huang, "An Approach to Define the Effective Lath Size Controlling Yield Strength of Bainite," *Materials Science and Engineering A,* vol. 527, pp. 6614-6619, 2010.

[31] D. Kuhlmann-Wilsdorf, "The Theory of Dislocation-Based Crystal Plasticity," *Philosophical Magazine A,* vol. 79, no. 4, pp. 955-1008, 1999.

[32] J.-C. Hell, M. Dehmas, S. Allain, J. M. Prado, A. Hazotte and J.-P. Chateau, "Microstructure-Properties Relationships in Carbide-Free Bainitic Steels," *ISIJ International,* vol. 51, no. 10, pp. 1724-1732, 2011.

[33] H. Hu, H. S. Zurob, G. Xu, D. Embury and G. R. Purdy, "New Insights to the Effects of Ausforming on the Bainitic Transformation," *Materials Science and Engineering A,* vol. 626, pp. 34-40, 2015.

[34] S. Nafisi, "Impact of Vanadium Addition on API X100 Steel," *ISIJ International*, vol. 54, no. 10, pp. 2404-2410, 2014.

[35] A. Perlade, A. Amard, F. Pechenot, E. Stenback and J.-M. Pipard, "Hot-Rolled Steel Sheet and Associated Production Method". France Patent WO 2012/127125 A1, 27 September 2012.

[36] R. Okamoto, H. Taniguchi and M. Fukuda, "High Strength Hot Rolled Steel Sheet Excelling in Bore Expandability and Ductility and Process for Producing the Same". Japan Patent EP 1 607 489 B1, 21 December 2005.

[37] N. Kariya, S. Takagi, T. Shimizu, T. Mega, K. Sakata and H. Takahashi, "High Strength Hot-Rolled Steel Plate". Japan Patent EP 1 616 970 A1, 18 January 2006.

[38] K. Seto, Y. Funakawa and S. Kaneko, "Hot Rolled High Strength Steels for Suspension and Chassis Parts "NANOHITEN" and "BHT Steel"," JFE Technical Report, 2007.

[39] K. Zhang, Z.-D. Li, Q.-L. Yong, J.-W. Yang, Y.-M. Li and P.-L. Zhao, "Development of Ti-V-Mo Complex Microalloyed Hot-Rolled 900-MPa-Grade High-Strength Steel," *Acta Metallurgica*, vol. 28, no. 5, pp. 641-648, 2015.

[40] R. A. Rijkenberg and D. N. Hanlon, "Automotive Chassis Part made from High Strength Formable Hot Rolled Steel Sheet". USA Patent US 9908566 B2, 6 March 2018.

[41] C. Kami and K. Yamazaki, "High-Strength Hot Rolled Steel Sheet with Excellent Bendability and Low-Temperature Toughness and Method for Manufacturing the Same". USA Patent US 9752216 B2, 5 September 2017.

[42] R. Misra, H. Nathani, J. Hartmann and F. Siciliano, "Microstructural Evolution in a New 770 MPa Hot Rolled Nb-Ti Microalloyed Steel," *Materials Science and Engineering A*, vol. 394, pp. 339-352, 2005.

[43] "McMaster Steel Research Centre Online Models," McMaster University Steel Research Centre, [Online]. Available: https://srcentre.mcmaster.ca/models/. [Accessed April 2019].

[44] H. Kestenbach, S. Campos and E. Morales, "Role of Interphase Precipitation in Microalloyed Hot Strip Steels," *Materials Science and Technology*, vol. 22, no. 6, pp. 615-626, 2006.

[45] H. Kestenbach and J. Gallego, "On Dispersion Hardening of Microalloyed Hot Strip Steels By Carbonitride Precipitation in Austenite," *Scripta Materialia*, vol. 44, pp. 791-796, 2001.

[46] W. Sha, F. Kelly and Z. Guo, "Microstructure and Properties of Nippon Fire-Resistant Steels," *JMEPEG*, vol. 8, pp. 606-612, 1999.

[47] R. Misra, G. Weatherly, J. Hartmann and A. Boucek, "Ultrahigh Strengh Hot Rolled Microalloyed Steels: Microstructural Aspects of Development," *Materials Science and Technology*, vol. 17, pp. 1119-1129, 2001.

[48] N. Kamikawa, M. Hirohashi, Y. Sato, E. Cahndiran, G. Miyamoto and T. Furuhara, "Tensile Behavior of Ferrite-Martensite Dual Phase Steels with Nano-Precipitation of Vanadium Carbides," *ISIJ International*, vol. 55, no. 8, pp. 1781-1790, 2015.

[49] D. Edmonds and R. Cochrane, "Structure-Property Relationships in Bainitic Steels," *Metallurgical Transactions A*, vol. 21A, pp. 1527-1540, 1990.

[50] N. Pathak, C. Butcher, M. J. Worswick, E. Bellhouse and J. Gao, "Damage Evolution in Complex Phase and Dual Phase Steels During Edge Stretching," *Materials*, vol. 10, no. 346, pp. 1-29, 2017.

[51] H. Scott, J. Boyd and A. Pilkey, "Micro-Computered Tomographic Imaging of Void Damage in a Hot-Rolled Complex Phase Sheet Steel," *Materials Science and Engineering A*, vol. 682, pp. 139-146, 2017.

[52] M. B. H. Slama, N. Gey, L. Germain, K. Zhu and S. Allain, "Key Parameters to Promote Granularization of Lath-Like Bainite/Martensite in FeNiC Alloys During Isothermal Holding," *Materials*, vol. 11, no. 1808, pp. 1-13, 2018.

[53] H. Wu and G. Liang, "Evolutionary Mechanism of Ultra-Fine Bainite Ferrite During Reheating," *Reviews on Advanced Materials Science*, vol. 33, pp. 65-68, 2013.

[54] F. Bu, X. Wang, L. Chen, S. Yang, C. Shang and R. Misra, "Influence of Cooling Rate on teh Precipitation Behavior in Ti-Nb-Mo Microalloyed Steels During Continuous Cooling and Relationship to Strength," *Materials Characterization*, vol. 102, pp. 146-155, 2015.

Appendix A Mechanical Properties

Table A.1. Summary of average UTS, YS and HER including standard deviation

Processing Parameters	Chem	UTS (MPa)	UTS SD (MPa)	$YS_{0.5\%}$ (MPa)	$YS_{0.5\%}$ SD (MPa)	HER (%)	HER SD (%)
890-610	**A**	815	4	655	10	32	1.2
	B	843	35	656	7	25	0.7
	C	787	7	670	8	32	3.8
	D	921	15	849	13	38	10.7
950-610	**A**	800	17	624	19	33	2.1
	B	886	10	644	7	25	0.4
	C	900	10	700	13	32	2.3
	D	1013	6	882	33	35	2.5
890-490	**A**	818	33	649	47	45	9.3
	B	845	46	729	65	35	4.3
	C	852	5	652	23	34	1.6
	D	945	26	835	41	28	0.1
950-490	**A**	815	16	652	17	58	8.6
	B	858	39	736	58	44	8.4
	C	877	18	664	46	32	2.3
	D	947	25	762	19	32	3.7
890-630-490	**A**	801	14	741	20	48	10.0
	B	847	18	754	25	48	9.0
	C	831	29	737	22	35	0.2
	D	946	40	794	31	37	3.1
950-630-490	**A**	879	19	835	31	68	17.3
	B	896	31	799	79	41	9.2
	C	926	28	882	39	45	6.4
	D	1006	46	912	49	41	4.5

Table A.2. Summary of average UE and TE including standard deviation

Processing Parameters	Chem	UE (%)	UE SD (%)	TE (%)	TE SD (%)
890-610	**A**	12	0.5	21	0.7
	B	9	2.1	14	0.8
	C	11	0.5	18	1.2
	D	10	0.3	21	1.0
950-610	**A**	10	1.2	18	1.6
	B	10	0.7	18	1.6
	C	10	0.2	19	0.5
	D	8	0.9	16	1.7
890-490	**A**	9	1.6	18	3.2
	B	8	1.4	17	2.2
	C	9	1.3	16	1.4
	D	7	0.4	15	0.4
950-490	**A**	9	1.4	18	2.4
	B	7	1.8	13	5.0
	C	9	0.6	18	1.0
	D	7	0.7	15	1.6
890-630-490	**A**	7	1.0	16	1.7
	B	9	0.6	18	1.7
	C	9	0.5	16	1.9
	D	7	0.2	15	0.3
950-630-490	**A**	5	1.2	13	1.7
	B	7	1.9	15	2.2
	C	4	0.8	11	1.1
	D	6	0.6	14	1.5

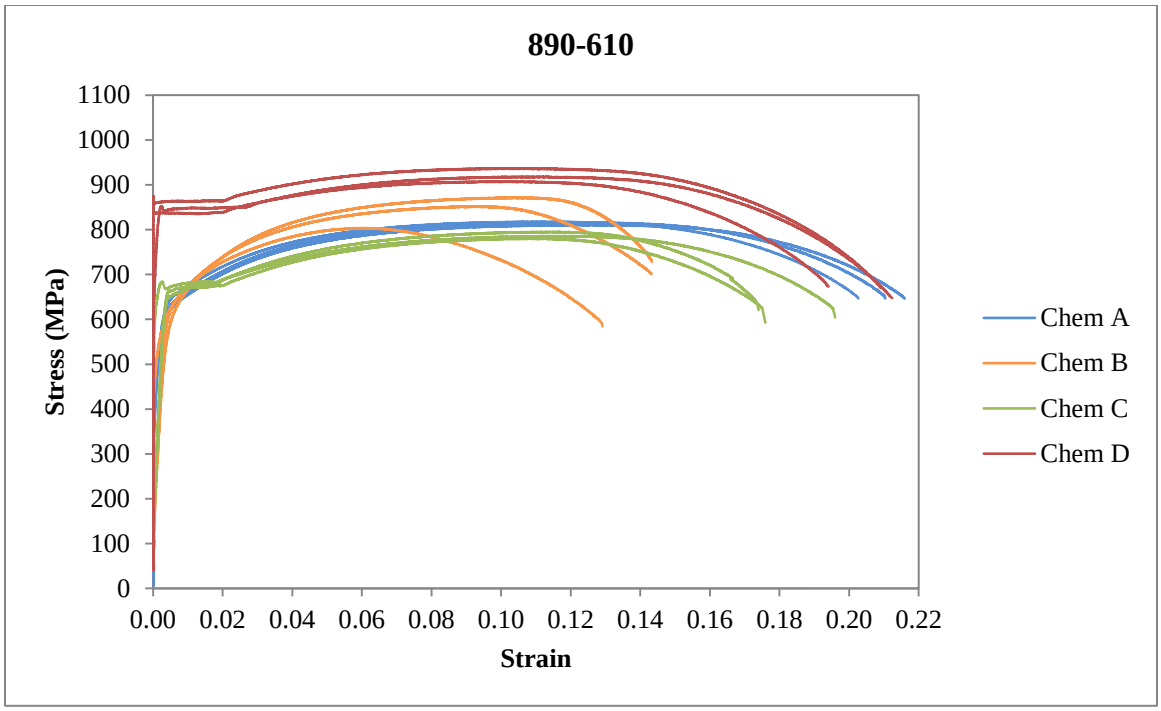

Figure A.1. Stress-strain curves from all chemistries processed at 890-610

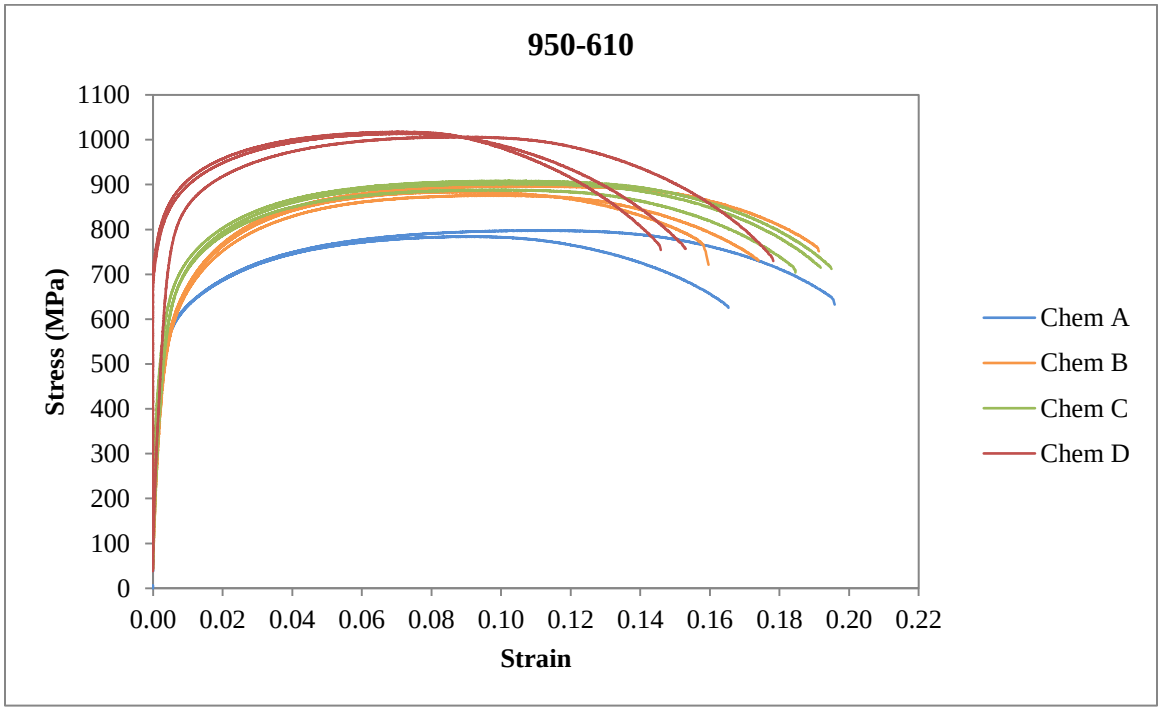

Figure A.2. Stress-strain curves from all chemistries processed at 950-610

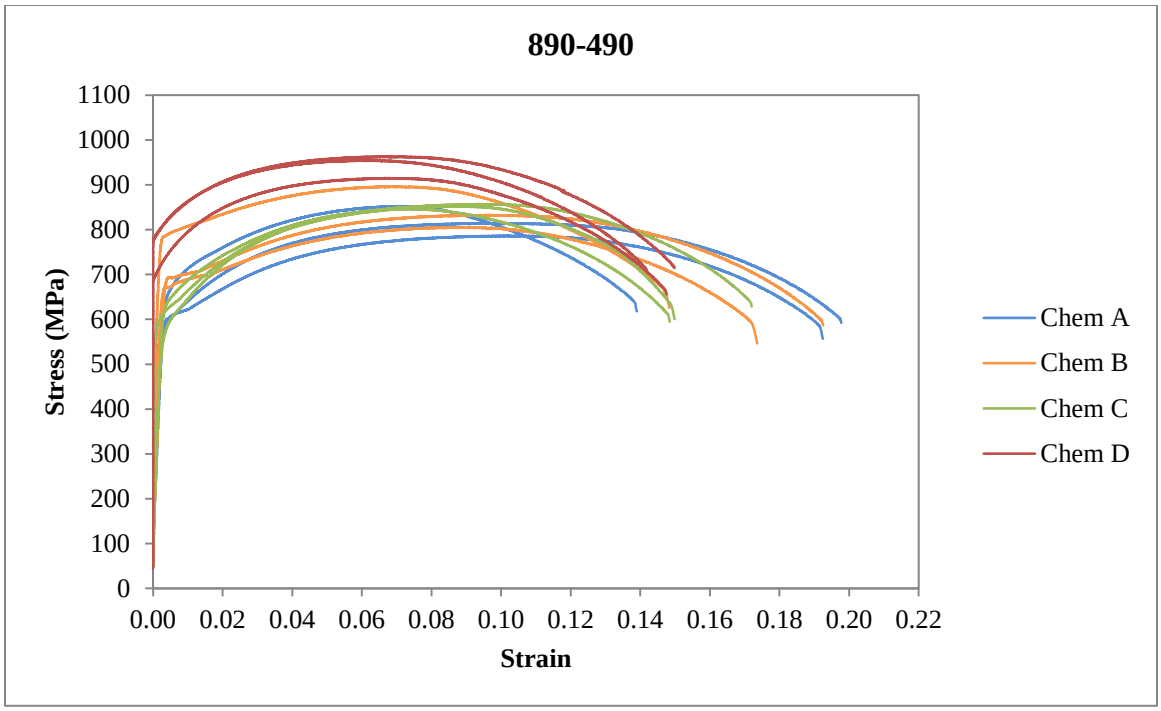

Figure A.3. Stress-strain curves from all chemistries processed at 890-490

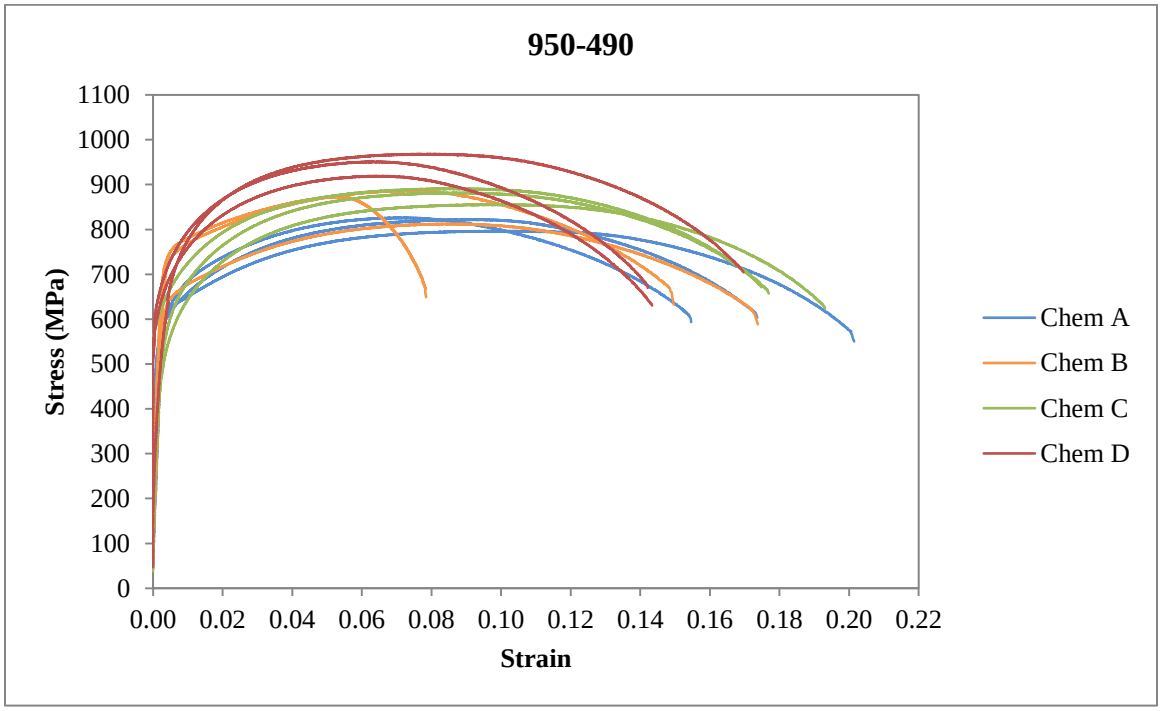

Figure A.4. Stress-strain curves from all chemistries processed at 950-490

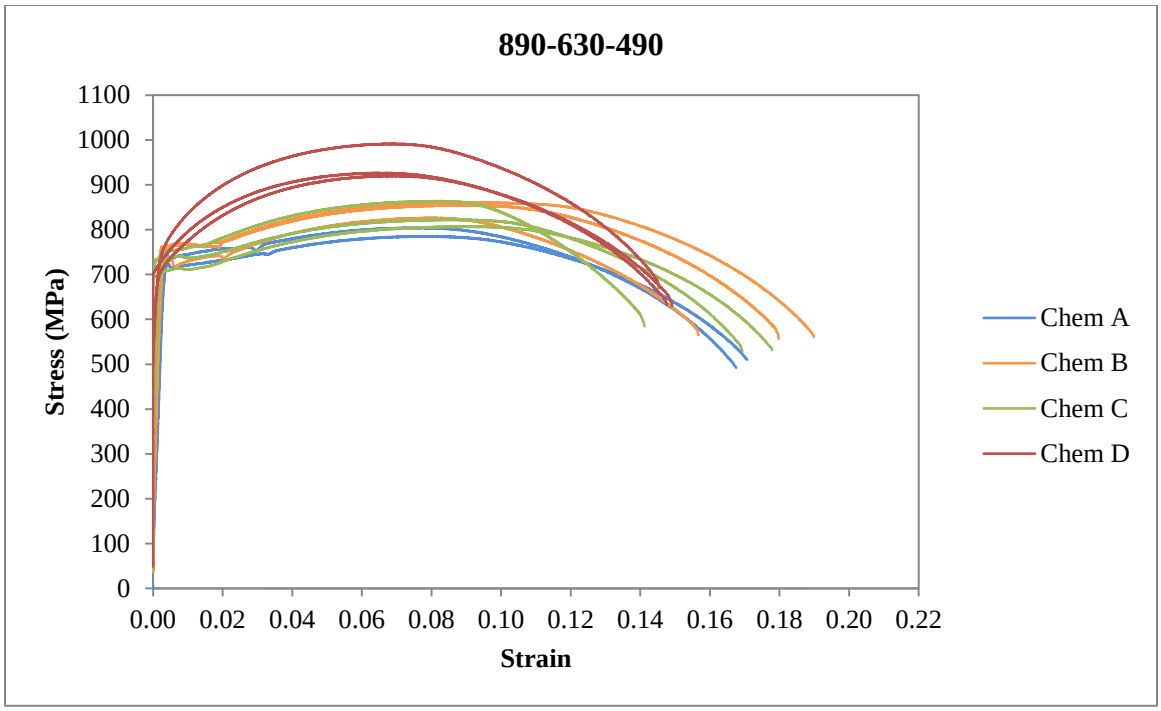

Figure A.5. Stress-strain curves from all chemistries processed at 890-630-490

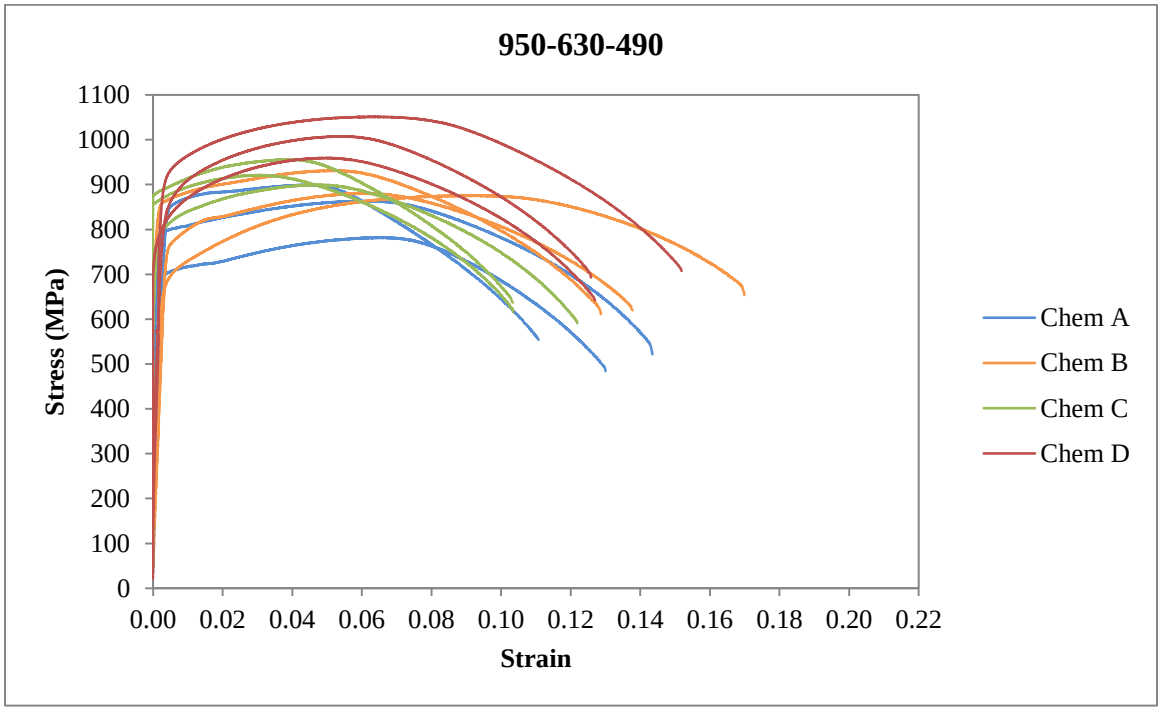

Figure A.6. Stress-strain curves from all chemistries processed at 950-630-490

Appendix B TEM and APT Images

The following figures display additional images from TEM thin foil analysis and from APT analysis that are not included in the results in Chapter 4.

Chemistry C

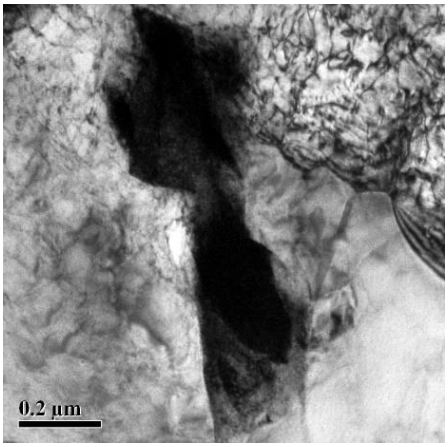

Chemistry D

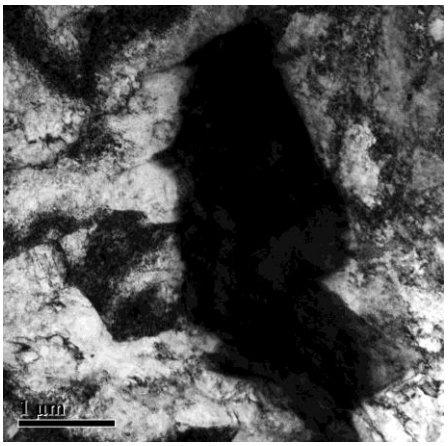

a. Granular martensite or M/A regions

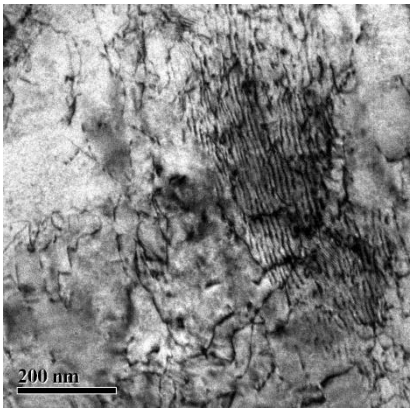

b. Dislocation sub-structure within ferrite

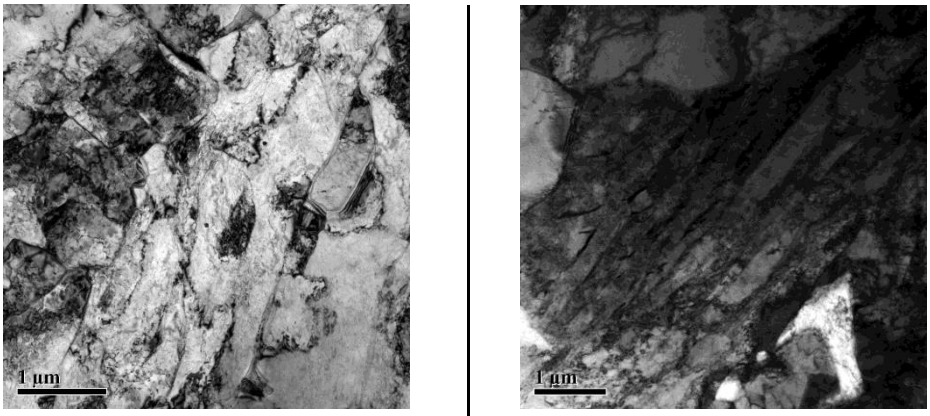

c. Regions of lath ferrite or bainite

Figure B.1. Thin foil TEM images of chemistries C and D processed at 950-610

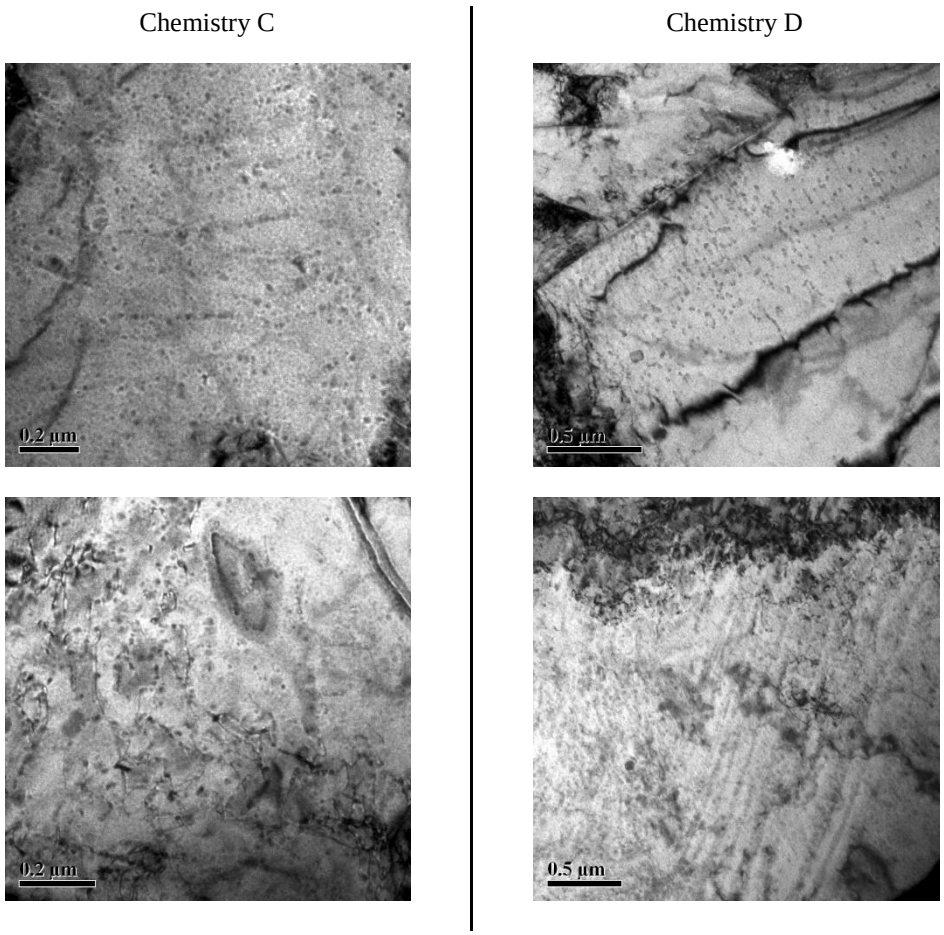

Figure B.2. Examples of fine precipitates present in chemistries C and D processed at 950-610.

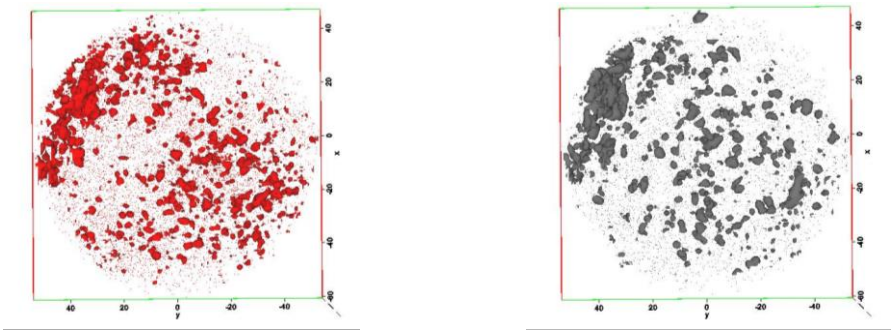

a. C density with 1.5 at% C isosurfaces b. Nb density with 0.5 at% Nb isosurfaces

Figure B.3. Endview of dataset 2 from chemistry C processed at 950-610 showing segregation of C and Nb

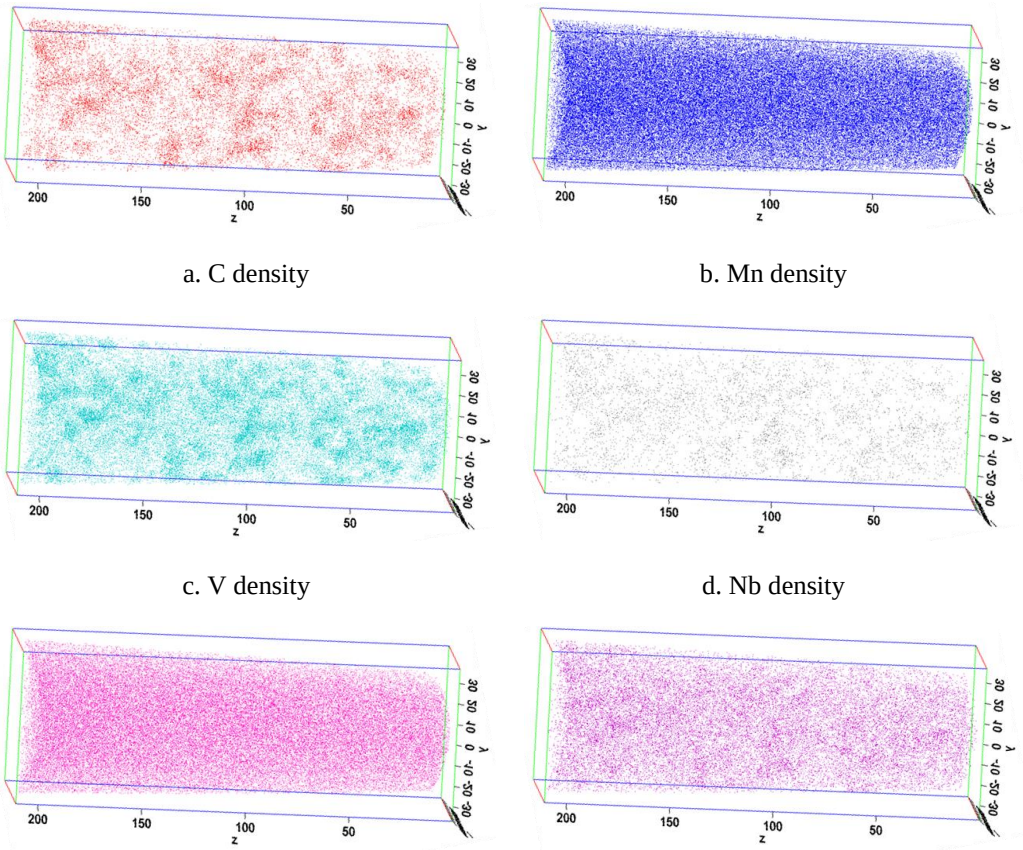

a. C density b. Mn density

c. V density d. Nb density

e. Cr density f. Mo density

Figure B.4. Dot maps showing density of C, Mn, V, Nb, Cr and Mo in dataset 1 from chemistry D processed at 950-610. Segregation is evident in C, V, Nb and Mo

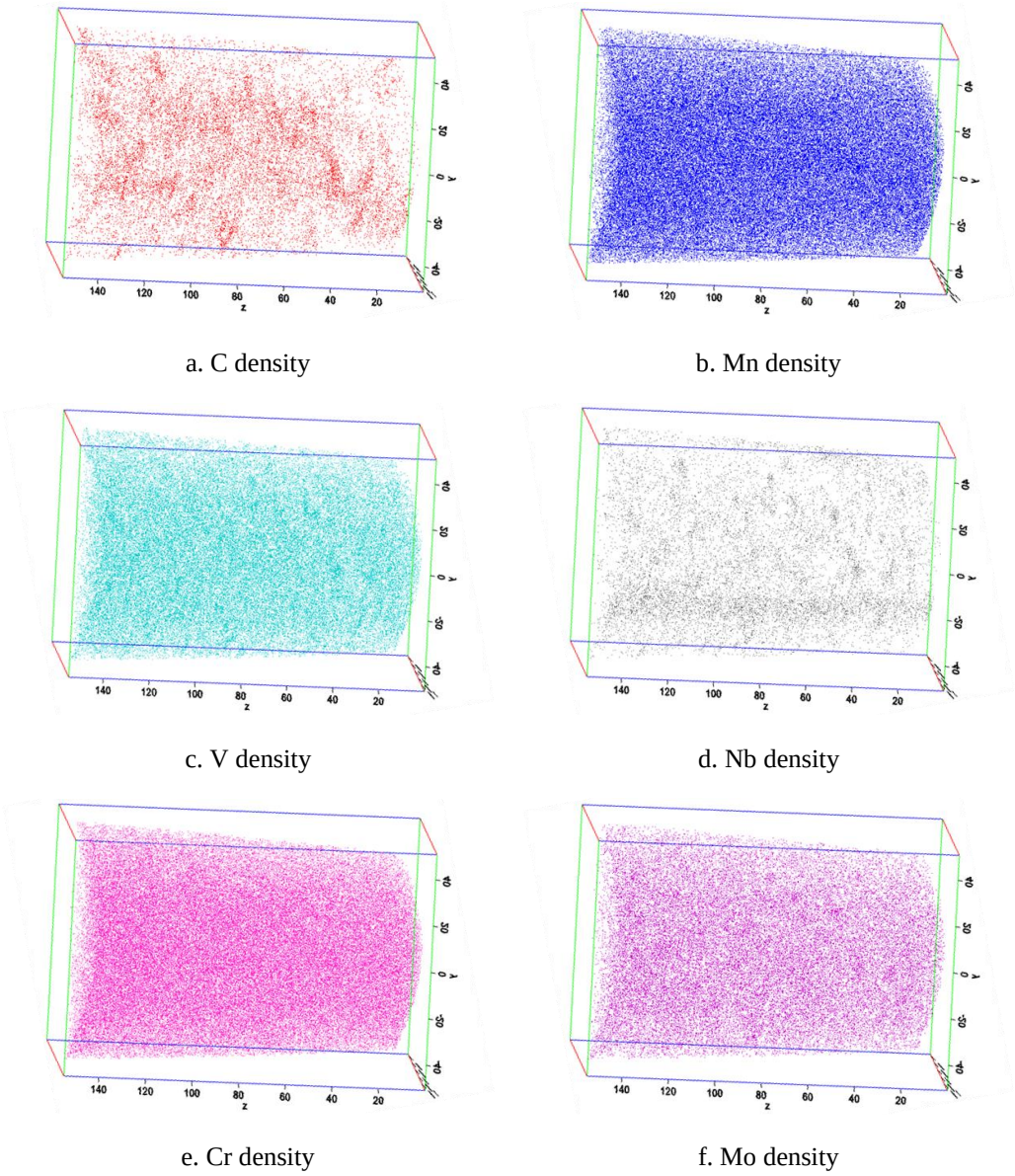

Figure B.5. Dot maps showing density of C, Mn, V, Nb, Cr and Mo in dataset 2 from chemistry D processed at 950-610. Segregation is evident in C, V, Nb and Mo

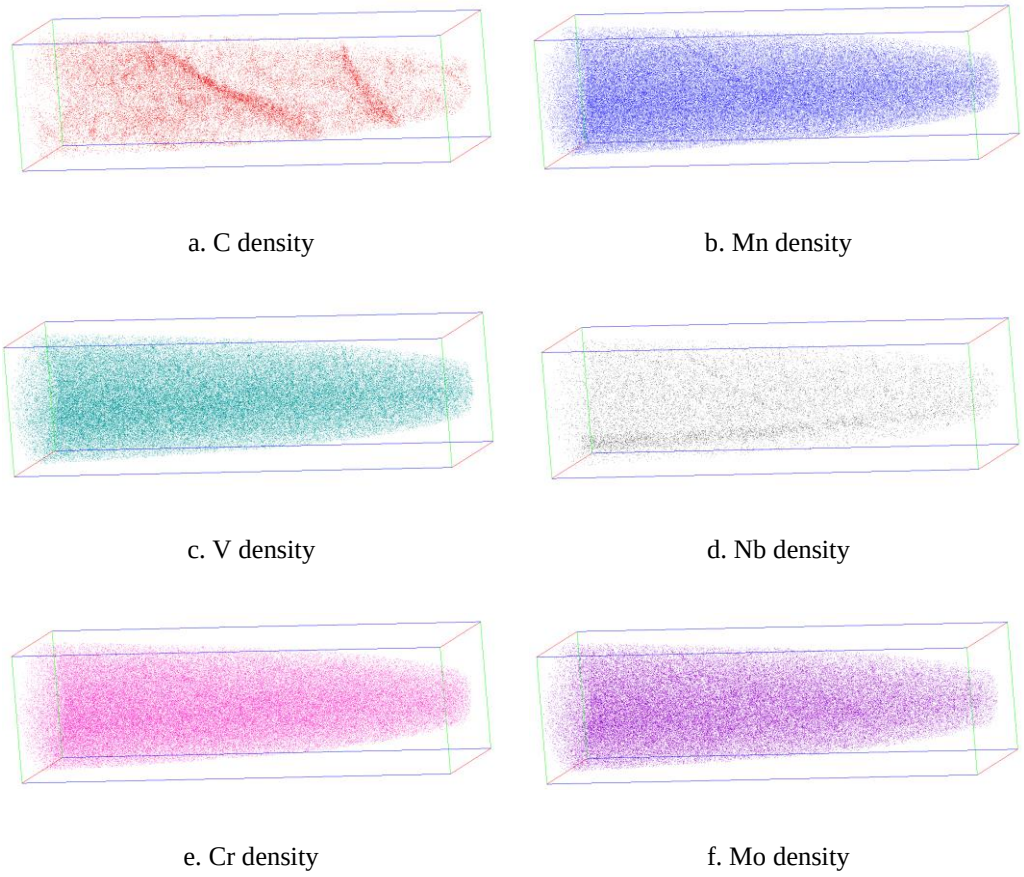

a. C density b. Mn density

c. V density d. Nb density

e. Cr density f. Mo density

Figure B.6. Dot maps showing density of C, Mn, V, Nb, Cr and Mo in dataset 2 from chemistry D processed at 950-630-490. Segregation is evident in C, V, Nb and Mo